Journal of Physics: Condensed Matter

TOPICAL REVIEW • OPEN ACCESS

Three-electron spin qubits

To cite this article: Maximilian Russ and Guido Burkard 2017 *J. Phys.: Condens. Matter* **29** 393001

View the article online for updates and enhancements.

Related content

- Physics of lateral triple quantum-dot molecules with controlled electron numbers
  Chang-Yu Hsieh, Yun-Pil Shim, Marek Korkusinski et al.
- Tutorial
  Veronica Cerletti, W A Coish, Oliver Gywat et al.
- Time-dependent single-electron transport
  Toshimasa Fujisawa, Toshiaki Hayashi and Satoshi Sasaki

This content was downloaded from IP address 134.34.147.213 on 13/09/2017 at 11:19

OPEN ACCESS
IOP Publishing
Journal of Physics: Condensed Matter
J. Phys.: Condens. Matter **29** (2017) 393001 (35pp)
https://doi.org/10.1088/1361-648X/aa761f

Topical Review

Three-electron spin qubits

Maximilian Russ and Guido Burkard

Department of Physics, University of Konstanz, D-78457 Konstanz, Germany

E-mail: Guido.Burkard@uni-konstanz.de

Received 25 April 2016, revised 15 May 2017
Accepted for publication 31 May 2017
Published 24 August 2017

Abstract

The goal of this article is to review the progress of three-electron spin qubits from their inception to the state of the art. We direct the main focus towards the exchange-only qubit (Bacon *et al* 2000 *Phys. Rev. Lett.* **85** 1758–61, DiVincenzo *et al* 2000 *Nature* **408** 339) and its derived versions, e.g. the resonant exchange (RX) qubit, but we also discuss other qubit implementations using three electron spins. For each three-spin qubit we describe the qubit model, the envisioned physical realization, the implementations of single-qubit operations, as well as the read-out and initialization schemes. Two-qubit gates and decoherence properties are discussed for the RX qubit and the exchange-only qubit, thereby completing the list of requirements for quantum computation for a viable candidate qubit implementation. We start by describing the full system of three electrons in a triple quantum dot, then discuss the charge-stability diagram, restricting ourselves to the relevant subsystem, introduce the qubit states, and discuss important transitions to other charge states (Russ *et al* 2016 *Phys. Rev.* B **94** 165411). Introducing the various qubit implementations, we begin with the exchange-only qubit (DiVincenzo *et al* 2000 *Nature* **408** 339, Laird *et al* 2010 *Phys. Rev.* B **82** 075403), followed by the RX qubit (Medford *et al* 2013 *Phys. Rev. Lett.* **111** 050501, Taylor *et al* 2013 *Phys. Rev. Lett.* **111** 050502), the spin-charge qubit (Kyriakidis and Burkard 2007 *Phys. Rev.* B **75** 115324), and the hybrid qubit (Shi *et al* 2012 *Phys. Rev. Lett.* **108** 140503, Koh *et al* 2012 *Phys. Rev. Lett.* **109** 250503, Cao *et al* 2016 *Phys. Rev. Lett.* **116** 086801, Thorgrimsson *et al* 2016 arXiv:1611.04945). The main focus will be on the exchange-only qubit and its modification, the RX qubit, whose single-qubit operations are realized by driving the qubit at its resonant frequency in the microwave range similar to electron spin resonance. Two different types of two-qubit operations are presented for the exchange-only qubits which can be divided into short-ranged and long-ranged interactions. Both of these interaction types are expected to be necessary in a large-scale quantum computer. The short-ranged interactions use the exchange coupling by placing qubits next to each other and applying exchange-pulses (DiVincenzo *et al* 2000 *Nature* **408** 339, Fong and Wandzura 2011 *Quantum Inf. Comput.* **11** 1003, Setiawan *et al* 2014 *Phys. Rev.* B **89** 085314, Zeuch *et al* 2014 *Phys. Rev.* B **90** 045306, Doherty and Wardrop 2013 *Phys. Rev. Lett.* **111** 050503, Shim and Tahan 2016 *Phys. Rev.* B **93** 121410), while the long-ranged interactions use the photons of a superconducting microwave cavity as a mediator in order to couple two qubits over long distances (Russ and Burkard 2015 *Phys. Rev.* B **92** 205412, Srinivasa *et al* 2016 *Phys. Rev.* B **94** 205421). The nature of the three-electron qubit states each having the same total spin and total spin in z-direction (same Zeeman energy) provides a natural protection against several sources of

Original content from this work may be used under the terms of the Creative Commons Attribution 3.0 licence. Any further distribution of this work must maintain attribution to the author(s) and the title of the work, journal citation and DOI.

noise (DiVincenzo *et al* 2000 *Nature* **408** 339, Taylor *et al* 2013 *Phys. Rev. Lett.* **111** 050502, Kempe *et al* 2001 *Phys. Rev.* A **63** 042307, Russ and Burkard 2015 *Phys. Rev.* B **91** 235411). The price to pay for this advantage is an increase in gate complexity. We also take into account the decoherence of the qubit through the influence of magnetic noise (Ladd 2012 *Phys. Rev.* B **86** 125408, Mehl and DiVincenzo 2013 *Phys. Rev.* B **87** 195309, Hung *et al* 2014 *Phys. Rev.* B **90** 045308), in particular dephasing due to the presence of nuclear spins, as well as dephasing due to charge noise (Medford *et al* 2013 *Phys. Rev. Lett.* **111** 050501, Taylor *et al* 2013 *Phys. Rev. Lett.* **111** 050502, Shim and Tahan 2016 *Phys. Rev.* B **93** 121410, Russ and Burkard 2015 *Phys. Rev.* B **91** 235411, Fei *et al* 2015 *Phys. Rev.* B **91** 205434), fluctuations of the energy levels on each dot due to noisy gate voltages or the environment. Several techniques are discussed which partly decouple the qubit from magnetic noise (Setiawan *et al* 2014 *Phys. Rev.* B **89** 085314, West and Fong 2012 *New J. Phys.* **14** 083002, Rohling and Burkard 2016 *Phys. Rev.* B **93** 205434) while for charge noise it is shown that it is favorable to operate the qubit on the so-called '(double) sweet spots' (Taylor *et al* 2013 *Phys. Rev. Lett.* **111** 050502, Shim and Tahan 2016 *Phys. Rev.* B **93** 121410, Russ and Burkard 2015 *Phys. Rev.* B **91** 235411, Fei *et al* 2015 *Phys. Rev.* B **91** 205434, Malinowski *et al* 2017 arXiv: 1704.01298), which are least susceptible to noise, thus providing a longer lifetime of the qubit.

Keywords: qubits, spin qubits, exchange-only qubits, resonant exchange qubits, RX qubit, charge noise, cavity QED

(Some figures may appear in colour only in the online journal)

1. Introduction

1.1. Quantum computation

Since the early beginnings, certain aspects of quantum mechanics such as entanglement and non-locality have fascinated those who studied it due to their counterintuitive behavior in comparison with everyday life, thus fueling heated debates. With the rise of the information processing technology the question arose whether these quantum properties could be exploited and used for information processing, thus opening the research field of quantum information processing (see e.g. [28] for a historical account). Quantum computers follow a logic based on quantum mechanics and can be seen as superior to classical computers since they have the ability to solve certain problems which classical computers cannot solve in any reasonable time. It does not seem that quantum computers surpass classical computers in performing arbitrary tasks but since they operate according to quantum mechanical laws, they appear to be superior in simulating other quantum systems [29, 30], a problem that classical computers are unable to tackle efficiently. Furthermore, quantum computers can solve some very specialized problems. The most well-known application is the Shor algorithm which is able to efficiently factorize integers [31] and thereby subvert the ability to encode encrypted information using prime factors as a private key [32]. Other known applications are the Deutsch algorithm, its generalization, the Deutsch–Josza algorithm [28], and the Grover algorithm for efficient search in unsorted databases [33, 34].

Following directly after the discovery of some of its potential applications, concepts for a physical realization of such a quantum computer were proposed. These concepts are based on the charge of electrons [35, 36], the spin of electrons in quantum dots [37], nuclear spin [38], photons in resonators and cavities [39], trapped ions [40], low-capacitance Josephson junctions [41, 42], donor atoms [43], colored centers in diamond [44, 45] or silicon-carbide [46], or linear optics [47].

The five DiVincenzo criteria for a fully functioning quantum computer [36, 48, 49] help to decide which concepts are reliable and, in a few words, comprise the scalability of the system, initialization and read-out schemes, the durability of the stored information, and concepts for precise control of the quantum bits (qubits) [36]. These qubits are the fundamental building block of each quantum computer and are not limited to two states, 0 and 1, but can be in any superposition of these, $|\Psi\rangle = \alpha|0\rangle + \beta|1\rangle$ with $|\alpha|^2 + |\beta|^2 = 1$ [28], thus forming a quantum two-level system. Each qubit can be visualized on the Bloch sphere (see figure 1) where the basis states of the qubit, $|0\rangle$ and $|1\rangle$, are located on the poles while vectors pointing to the surface of the sphere represent all possible pure states of the qubit. Thus, complete control of a qubit requires interactions corresponding to two independent axes of rotations on the Bloch sphere [28]. The physical realization of these rotations depends on the chosen qubit system.

The aim of this topical review is to review the recent progress and advances of three-spin qubit systems which are considered as a possible and promising candidate for a functioning quantum computer. The organization of the paper is as follows. In section 1, we provide an introduction in which we briefly cover the fundamental concepts needed for three-spin qubits such as their experimental realization (section 1.2), followed by a discussion of the exchange interaction (section 1.3), the single-spin qubit (section 1.4), and the two-spin singlet-triplet qubit (section 1.5). Subsequently in section 2, the three-spin qubits are introduced. We start by explaining the electrical (section 2.1) and spin properties of three-spin qubits (section 2.2) constructing a framework for their further investigation. Afterwards, we introduce and discuss the different

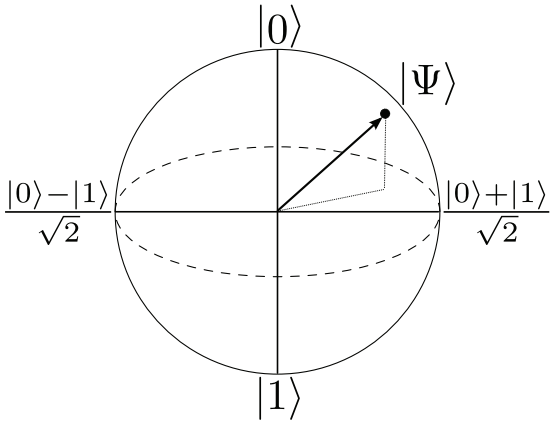

Figure 1. Visualization of a qubit on the Bloch sphere. The basis states $|0\rangle$ and $|1\rangle$ are located on the poles and arbitrary pure qubit states $|\Psi\rangle$ are represented by vectors pointing to an arbitrary point on the surface of the sphere.

physical implementations of three-spin qubits in the light of the DiVincenzo criteria, the exchange-only qubit (section 2.3) with its derived versions, the resonant-exchange qubit (section 2.3.4) and the always-on exchange-only qubit (section 2.3.3), the spin-charge qubit (section 2.4), and the hybrid qubit (section 2.5). In section 3, two-qubit gates are discussed for the three-spin qubits with the focus on exchange-based short-ranged (section 3.1) and cavity-mediated long-ranged operations (section 3.2). Finally, in section 4, we investigate the behavior of three-spin qubits under the influence of the two main sources of decoherence, magnetic noise (section 4.1) and charge noise (section 4.2), and provide concepts for a reduction of the decoherence effects. We conclude in section 5 with a summary and future perspectives.

1.2. Spin qubits: physical realization and measurement techniques

Although three-spin qubits were already proposed in 2000 [2] it took several years for the appearance of devices capable of operating three-spin qubits due to the multitude technical and engineering challenges. The main challenges for a functioning three-spin (here three electrons in a triple quantum dot (TQD)) device is the complexity of the system since several gate electrodes are needed in order to address each electron individually. The first device was realized around 2006 [50] and was soon followed by other realizations [4, 51–61, 62] which improved the positioning of the electrons. A functioning three-spin qubit device capable of quantum computation was demonstrated in a double quantum dot (DQD) [11, 63–65] and in a linear TQD [4, 5, 54, 59, 60, 66–70]. While a triangular shape provides some interesting new features, e.g. chirality [71–77] and faster qubit operations [2, 13], the advantages currently do not seem to outweigh the experimental drawbacks and difficulties. Therefore, and since almost all experiments and most theoretical studies use the linear geometry we also mostly stick to the linear geometry in this review and implicitly assume that each TQD is linearly arranged, unless otherwise stated.

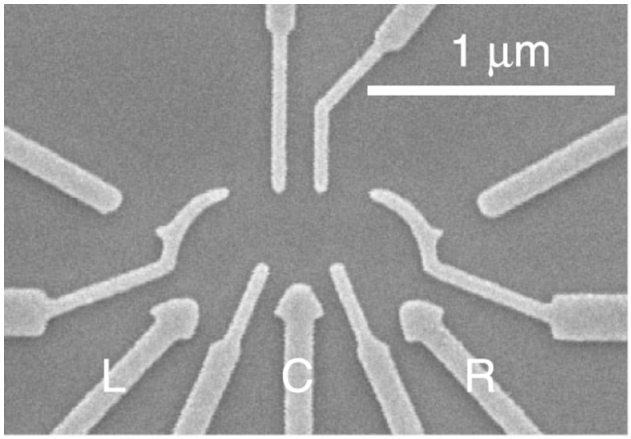

Figure 2. Scanning electron micrograph of a depletion mode triple quantum dot (TQD) device in GaAs. Metallic gates (light gray) are deposited on top of the heterostructure (dark gray) to deplete the 2DEG underneath in order to form isolated structures. The number of electrons and the energy in each QD is controlled by the gates labeled as L, C, and R. Tunneling between the electrons is controlled by the thinner gates in between. Reprinted with permission from [68] Copyright 2014 by the American Physical Society.

The most common technique implementing semiconductor quantum dots (QDs) are lateral QDs where a two-dimensional electron gas (2DEG) is further confined by electrostatic potentials provided by the gate electrodes forming an (approximately) zero-dimensional structure (see figure 2). While GaAs [78] and silicon (Si) [79] are the typical choice of material, more exotic semiconductors [80–87] are also possible although rare. Crucial for the implementation is the 2DEG experimentally realized by using a heterostructure which accumulates the electrons at an interface; the GaAs layer is sandwiched between AlGaAs layers [78] and Si by either SiGe [79] layers or SiO_x [88, 89] layers. Advances in fabrication process allow for atomically precise layer interfaces and gate structures with a very high precision giving rise to scalable and controllable quantum dot devices (selected examples see [69, 90–98]) with the current record of nine individually addressable QDs [99]. Regarding the choice for material there is a clear tendency towards favoring Si since Si consists of ≈95% nuclear free isotopes which can be increased with isotopic purification [100]. For further confinement of the electrons, metallic gates are placed on top and/or underneath the heterostructure which locally deplete the 2DEG forming an isolated island. In undoped Si/SiGe the 2DEG is typically empty with no gate voltage applied and the gates accumulate electrons into the 2DEG [79]. Calibration of the voltages on these gate allows one to reach the few electron regime where only a few electrons are still occupying the dots [78, 79]. Additional gates (number depends on the material and fabrication, e.g. four in the device seen in figure 2) are required to form the dots as well as to control the coupling to the lead which allows for a filling of the dots. A typical setup for a TQD consists of at least five gates (see figure 2), three gates (L-, C-, R-gate in figure 2) on top of each QD in order to control the energy at each dot and two gates in between for control of the tunneling couplings. Due to the

higher complexity of the multiple-dot nano-devices recent devices use a stacking gate architecture crucial for large-scale devices [89, 94, 95, 99, 101].

Common techniques for measurement of the QD devices require additional QDs or quantum point contacts (QPC) [102, 103], single electron transistors [104–106], or tunnel junctions [107] in order to sense the number and movement of the electrons in each dot in a time resolved measurement [78, 79]. Due to the finite range of the charge sensors, large arrays of QDs have multiple sensors, e.g. a recently studied nine-dot device has three charge sensors [99]. Another measurement technique involves photons that carry the information out of the device. Connecting the device to a microwave cavity allows for read-out of device parameters using cavity quantum electrodynamics (cQED) without directly interfering with the device [108–117]. Both measurement techniques also allow for read-out of the qubit states; cavity read-out requires for a few implementations strong coupling between the qubit and the cavity. The measurement techniques can be grouped as either invasive, e.g. emptying the QD [78, 79], or noninvasive, sensing the charge or spin of the electrons in the QD without changing the electron number [78, 79].

1.3. The exchange interaction

The most important tool for spin quantum computation with electrons in QDs is the exchange interaction, originating from the sign change under exchange of fermionic particles, since it can be electrically controlled both very precisely and fast by detuning of the externally applied electrostatic gate voltages [78, 118].

A sufficient explanation for exchange interaction between N_e electrons in N QDs is provided by the Hubbard model [119, 120] with symmetric spin-conserving nearest neighbor hopping

$$H_{\rm Hub} = \sum_{i=1}^{N}\left[\frac{\tilde{U}}{2}n_i(n_i-1)+V_i n_i\right] + \sum_{\langle i,j\rangle} U_C n_i n_j + \sum_{\sigma=\uparrow,\downarrow}(t_{ij}c^{\dagger}_{i,\sigma}c_{j,\sigma}+\text{h.c.}), \quad (1)$$

where the operator $c^{\dagger}_{i,\sigma}$ ($c_{i,\sigma}$) creates (annihilates) an electron in QD i with spin $\sigma=\uparrow,\downarrow$, V_i is the gate energy in QD i, $\tilde{U}$ is the energy penalty for doubly occupying a single QD due to the Coulomb repulsion, and U_C is the energy to pay for two electrons in neighboring QDs. We define the number operator $n_i \equiv \sum_\sigma c^{\dagger}_{i,\sigma}c_{i,\sigma}$ and the gate-controlled hopping matrix elements $t_{ij}=t_{ji}=t$. For a number of electrons N_e matching the number N of QDs, $N=N_e$, the low-energy Hamiltonian for suitably adjusted gate potentials V_i can be approximated by a Schrieffer–Wolff transformation [121, 122] yielding an Heisenberg spin chain

$$H_{\rm Heis} = \sum_{\langle i,j\rangle} J_{ij}\boldsymbol{S}_i \cdot \boldsymbol{S}_j, \quad (2)$$

where $\boldsymbol{S}_i$ is the spin operator of the ith electron in QD i and the sum runs over neighboring pairs of electrons. While the general case is quite interesting, in this review we are only interested in small systems with $N \leqslant 3$.

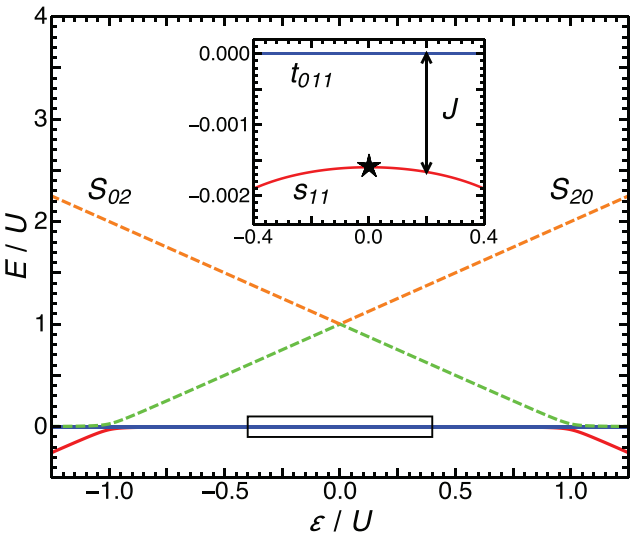

Figure 3. Eigenenergies (in units of the charging energy U) of the singlet-triplet (ST) qubit as a function of detuning ε for weak tunneling, $t = 0.02\,U$. The inset magnifies the energy splitting between the $|s\rangle$ and $|t_0\rangle$ state due to the exchange interaction J. Inside the (1, 1) charge configuration regime $J \approx 4t^2U/(U^2-\varepsilon^2)$ [120]. The eigenenergies are labeled with their dominating charge configuration. There is a sweet spot (black star in inset) at zero detuning, $\varepsilon = 0$.

We explicitly demonstrate the simplest case for exchange, two electrons in $N=2$ QDs. Considering a single (valley-) orbital for each QD and restricting ourselves to the $S_z=0$ subspace there are four relevant states

$$|s\rangle \equiv \frac{1}{\sqrt{2}}(c^{\dagger}_{1,\uparrow}c^{\dagger}_{2,\downarrow} - c^{\dagger}_{1,\downarrow}c^{\dagger}_{2,\uparrow})|\text{vac}\rangle, \quad (3)$$

$$|t_0\rangle \equiv \frac{1}{\sqrt{2}}(c^{\dagger}_{1,\uparrow}c^{\dagger}_{2,\downarrow} + c^{\dagger}_{1,\downarrow}c^{\dagger}_{2,\uparrow})|\text{vac}\rangle, \quad (4)$$

$$|s\rangle_{11} \equiv c^{\dagger}_{1,\uparrow}c^{\dagger}_{1,\downarrow}|\text{vac}\rangle, \quad (5)$$

$$|s\rangle_{22} \equiv c^{\dagger}_{2,\uparrow}c^{\dagger}_{2,\downarrow}|\text{vac}\rangle. \quad (6)$$

States with $S_z=\pm 1$ and $|t_0\rangle$ are pure triplet states, thus, not coupled to any intermediate states with (2, 0) or (0, 2) charge configurations and, therefore, not affected by the exchange interaction. Introducing the dipolar detuning parameter $\varepsilon \equiv (V_1-V_2)/2$, the charging energy $U=\tilde{U}-U_C$ and assuming real valued tunneling parameters, the matrix representation of equation (1) in the basis given above is given by

$$H_{\rm ST} = \begin{pmatrix} 0 & 0 & \sqrt{2}t & \sqrt{2}t \\ 0 & 0 & 0 & 0 \\ \sqrt{2}t & 0 & U+\varepsilon & \\ \sqrt{2}t & 0 & 0 & U-\varepsilon \end{pmatrix}. \quad (7)$$

In figure 3 the eigenenergies of this Hamiltonian are plotted as a function of the detuning ε. Inside the (1, 1)-charge configuration regime the singlet qubit state $|s\rangle$ is hybridized, $|s\rangle \to |\tilde{s}\rangle$, by the admixture of the other charge states, $|s\rangle_{11}$ and $|s\rangle_{22}$, thereby, splitting the qubit by the exchange interaction

$J \approx 4t^2U/(U^2 - \varepsilon^2)$ [120] which can be used either for entangling two-qubit gates or single qubit rotations depending on the implementation of the logical qubit.

1.4. Spin-$\frac{1}{2}$ qubit

The original idea for a semiconductor electron spin qubit was proposed by Loss and DiVincenzo [123] two decades ago. As the simplest choice, the spin-$\frac{1}{2}$ qubit is encoded in the two-level system associated with the spin-degree of freedom, i.e. the $|0\rangle \equiv |\uparrow\rangle$ and $|1\rangle \equiv |\downarrow\rangle$ states, of a single electron confined in the lowest orbital of a single QD. Since the qubit states have opposite spin projections the qubit is susceptible to magnetic fields. An external magnetic field $\boldsymbol{B}(\tau)$ (can depend on time τ) lifts the degeneracy between the qubit states by the Zeeman energy $E = g\mu_B \boldsymbol{B}(\tau) \cdot \boldsymbol{S}$ [37, 78] and fixes the quantization axis.

Considering $\boldsymbol{B}(\tau) = (B_x(\tau), 0, B_z)^T$ with a large time-independent magnetic field in z-direction, $B_z = B$, and a small oscillatory driving field in x-direction, $B_x(\tau) = B_D \cos(\omega\tau)$. In qubit space the Zeeman term takes the expression for electron spin resonance (ESR)

$$H_{\mathrm{ESR}} = \frac{\hbar}{2}\omega_z\sigma_z + \frac{\hbar}{2}\omega_x \cos(\omega\tau)\sigma_x \tag{8}$$

with the Zeeman energies $\hbar\omega_z = g\mu_B B$ and $\hbar\omega_x = g\mu_B B_D$. Turning on the oscillating field causes Rabi transitions between the spin states which together with the energy splitting of the qubit states provide full control of the qubit [37]. As an alternative for oscillating magnetic fields one can also modulate the g-factor of the material which yields the same expression. The speed of the gates depends on the strength of the oscillatory driving field resulting in typical gate times $\tau_g \approx 100$ ns [124].

Electric dipole spin resonance (EDSR) can be seen as an improvement of ESR which allows for electric driving of the qubit instead of magnetic driving. In the presence of spin–orbit interaction an electric field $E(\tau) = E_0 \cos(\omega\tau)$ induces, in general, non-zero components of a pseudo magnetic field $b(\tau)$ perpendicular to the static magnetic field [37, 125]. This perpendicular (pseudo) magnetic field yields the same dynamics in the system as a real magnetic field due to $b(\tau) \propto E(\tau)$ with a coupling strength $\omega_{\tilde{x}}$ depending on the spin–orbit parameters [125]. Experiments demonstrate successful qubit rotations including spin flips achieving gate times on the order of $\tau_g \approx 100$ ns in GaAs devices [126]. However, the proposed $\tau_g \approx 10$ ns [125] are not reached yet due to problems occurring at high electric fields, e.g. incomplete spin flips, [127]. Since the Rabi oscillations depend on the strength of the spin–orbit interaction, materials with strong spin–orbit coupling, such as InAs nanowires, can increase spin-flip frequency correspondingly [128]. Rabi oscillation as fast as $f_{\mathrm{Rabi}} \approx 58$ MHz were demonstrated [129]. However, the qubit fidelity of these fast gates is quite poor (≈50%) due to strong dephasing from nuclear spins [129].

Alternatively, one can use an oscillating electric field combined with a gradient in the magnetic field (slanting magnetic field) which does not rely on spin–orbit interaction [130, 131] allowing for the use of materials with weak spin–orbit coupling such as silicon. The electric field $E(\tau)$ induces an oscillation of the electron position such that the electron experiences an oscillating magnetic field of the same frequency $B(\tau) \propto E(\tau)$. Experiments in a GaAs device using the Overhauser fields demonstrate a spin-flip time comparable to standard ESR ($\tau_g \approx 110$ ns) [132] while the use of an integrated magnet yield a spin-flip time as fast as $\tau_g \approx 20$ ns [133] due to larger field gradients. High fidelity spin-flips are demonstrated in silicon devices ($f_{\mathrm{Rabi}} \approx 5$ MHz) due to the lower percentage of nuclear-spins and also show sufficient distinction to other valley states [101]. Individual control in multi-spin systems is successfully demonstrated in GaAs devices ($f_{\mathrm{Rabi}} \approx 9$ MHz [131], $f_{\mathrm{Rabi}} \approx 3$ MHz [134]).

Initialization and read-out schemes, among others, require a nearby auxiliary QD in order to enable a spin-to-charge conversion which is detectable by a QPC, or the coupling to the lead [78, 135].

The common implementation of two-qubit gates for spin-$\frac{1}{2}$ qubits makes use of the exchange interaction [78, 118] between two electrons in neighboring QDs (see previous section 1.3) which induces the universal $\sqrt{\mathrm{SWAP}}$-gate as described in the original proposal [123]. Experiments demonstrate two-qubit gates with a gate time $\tau_g \approx 180$ ps [78, 118, 136] with gate fidelities exceeding 99%. A full demonstration of universal quantum control in two spin-$\frac{1}{2}$ qubits was demonstrated about a decade after the original proposal [134].

The main advantage of single spin-$\frac{1}{2}$ qubits is their immunity to electric charge noise from background fluctuations; however, two or more coupled spin-$\frac{1}{2}$ qubits are not always immune. The exchange interaction needed for two-qubit gates is sensitive to charge noise, thus limiting the gate fidelity [137]. Improvements use, among others, dynamical decoupling techniques or operate the qubits at a sweet spot [138–140], working points least susceptible to the noise. In this review we do not focus on decoherence in single-spin qubits which is already extensively covered in related reviews (see [141] and [37]).

The electric control of spin-$\frac{1}{2}$ qubits is challenging to implement due to its dependence on slanting magnetic fields, spin–orbit effects, or oscillating magnetic fields which are not very reliable due to the weak coupling to the spins. Another potential drawback of the spin-$\frac{1}{2}$ qubit is the rather strong susceptibility to (global) magnetic fields which are, on the one hand, required for fast single qubit operations, while on the other hand, allow coupling the qubit to magnetic noise giving rise to strong decoherence. The strongest source of decoherence is magnetic noise due to nuclear spins [37, 142–145] while relaxation processes are dominated by the spin–orbit interaction [37, 146–151]. Theoretical studies [142] and experimental demonstration [78, 118] show typical dephasing times on the order of $T_2^\star \approx 10$ ns in GaAs devices [118, 152]. However, due to the slow dynamic of the nuclear field, the coherence time of the qubit can be significantly increased by either strongly polarizing the nuclear spin [145] which has not

been successfully demonstrated yet, or using rephasing pulse sequences as spin-echo or CPMG [153]. Combining echo sequences additional notch filtering of the nuclear dynamics gives rise to even longer decoherence times $T_2 \approx 0.87$ ms [154]. Relaxation processes scale with an external magnetic field and are typically several orders of magnitudes slower [78, 155] with extreme cases $T_1 \approx 1$ s [155]. Both main sources for decoherence are reduced significantly in silicon devices due to the smaller number of nuclear spins and weaker spin–orbit interaction [79].

1.5. Singlet-triplet (ST) qubit

One idea to achieve (partial) electrical control of the qubit gates and to counteract the sensitivity of spin-$\frac{1}{2}$ qubits to fluctuations in global magnetic field (here labelled global magnetic noise) is to encode the quantum information in the $S_z = 0$ subspace of two electrons in a double quantum dot (DQD). One state is the $S_z = 0$ triplet state $|t_0\rangle \equiv (|\uparrow,\downarrow\rangle + |\downarrow,\uparrow\rangle)/\sqrt{2}$ and the other state is the singlet state $|s\rangle \equiv (|\uparrow,\downarrow\rangle - |\downarrow,\uparrow\rangle)/\sqrt{2}$. Since both states have the same $S_z = 0$ quantum number, global magnetic noise pointing along the quantization axis has no effect on these two states, thus, the singlet-triplet (S-T) qubit is protected against such noise and a simple example of a decoherence free subspace (DFS) qubit.

One axis of qubit control is provided by the electrically controllable exchange interaction between the electrons in the DQD due to the hybridization of the singlet energy given by admixture of charge states with doubly occupied dots and giving rise to a splitting of the singlet and triplet energy. This is the same mechanism that provides the two-qubit gates for the spin-$\frac{1}{2}$ qubit which can be controlled to a very high degree predicting gate fidelities exceeding 99% [140] with gate times below one nanosecond [118].

A second axis of control is provided by a gradient of the magnetic field in the DQD which lifts the degeneracy between the states $(|t_0\rangle + |s\rangle)/\sqrt{2} = |\uparrow,\downarrow\rangle$ and $(|t_0\rangle - |s\rangle)/\sqrt{2} = |\downarrow,\uparrow\rangle$ due to the difference in magnetic fields in the two QDs. This leads to rotations of the qubit around an axis orthogonal to the quantization axis [156]. Experimentally, these gradients are either given by the Overhauser fields of the nuclear spins in the host material, typical for GaAs, or the artificial magnetic field gradient obtained by placing a micromagnet in the vicinity of the DQD [131]. The latter implementation is needed for materials with a low density of nuclear spins such as silicon.

Read-out and state preparation can be achieved in the same way as for spin-$\frac{1}{2}$ qubits via 'spin-to-charge' conversion, where the gates are adiabatically detuned in such a way that one of the doubly occupied states is energetically highly favored [78]. Due to the Pauli exclusion principle only the anti-symmetric singlet state $|s\rangle$ is coupled via tunneling t to the doubly occupied state while the triplet state transition is forbidden giving rise to a read-out technique with fidelities exceeding 99%. The requirements for this read-out method to work are spin conserving hopping and a single non-degenerate ground state in the QD with a sufficient energy gap to the excited states.

Two-qubit gates can be implemented by the short-ranged exchange interaction together with spin–orbit interaction (exchange interaction alone is insufficient due to its high symmetry) [157], magnetic field gradients [158], by capacitively coupled DQDs [159–162] or an auxiliary dot [163]. Long-ranged two-qubit gates can either use the electrostatic coupling between the DQDs [159, 164, 165], and/or the coupling of two DQDs to the same microwave cavity [159, 166–171]. Since microwave cavity have been under intense investigation recently due to the access to high quality and high impedance microwave cavities [115, 172], the last approach seems in reach. The required strong coupling regime for such an interaction, where the transfer of information is faster than the cavity and the qubit decays, has recently been achieved for a single electron charge inside a DQD in carbon nanotubes [173], Si/SiGe [113] and GaAs [115] quantum dots.

The main concern of the ST qubit is the lack of electric control for one of the single-qubit rotation axes provided by the magnetic field gradients. Since this axes are either provided by Overhauser fields, which one cannot control, or by an additional micro magnet, where the magnetic fields are fixed by the geometry, this interaction is permanently turned on. The latter implementation can be controlled to a certain degree by changing the relative position of the quantum dots to the micro magnets through the gate voltages which changes the magnetic field gradients the qubit is exposed to [131].

Another downside for the ST qubit is the opening of a channel which couples the qubit to charge noise, electric fluctuations of the environment or the gate potentials. Electric fields can couple to the qubit through the detuning parameter ε and in this way give rise to an exponential decay of coherence due to dephasing. The exact decay depends on the spectral density of the noise $S_q(\tilde{\omega}) = A|\tilde{\omega}|^{-\gamma}$ where A is the strength of the noise, $\tilde{\omega}$ is the noise frequency, and γ is the spectral density exponent which usually has to be set phenomenologically or needs to be measured in experiments and strongly depends on the host material and device fabrication. This power law dependence arises from statistical calculations considering many fluctuators [139, 174], agreeing well with experimental studies in silicon and GaAs [139]. Due to interference of the system, e.g. working with a 50 Hz AC current, other noise spectral density dependences also occur and add up with the low-frequency noise, $S_q(\tilde{\omega}) = A|\tilde{\omega}|^{-\gamma}$. These additional noise sources directly depend on the exact experimental setup and can often be filtered directly. However, the low-frequency spectrum is dominated by '1/f-noise' with a power law with typical values for γ range from 0.7 to 2.3 [139, 175–178], but higher values are not unusual [179]. Protection against such charge noise can be obtained by operating the qubit system at a high symmetry point, where the transition to both asymmetric charge states is equal. At such a sweet spot, the ground state energy gap as a function of the detuning $\varepsilon = (V_1 - V_2)/2$ has an extremum, thus the qubit is immune to energy fluctuations in ε due to charge noise in first order [96, 140, 180–183]. However, second or higher order effects still limit the dephasing time.

2. Three-electron spin qubits

Taking the idea of electrical control and protection of the qubit against noise one step further leads ultimately to the three-spin qubit which can be controlled fully electrically. Some three-spin qubits also form a decoherence-free subspace (DFS) qubit implying that they are immune to all collective decoherence, i.e. decoherence which affects all spins in one qubit, many nearby qubits, or ideally in the full quantum computer in the same way [184]. There are many different ways of implementing such a three-spin qubit. In this review we cover the exchange-only (EO) qubit [2], the spin-charge qubit [7], the hybrid qubit [8, 9, 11], the resonant exchange (RX) qubit [5, 6], and on the always-on exchange-only (AEON) qubit [16]. All of these qubit implementations are realized using three electrons in either a single quantum dot, double quantum dot (DQD), or triple quantum dot (TQD) depending on the qubit implementation. The full spin-space is spanned by $\mathcal{H}_{3\text{spin}} = \mathcal{H}_{1/2} \otimes \mathcal{H}_{1/2} \otimes \mathcal{H}_{1/2}$ which can be divided into two spin-$\frac{1}{2}$ and one spin-$\frac{3}{2}$ subspace, thus, $\mathcal{H}_{3\text{spin}} = \mathcal{H}_{1/2} \oplus \mathcal{H}_{1/2} \oplus \mathcal{H}_{3/2}$, where $\mathcal{H}_\sigma$ denotes the Hilbert space corresponding to the irreducible representation of SU(2) with total spin σ. In other words the Hilbert space can be separated into a $S = 3/2$ quadruplet and a degenerate $S = 1/2$ doublet [4, 185] which can further be split into a high and low energy qubit by an external magnetic field along the z-axis. The qubit states for these qubits are chosen in such a way that they have identical spin quantum numbers, both the total spin $S = 1/2$ and the total spin projection along the quantization axis $S_z = 1/2$ giving rise to immunity against global magnetic fluctuations. Different qubit realizations are introduced and discussed in detail in the following sections and we postpone a more detailed discussion about DFSs and further dynamical (noise) decoupling schemes in three spin qubits to section 4 and refer to a related review [184] for more details. However, before delving into the qubit implementations, some basic properties of electrons in TQDs need to be introduced.

For the description of TQDs, the extended Hubbard Hamiltonian (see equation (1) for $N = 3$ quantum dots) is an appropriate choice throughout almost the full review since it combines all key features of the three-spin qubits while the expressions are still succinct. Therefore, in this review we skip a realistic and comprehensive discussion of the exact energy levels and their microscopic dependence on gate voltages, the geometry of the TQD, the number of electrons, and the magnetic field [186–192] and only briefly introduce the key points while sticking to the Hubbard model in the remainder. A comprehensive study of these can be found in the related review [192].

2.1. Electrostatic properties of electrons in a TQD

As a first step to visualize, navigate, and find relevant states in the large Hilbert space of multi-electron states in a TQD, the charge stability diagram of the TQD is helpful as it highlights the charge transitions between different occupancies of

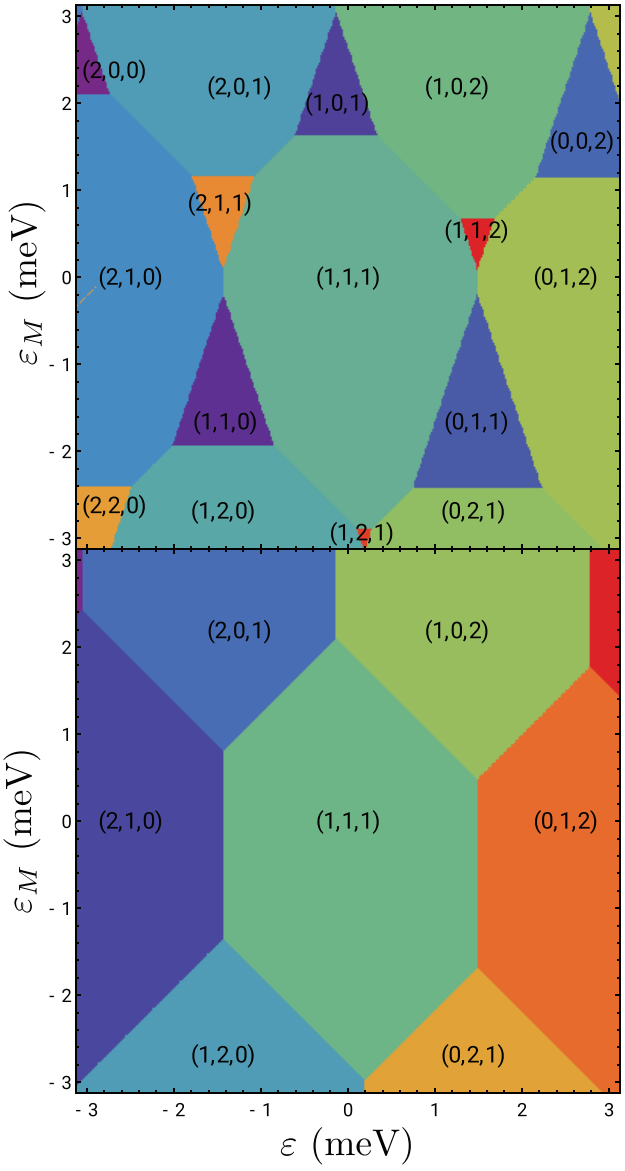

Figure 4. Charge stability diagram of a triple quantum dot (TQD) with realistic parameter settings as a function of detuning parameters ε and ε_M from equation (25) (a) for an arbitrary number of electrons and (b) for a fixed number $n = 3$ of electrons. Both diagrams were obtained using a capacitance model of the TQD adapted from [51, 195].

multiple QDs [51, 58, 192–197] and neglects all spin related effects. To generate the charge stability diagram, we use here a modified version of the algorithm used in [198, 199] with a maximum number of (four) electrons in the TQD and a fixed rate for the electron tunneling between the dots. Figure 4 shows the low electron occupancy part of the charge stability diagram as a function of the two detuning parameters defined as

$$\varepsilon = (\mu_1 - \mu_3)/2, \tag{9}$$

$$\varepsilon_M = \mu_2 - (\mu_1 + \mu_3)/2, \tag{10}$$

for a fixed value of the average voltage $eV_{\text{av}} = (\mu_1 + \mu_2 + \mu_3)/3$. The parameter $\mu_i = \sum_{j=1}^{3} v_{i,j} V_j$ with $i, j = 1, 2, 3$ is the chemical potential of QD i given by the gate voltages V_i (see figure 2)

underneath each QD and $v_{i,j}$ describes the electrostatic interaction between QD i and the gate underneath QD j and depends on the charging energies, the additional energy one has to pay to add another electron to the corresponding dot [51, 193]. In few words, the $v_{i,j}$ describe how each gate has to be adjusted in order to change the chemical potential in each dot. Taking into account a finite coupling between the QDs due to cross capacitance effects, i.e. adding an electron in one QD changes the potential of the neighboring QD, the typical honeycomb structured diagrams shown in figure 4 are obtained.

In the center of the charge stability diagram for a fixed value of V_{tot} lies the (1,1,1) charge configuration regime with one electron in each QD surrounded by the six asymmetric charge configurations, (2,0,1), (1,0,2), (1,2,0), (0,2,1), (2,1,0), and (0,1,2) with the same number of electrons. Here, (l,m,n) labels a charge configuration with l electrons in the left QD, m electrons in the center QD, and n electrons in the right QD. Each of these asymmetric states except the last two are interlinked with the (1,1,1) charge configuration through a single hopping event while the last two states require two hopping events. States with triple occupation of a single QD are located at more extreme values of the detuning parameters. Note that the average voltage V_{av} roughly sets the total number of electrons in the TQD since the number of electrons is allowed to change due a coupling to the leads.

Special points of interest for quantum computation and qubit implementations are typically centered inside a charge configuration regime or located at the charge transition points where multiple charge configurations intersect since these points provide a high symmetry with respect to charge configurations.

2.2. Spin properties of three-spin qubits in TQDs

In a second step, spin and orbital effects are reintroduced which in general further subdivides the stability diagram. The Hilbert space of three electron-spins with spin $\frac{1}{2}$ in a TQD is $\mathcal{H}_{3\text{spin}} = \mathcal{H}_{1/2} \otimes \mathcal{H}_{1/2} \otimes \mathcal{H}_{1/2}$ and combined with only a single available orbital in each QD contains in total 20 possible states (220 possible states for a second available orbital, e.g. additional valley). There are eight states with a symmetric charge configuration (1, 1, 1), and two states with asymmetric charge configurations (2, 0, 1), (1, 0, 2), (1, 2, 0), (0, 2, 1), (2, 1, 0), and (0, 1, 2) each. States with a triply occupied QD (3, 0, 0), (0, 3, 0), and (0, 0, 3) are excluded due to the restriction to a single available orbit in each dot.

The corresponding spin Hilbert space $\mathcal{H}_{3\text{spin}} = \mathcal{H}_{3/2} \oplus \mathcal{H}_{1/2} \oplus \mathcal{H}_{1/2}$ can be divided into a quadruplet $\mathcal{H}_{3/2}$ with effective spin-3/2 and two degenerate doublets $\mathcal{H}_{1/2}$ which combined with different orbits and restricted to the total spin $S = 1/2$ subspace gives rise to a two-fold degenerate subspace $\mathcal{H}_{+1/2} \oplus \mathcal{H}_{-1/2}$. This subspace is effectively decoupled from the $S = 3/2$ subspace considering weak magnetic field gradients [23] and weak spin orbit interaction [22]. Leakage into the $S = 3/2$ and $S_z = \pm 1/2$ states is suppressed by exchange [23]. These two subspaces, distinguished by $S_z = \pm 1/2$, are interchangeable with respect to the exchange interaction, thus an external magnetic field allows us to focus on only one of them, e.g. $S = 1/2$, $S_z = +1/2$. Without loss of generality, the $S = S_z = +1/2$ subspace is spanned by the basis states

$$|0\rangle \equiv |s\rangle_{13}|\uparrow\rangle_2, \tag{11}$$

$$|1\rangle \equiv \sqrt{\frac{2}{3}}\,|t_+\rangle_{13}|\downarrow\rangle_2 - \frac{1}{\sqrt{3}}|t_0\rangle_{13}|\uparrow\rangle_2, \tag{12}$$

$$|2\rangle \equiv |s\rangle_{11}|\uparrow\rangle_3, \tag{13}$$

$$|3\rangle \equiv |\uparrow\rangle_1|s\rangle_{33}, \tag{14}$$

$$|4\rangle \equiv |\uparrow\rangle_1|s\rangle_{22}, \tag{15}$$

$$|5\rangle \equiv |s\rangle_{22}|\uparrow\rangle_3, \tag{16}$$

$$|6\rangle \equiv |s\rangle_{11}|\uparrow\rangle_2, \tag{17}$$

$$|7\rangle \equiv |\uparrow\rangle_2|s\rangle_{33}, \tag{18}$$

with the two-electron singlet state $|s\rangle_{ij} \equiv (|\uparrow\rangle|\downarrow\rangle - |\downarrow\rangle|\uparrow\rangle)/\sqrt{2}$ and the two-electron triplet states $|t_0\rangle_{ij} \equiv (|\uparrow\rangle|\downarrow\rangle + |\downarrow\rangle|\uparrow\rangle)/\sqrt{2}$ and $|t_+\rangle_{ij} \equiv |\uparrow\rangle|\uparrow\rangle$ occupying QD i and QD j. Since the doubly occupied states $|2\rangle$, $|3\rangle$, $|4\rangle$, and $|5\rangle$ are obtained from $|0\rangle$ and $|1\rangle$ via the motion of a single electron and the states $|6\rangle$ and $|7\rangle$ requires at least two hopping events, the latter two states are neglected in most studies. The motivation comes from perturbation theory where these terms only add higher order corrections in the relevant parameter regimes [3, 5, 6, 16, 20, 22, 24]. The resulting matrix representation of the Hamiltonian equation (1) in this basis up to a global energy shift, is [3]

$$H = \begin{pmatrix} 0 & 0 & t_l/2 & t_r/2 & t_r/2 & t_l/2 \\ 0 & 0 & \sqrt{3}\,t_l/2 & -\sqrt{3}\,t_r/2 & -\sqrt{3}\,t_r/2 & \sqrt{3}\,t_l/2 \\ t_l/2 & \sqrt{3}\,t_l/2 & E_2 & 0 & 0 & 0 \\ t_r/2 & -\sqrt{3}\,t_r/2 & 0 & E_3 & 0 & 0 \\ t_r/2 & -\sqrt{3}\,t_r/2 & 0 & 0 & E_4 & 0 \\ t_l/2 & \sqrt{3}\,t_l/2 & 0 & 0 & 0 & E_5 \end{pmatrix}. \tag{19}$$

The symmetric tunneling parameters are $t_{12} = t_{21} \equiv t_l/\sqrt{2}$, $t_{23} = t_{32} \equiv t_r/\sqrt{2}$, and $t_{13} = t_{31} = 0$ and the simplified expressions for the charging energies of the states are

$$E_2 = \varepsilon - \varepsilon_M + U, \tag{20}$$

$$E_3 = -\varepsilon - \varepsilon_M + U, \tag{21}$$

$$E_4 = \varepsilon + \varepsilon_M + U, \tag{22}$$

$$E_5 = -\varepsilon + \varepsilon_M + U. \tag{23}$$

In this case, all of the charging energies E_i depend only on the two detuning parameters

$$\varepsilon = (V_1 - V_3)/2, \tag{24}$$

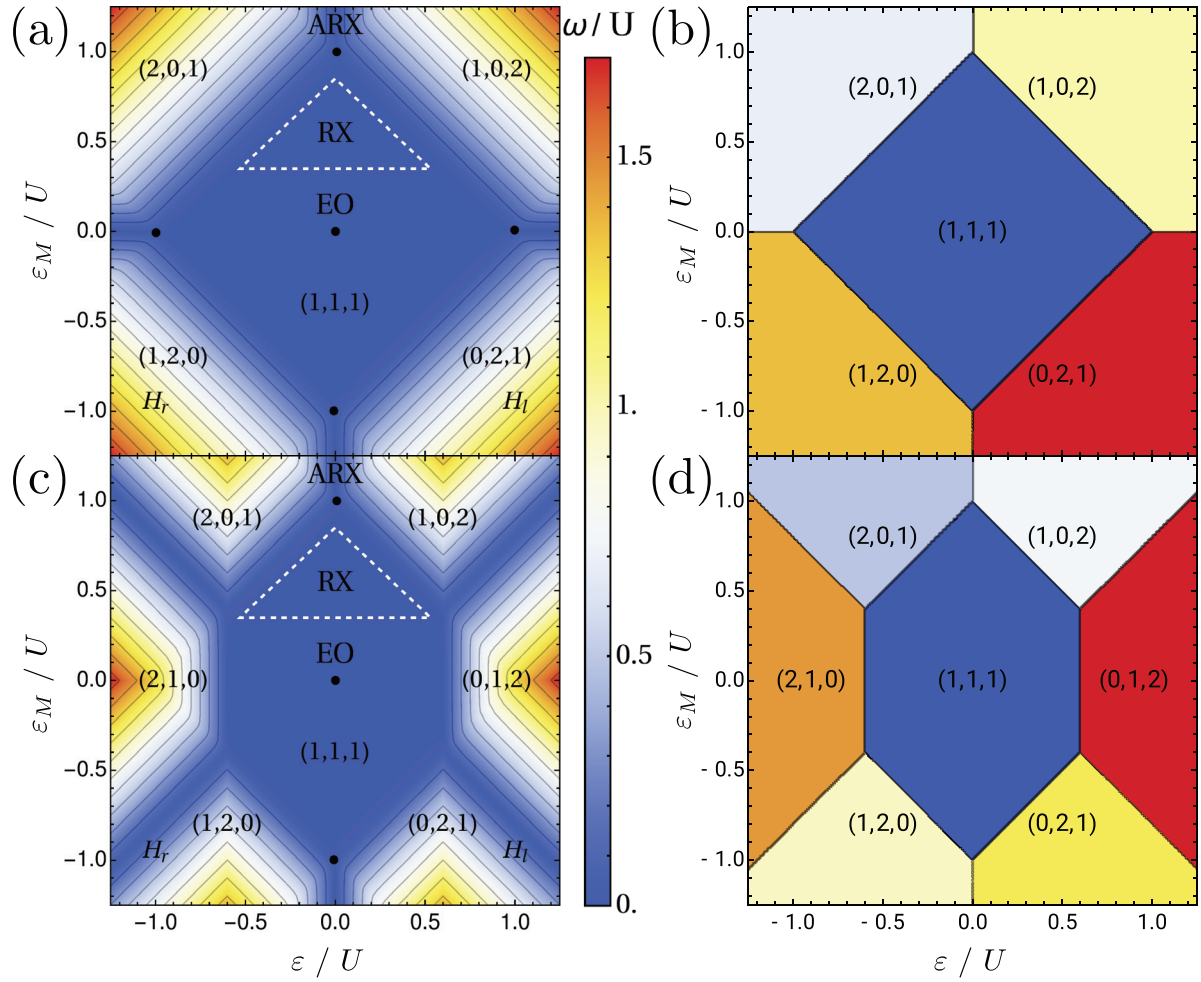

Figure 5. (Left column) Energy landscape of the ground-state energy gap ω of a three-spin qubit as a function of the detuning parameters ε and ε_M in a triple quantum dot in units of the charging energy U. For the tunneling parameters the ratios $t_l = 0.022\,U$ and $t_r = 0.015\,U$ and for the mutual charging energy $U_C = 0.2\,U$ are used. Maneuvering through the (ε, ε_M) plane one can access various parameter regimes that allow the use of different qubit implementations in different charge configurations (l,m,n), where l electrons are in the left, m electrons in the center, and n electrons in the right QD. We indicated the double sweet spots (DSS) (black dots), the location of the exchange-only (EO) qubit, the resonant exchange (RX) qubit (dashed triangle), the asymmetric resonant exchange (ARX) qubit, and the left and right hybrid ($H_{l,r}$) qubit highlighted. (Right column) Charge ground state of a three-spin qubit in the absence of tunneling, $t_l = t_r = 0$ as a function of the detuning parameters ε and ε_M in a triple quantum dot in units of the charging energy U. For plots (a) and (b) the states with (2,1,0) and (0,1,2) charge configurations are neglected corresponding to a large cross-charging energy $U_C \lesssim U$ while for plots (c) and (d) small a value $U_C = 0.2\,U$ is considered. Figures taken from [3, 200].

$$\varepsilon_M = V_2 - (V_1 + V_3)/2 + U_C, \tag{25}$$

and the adjusted charging energy $U = \tilde{U} - U_C$. In the general case $U_i \neq U_j$, where U_i is the charging energy in dot i, the expressions for the charging energies of the states are changed [16].

The logical choice for a qubit is the two-level system consisting of the ground state and the first excited state, energetically split by the ground-state energy gap ω. For $t_{l,r} \ll E_i$, these are essentially the states $|0\rangle$ and $|1\rangle$ with corrections $\propto t_{l,r}/E_i$. In figures 5(a) and (c) the ground-state energy-gap is plotted as a function of the two detuning parameters, ε and ε_M, with labels indicating the dominant charge configuration (a) excluding and (c) including the states $|6\rangle$ and $|7\rangle$. Figure 5 (right column) shows the charge ground state from equation (18) excluding (figure 5(b)) and including the states $|6\rangle$ and $|7\rangle$ (figure 5(d)). The logical qubit states, defined as the ground state and the first excited state, have different charge configurations depending on the exact location in the detuning space. In the (1,1,1) charge configuration regime the spin qubit states are $|0\rangle$ and $|1\rangle$ hybridized by the admixture of the asymmetric states $|2\rangle$, $|3\rangle$, $|4\rangle$, $|5\rangle$ (to a less degree also by $|6\rangle$ and $|7\rangle$) giving rise to a finite energy gap between the states ω.

2.3. Exchange-only (EO) qubit

The idea of all-electric qubit control ultimately leads to the exchange-only qubit which, as the name suggests, provides the possibility for full qubit control with only the exchange interaction [2]. Analogously to the ST qubit (see section 1.5), the exchange interaction originates from the hybridization of the logical qubit states with asymmetric charge states and can be precisely controlled by electrostatic control of the gates underneath and in between the QDs. In this section, we try

to provide an overview of preceding experimental and theoretical developments of the exchange-only qubit. The organization is as follows. We start with the model and subsequently follow with the single-qubit operations, where we discuss the two main types of experimental realizations. We discuss two-qubit operations and the decoherence of our qubit due to environment separately in the next sections 3 and 4.

2.3.1. Model. For the EO qubit the focus is on the eight-dimensional subspace with a symmetric (1, 1, 1) charge configuration which can be separated into a $S = 3/2$ quadruplet and a degenerate $S = 1/2$ doublet [4, 185, 201] whose degeneracy can be lifted by an external magnetic field aligned along the z-axis. We are interested in these doublets since they provide two two-level systems, each having identical quantum numbers, one being the total spin $S = 1/2$ the other being the projection of the total spin along the quantization axis $S_z = \pm 1/2$. For the $S_z = +1/2$ two-level system an appropriate basis is given by

$$|0_+\rangle \equiv |s\rangle_{13}|\uparrow\rangle_2 = \frac{1}{\sqrt{2}}(|\uparrow,\uparrow,\downarrow\rangle - |\downarrow,\uparrow,\uparrow\rangle), \tag{26}$$

$$\begin{aligned}|1_+\rangle &\equiv \sqrt{\frac{2}{3}}\,|t_+\rangle_{13}|\downarrow\rangle_2 - \frac{1}{\sqrt{3}}|t_0\rangle_{13}|\uparrow\rangle_2 \\ &= \frac{1}{\sqrt{6}}(2|\uparrow,\downarrow,\uparrow\rangle - |\uparrow,\uparrow,\downarrow\rangle - |\downarrow,\uparrow,\uparrow\rangle),\end{aligned} \tag{27}$$

while for the $S_z = -1/2$ two-level system all spins are flipped,

$$|0_-\rangle \equiv |s\rangle_{13}|\downarrow\rangle_2 = \frac{1}{\sqrt{2}}(|\downarrow,\downarrow,\uparrow\rangle - |\uparrow,\downarrow,\downarrow\rangle), \tag{28}$$

$$\begin{aligned}|1_-\rangle &\equiv \sqrt{\frac{2}{3}}\,|t_-\rangle_{13}|\uparrow\rangle_2 - \frac{1}{\sqrt{3}}|t_0\rangle_{13}|\downarrow\rangle_2 \\ &= \frac{1}{\sqrt{6}}(2|\downarrow,\uparrow,\downarrow\rangle - |\downarrow,\downarrow,\uparrow\rangle - |\uparrow,\downarrow,\downarrow\rangle).\end{aligned} \tag{29}$$

A special feature of the EO qubit is the possibility for two different qubit encodings using either the 'subspace' or the 'subsystem' encoding. For the subspace, as the name suggests, the qubit states are encoded in a real subspace of the total Hilbert space, either in the positive two-level system, $|0\rangle = |0_+\rangle$ and $|1\rangle = |1_+\rangle$, or in the negative two-level system, $|0\rangle = |0_-\rangle$ and $|1\rangle = |1_-\rangle$. This implementation needs a sufficiently strong magnetic field along the quantization axis to break the degeneracy of the doublets and energetically favor one of the two-level systems depending on the sign of the magnetic field. Here, we use the convention that the positive ($S_z = +1/2$) subspace qubit is energetically favorable. Particularly, fine-tuning of the confinement potentials and adjusting the strength of the magnetic field energetically separate the doublet states from the quadruplet states [202] in Si [192, 203] and GaAs [192, 202]. For a finite magnetic field, one of the two-level systems is pushed down in energy, such that it forms the well isolated states, hence, reducing orbital relaxation.

The second type of encoding is the 'subsystem' qubit which utilizes all states with $S = 1/2$, thus, $|0\rangle = |0_\pm\rangle$ and $|1\rangle = |1_\pm\rangle$ giving rise to a qubit implementations with one leftover degree of freedom [2, 19]. In the absence of a magnetic field there are parameter regimes where the orbital energies dominate pushing the quadruplet up in energy and the doublets down in energy [192, 203] allowing for the implementation of such a subsystem qubit. It is crucial for this implementation that there are no interactions which couple the $|0_\pm\rangle$ states differently than the $|1_\pm\rangle$ states. Under this condition, the two-level systems are not entangled and the additional degree of freedom can be rewritten into a global degree of freedom allowing for a well-defined qubit [19]. In realistic systems, the exchange interaction fulfills these conditions while local magnetic field gradients and spin–orbit coupling violate it.

In the low energy subspace in the (1, 1, 1) charge configuration regime a Schrieffer–Wolff transformation yields (analogously to the ST qubit) an effective Heisenberg Hamiltonian for the hybridized states, however, with three exchange coupling parameters

$$H_{\text{eff,TQD}} = \frac{J_{12}}{4}\boldsymbol{\sigma_1}\cdot\boldsymbol{\sigma_2} + \frac{J_{23}}{4}\boldsymbol{\sigma_2}\cdot\boldsymbol{\sigma_3} + \frac{J_{13}}{4}\boldsymbol{\sigma_1}\cdot\boldsymbol{\sigma_3}. \tag{30}$$

For a linear arrangement and neglecting superexchange $J_{13} = 0$. The expressions for the exchange couplings depend on the choice of the subspace taken into account. Since the states with (2,1,0) and (0,1,2) charge configurations are not directly coupled to the (1,1,1) charge states they are usually neglected for the derivation of the exchange couplings. In this case, the exchange couplings are given by [3]

$$J_{12} = J_l = 2t_l^2 U/\left[U^2 - (\varepsilon - \varepsilon_M)^2\right], \tag{31}$$

$$J_{23} = J_r = 2t_r^2 U/\left[U^2 - (\varepsilon + \varepsilon_M)^2\right]. \tag{32}$$

More general expressions which include different Coulomb terms U_i in each QD are given in [16] and are not shown here. The resulting energy splitting between the qubit states is given by [6]

$$\omega = \sqrt{J_l^2 + J_r^2 - J_l J_r}. \tag{33}$$

2.3.2. Conventional single qubit operations. The exchange-only qubit allows for all-electrical control of the qubit rotations with only the exchange interactions allowing for J_l and J_r two independent axes of control. In the hybridized qubit basis, $|0\rangle$ and $|1\rangle$, the Heisenberg Hamiltonian from equation (30) can be expressed as

$$H_{\text{qubit}} = E_0\mathbb{1}_2 - \frac{J}{2}\sigma_z - \frac{\sqrt{3}\,j}{2}\sigma_x \tag{34}$$

with the qubit Pauli matrices, $\sigma_z \equiv |0\rangle\langle 0| - |1\rangle\langle 1|$ and $\sigma_x \equiv |0\rangle\langle 1| + |1\rangle\langle 0|$, and the exchange energies $J \equiv (J_l + J_r)/2$ and $j \equiv (J_l - J_r)/2$. The first term $\propto E_0$ only contributes to a global phase of the qubit, thus, can be ignored. Note, that the rotation axes are provided by the sum and difference of the exchange interaction between the dots (see equations (31) and (32)), thus, the rotation axes corresponding to an exchange pulse of $J_{l,r}$ are not perpendicular on the Bloch sphere. To be

exact, the angle between the rotation axes corresponding to the pure exchange interactions J_{12} and J_{23} is 120°; a symmetric pulse $J_{12} = J_{23}$ provides rotations around the z-axis while the rotation around the x-axis is given by a three-step pulse due to the exchange interaction always being positive. This can be visualized using the classic Euler angle construction as rotations around three axes can simulate a rotation around any axis. Hence, in total four serial exchange pulses (for $J_{13} \neq 0$ three pulses) are always sufficient to create arbitrary single qubit operations [2]. In experiments, there are two ways of controlling the exchange interaction which differentiate in the choice of the operating gates.

Tilting based exchange pulses. The usual way to control the exchange interaction in a TQD is by varying the gate potentials underneath each QD adapted from DQDs [78, 118] and successfully demonstrated for TQDs [59, 66, 67, 69, 70]. The exchange interactions $J_{l,r}(\varepsilon, \varepsilon_M)$ are controlled by adjusting the gate potentials, maneuvering through the detuning space spanned by the two detuning parameters ε and ε_M. An exchange-pulse, thus, requires the movement of the point of operation to the correct spot at which J_l and J_r take the desired values for the single qubit operation. Visualized in parameter space, this corresponds to maneuvering to a region where either J_l or J_r dominates the exchange interaction. In a ST qubit, this corresponds to a tilting of the QD potential while for the EO qubit both detuning parameters play a role (shown schematically in figure 6 top row). Precisely, a pure J_l-pulse requires $|\varepsilon - \varepsilon_M| \gg |\varepsilon + \varepsilon_M|$ and a pure J_r-pulse requires $|\varepsilon - \varepsilon_M| \ll |\varepsilon + \varepsilon_M|$, while the requirement for the (1,1,1) charge configuration regime $|\varepsilon \pm \varepsilon_M| < U$ must still hold. Since the detuning parameters have to be operated adiabatically and are located far away in detuning space, this limits the speed of arbitrary qubit rotations since they require a sequence of J_l and J_r pulses. To speed up gate operations, optimized pulse sequences can be used. Universal control has been demonstrated experimentally in the two most common materials, Si [69] and GaAs [4, 5, 54, 59, 60, 66–68], yielding control over two independent rotation axes with both exchange couplings exceeding $J \approx 100$ MHz ≈ 40 μeV [69]. Strong dephasing from hyperfine interactions in GaAs devices [59, 67] and charge noise in Si devices [69], however, limits the fidelity of the qubit rotations. A significant improvement is to be expected by operating the qubit at charge noise sweet spots [6, 20, 24], using dynamical decoupling sequences [184, 204–206], and reported using devices with nuclear-spin-free isotopes [69].

2.3.3. Symmetric operation point (AEON qubit). Another concept for improved single qubit rotations is the symmetric operation point (SOP) [96], where one keeps the qubit at a high symmetry point while operating the qubit, i.e. never leaving the SOP in detuning space. Taking a closer look at the expression for the exchange couplings in equations (31) and (32) one finds that such operation is possible via controlling the tunneling amplitudes $t_{l,(r)}$ which also leads to control over the exchange couplings due to $J_{l,(r)} \propto t^2_{l,(r)}$. To be exact,

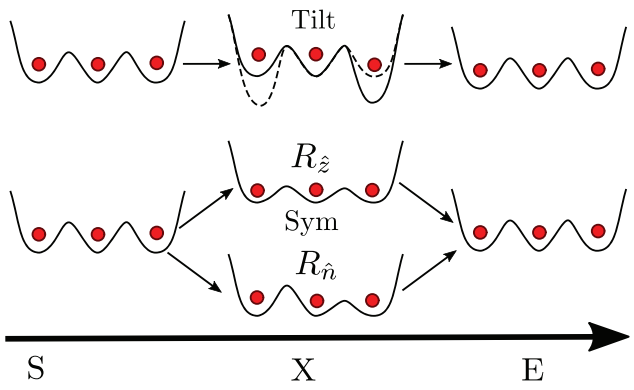

Figure 6. Schematic illustration of the two methods for operating the qubit described in the main text. The black lines represent the energy potential of the TQD which is filled with three electrons (red dots). The qubit is in some initial state at time S. Then, a single-qubit operation, tilt or symmetric, is performed at time X, leaving the qubit in some final state at time E. For the tilt method, the detuning, the energy potential difference between the quantum dots, is changed to operate the single-qubit gates. The solid and the dashed line correspond to two linear independent rotations. For the symmetric method the tunnel-barrier, the height of the energy potential separating the quantum dots, is lowered for the gate operation. A symmetric lowering corresponds to a rotation around the $\hat{z}$-axis, while an asymmetric lowering causes a rotation around some axis $\hat{n}$ [16].

this way to control exchange was already proposed in the original paper by Loss and DiVincenzo [123]. Since recent architectures for quantum dot devices [78, 79] always include an additional (static) gate to set the tunnel coupling between the dots the symmetric operation point (SOP) does not require new quantum dot architectures [96, 183].

The AEON qubit [16] is a modified version of the original EO qubit [2] where the exchange interaction is either completely turned on or completely turned off while staying at a favorable operation point, therefore, a candidate for such a symmetric implementation. As already shown, full control over the qubit is possible through the two exchange interactions $J = (J_l + J_r)/2$ and $j = (J_l - J_r)$ consisting of the left (right) exchange coupling $J_{l,(r)}$ with the approximated expression $J_{l,r} = 2t^2_{l,r}U/[U^2 - (\varepsilon \mp \varepsilon_M)^2]$ (for the general expression see [16]). The specific expressions for the exchange coupling in the AEON qubit allow for the existence of a double sweet spot (DSS) which is insensitive to noise in lowest order with respect to both detuning parameters simultaneously (a more detailed discussion and definition follows in section 4.2). The DSS for the AEON qubit is located directly in the center in the energy landscape of the ground-state energy gap $\omega = \sqrt{J^2 + 3j^2}$ (see figure 5), thus, possessing the highest symmetry with respect to all (directly tunnel coupled) asymmetric charge configurations. Since the location of the DSS is provided by the geometry of the TQD, thus, independent of the tunneling parameters, it still exists even for less symmetric geometries albeit not located in the center [16]. This allows for operating the qubit by tuning the tunneling parameters while staying permanently on the DSS. Setting the tunneling parameters to be symmetric $t_l = t_r$ (turning on both exchange coupling simultaneously) results in a rotation around the z-axis

(see figure 6 middle row), while setting $t_l = (\sqrt{6}+\sqrt{2})t_r/2$ results in a rotation around the $\hat{n} = -(\hat{x}+\hat{z})/\sqrt{2}$-axis (see figure 6 bottom row) which together with a rotation around the z-axis causes a rotation around the orthogonal x-axis [16]. Therefore, a three-pulse sequence is sufficient for arbitrary single qubit gates which is one pulse less than needed for the conventional EO qubit [2]. Since the exchange couplings are either completely turned on or completely turned off, symmetric gate operations, which control the tunnel barriers $t_{l,r}$ directly, are required. Simultaneously, this makes the AEON qubit robust against leakage induced by a magnetic field gradient [23], albeit to a lesser degree than the RX qubit (see section 2.3.4) due to smaller exchange couplings.

Additionally, the symmetric way of operation allows for heavy filtering of the detuning gates together decreasing the effects of the charge noise on the qubit. However, time-dependent control of the tunneling parameters also opens another channel for coupling noise to the qubit via the tunnel couplings [3]. Experiments in operating a DQD symmetrically demonstrate a significant improvement of the qubit decoherence times and overall fidelities compared to the standard implementation using detuning as control [96, 183], therefore, indicating that noise coupled to the qubit via detuning dominates over noise coupled via tunneling. Up to date there is no experimental demonstration of symmetric operation of three-spin qubits, however, experiments successfully demonstrated control over various QDs [207].

The initialization techniques, read-out schemes, and physical implementation of the AEON qubit are identical to the conventional EO qubit. We note however that initialization and read-out using spin-to-charge conversion is not optimal for this implementation since one needs to traverse the RX regime in parameter space [16, 27].

2.3.4. Resonant exchange operation (RX qubit). The RX qubit [5, 6, 15] is a modified version of the EO qubit where the exchange interaction is always turned on, while the qubit is operated (as the name suggests) through a resonant modulation of the exchange interaction. As a first thought this may sound like a step backwards to the original spin-$\frac{1}{2}$ qubit which depends on the (slow) qubit rotation through ESR [78] or EDSR [208], however, due to the permanently turned on exchange interaction which induces a strong qubit splitting, the energy gap can be modulated electrically and also much more strongly, giving rise to high fidelity gates and gate times on the order of nanoseconds [5, 27].

Analogously to the EO qubit, the qubit states are given by equations (26) and (27), and therefore, still located inside the (1, 1, 1) charge configuration regime. However, due to $\varepsilon_M \gg |\varepsilon|$ the qubit state are strongly hybridized by the admixture of the (2, 0, 1) and (1, 0, 2) charge configurations resulting in a large energy gap between the qubit states while the influence of the (1, 2, 0) and (0, 2, 1) charge configurations is negligible. Inside the $(\varepsilon, \varepsilon_M)$-landscape of the ground state energy gap the RX regime is located in the upper part of the diamond formed (1, 1, 1) charge regime (white triangle in figure 5). The RX qubit Hamiltonian in its eigenbasis with a modulated detuning $\varepsilon \to \varepsilon + \delta\varepsilon$ takes the form [3, 6]

$$H_{\text{qubit}} = \frac{\hbar}{2}\omega_{\text{RX}}\sigma_z + \delta\varepsilon\,\eta\sigma_x \tag{35}$$

with the resonance frequency $\hbar\omega_{\text{RX}} = \sqrt{J^2+3j^2}$, the modulation coupling $\eta = \frac{1}{2\omega}[J(\partial J/\partial\varepsilon) + 3j(\partial j/\partial\varepsilon)]$, and the exchange couplings $J = (J_l + J_r)/2$ and $j = (J_l - J_r)$. Due to the negligible influence of the (1, 2, 0) and (0, 2, 1) charge configurations the exchange coupling is approximated by $J_{l,r} = t_{l,r}^2/(U - \varepsilon_M \pm \varepsilon)$ [3, 6, 20].

Rabi oscillations corresponding to qubit rotations become accessible through resonant driving of the detuning ε near the qubit's resonance frequency ω_{RX}, thus, $\delta\varepsilon = f(\tau)\cos(\nu\tau + \phi)$ with an adjustable phase ϕ, while the modulation amplitude $f(\tau)$ varies slowly (compared to ω_{RX}) in time τ. Near resonance, $\delta \ll \omega_{\text{RX}}$ with $\delta = \nu - \omega_{\text{RX}}$, the Rabi frequency is given within the rotating frame approximation by [6]

$$\Omega(\tau) \approx \frac{f(\tau)}{\hbar}\frac{\sqrt{3}\,t^2}{(U-\varepsilon_M)^2}, \tag{36}$$

while the axis of rotation is set by the adjustable phase ϕ of the driving. Experiments in a GaAs TQD device have demonstrated π rotations of the qubit around two axes of control on nanosecond time scales, $t_{\text{gate}} = 2.5$ ns [5, 27]. Combined with a CPMG coherence time $T_2 \approx 10$ μs, this allows for more than 10^3 coherent gates [5]. In this experiment, the resonance detuning is affected by the Overhauser fields which causes additional dephasing and is therefore the limiting factor for the coherence time. Results from a more recent experiment confirm that the limitation is caused by nuclear spins for weak driving, while for strong driving charge noise is the limiting factor [27]. Interestingly, operating the RX at a symmetric operation point provides only a slight improvement (a more detailed discussion follows in section 4.2). An experimental realization in a silicon device (Si/SiGe or SiMOS) should significantly improve the RX qubit for weak driving due to the absence of nuclear spins under isotopic purification [69, 79, 100, 209–211].

The initialization techniques, read-out schemes, and physical implementation are identical to the conventional EO qubit. As a remark, both initialization and read-out schemes using either spin-to-charge conversion or cavity quantum electrodynamics (cQED) based techniques should be feasible due to the short distance in $(\varepsilon, \varepsilon_M)$ parameter space with respect to the (2, 0, 1) and (1, 0, 2) charge configurations which strongly hybridize the qubit states [6, 17, 18].

Other methods. Up to this point we have only considered a linearly aligned TQD which is used in most experimental setups. In the following, we briefly introduce triangularly arranged TQD systems (TQD molecules) where we mainly focus on the implementation of qubit rotations in such a system which differ from the linear case. For more details about the energy structure and properties we refer to the review by Chan-Yu Hsieh (see [192]) or the original works [71, 72]. In

addition to the exchange interaction J_{13} between the first and the last dot an (equilateral) triangular shape adds another feature, the chirality, to the system. This allows for a new set of qubit states in the same $S = 1/2$ and $S_z = \pm 1/2$ subspace

$$|+\rangle = \frac{1}{\sqrt{3}}\left(|\uparrow\uparrow\downarrow\rangle + e^{+i\frac{2\pi}{3}}|\uparrow\downarrow\uparrow\rangle + e^{+i\frac{4\pi}{3}}|\downarrow\uparrow\uparrow\rangle\right), \quad (37)$$

$$|-\rangle = \frac{1}{\sqrt{3}}\left(|\uparrow\uparrow\downarrow\rangle + e^{-i\frac{2\pi}{3}}|\uparrow\downarrow\uparrow\rangle + e^{-i\frac{4\pi}{3}}|\downarrow\uparrow\uparrow\rangle\right), \quad (38)$$

which are the eigenstates of the chirality operator [71] with the eigenvalues $\chi = \pm 1$. A unitary transformation connects them with the conventional eigenstates from equations (26) and (27). The low-energy subspace can also be approximated by a Heisenberg exchange Hamiltonian [72], however, the exchange couplings include additional terms arising from the circular structure and chirality [75, 212–214]. Applying an in-plane electric field breaks the symmetry of the system and gives rise to terms $\propto \sigma_y$ in the qubit space, corresponding to rotations around the y-axis on the Bloch sphere [74, 75]. Combining the in-plane electric field with spin–orbit effects, very fast Rabi oscillations between the chiral qubit states are proposed with $\tau_{\text{Rabi}} = 0.1\text{–}10^3$ ps depending on the realization of the device [215]. Additionally, the ring structure allows for the application of topologically protected quantum computation due to the non-trivial phase an electron acquires when traveling around a circle [73, 192]. Since this is beyond the scope of this review, we end the discussion of triangularly shaped TQDs and continue with further qubit implementations of three-spin qubits.

2.4. Spin-charge qubit

The spin-charge qubit is a unique implementation for a three-spin qubit since all three electrons are located in a single quantum dot occupying the three lowest orbitals [7]. The qubit states are

$$|1\rangle \equiv |s\rangle_{01}|\downarrow\rangle_2, \quad (39)$$

$$|0\rangle \equiv \sqrt{\frac{2}{3}}\,|t_-\rangle_{01}|\uparrow\rangle_2 - \frac{1}{\sqrt{3}}|t_0\rangle_{01}|\downarrow\rangle_2, \quad (40)$$

where each orbital, 0,1,2, is occupied by a single electron with the qubit states corresponding to the $S = 1/2$ and $S_z = -1/2$ subspace (see section 2.2). Orbital relaxation processes can be suppressed by designing the confinement potential in such a way that the $S = 1/2$ and $S_z = -1/2$ two-level system form the ground and the first excited state [187–192]. In this sense, the qubit implementation is very similar to the exchange-only qubit where the quantum dot (position degree of freedom) is interchanged with the orbital (orbital degree of freedom). Therefore, single qubit rotations are not possible anymore through conventional electric control, i.e. control over the exchange interaction through biasing of the gate voltages underneath or in-between the QDs. Instead of controlling the detuning or the barrier between the QDs one can acquire single-qubit rotations by controlling the confinement potential, particularly, the eccentricity of the confinement potential. Going beyond the Hubbard Hamiltonian and considering electrons in an elliptic confinement potential with eccentricities ω_x and ω_y the Hamiltonian in the qubit space can be written as [7, 216]

$$H_{\text{qubit}} = b_x\sigma_x + b_z\sigma_z + b_0\mathbb{1}_2. \quad (41)$$

The parameters are $b_x = \sqrt{3}\,(V_{0220} - V_{1221})/2$, $b_z = -V_{0110} + (V_{1221} + V_{0220})/2$, and $b_0 = V_{0101} + V_{1212} + V_{0202}$ with the usual matrix elements $V_{o_1o_2o_3o_4} = \langle o_1, o_2|\mathcal{V}_{\text{Coulomb}}|o_3, o_4\rangle$ and $o_i \in \{0, 1, 2\}$ originating from the long-range Coulomb interaction. A direct comparison of equations (41) and (34) shows that the matrix elements of the form $V_{o_1o_2o_2o_1}$ resemble an orbital exchange interaction, thus, $V_{0110} \sim J_l$, $V_{1221} \sim J_r$, and $V_{0220} \sim J_{13}$ (omitted in equation (34)). While the explicit expressions can be found in [216], the main result is a different dependence of b_x and b_z with respect to the eccentricity ratio $r \equiv \omega_x/\omega_y$ which both can be electrically adjusted by the gates. In the presence of a fixed magnetic field, this allows for fast electrically driven single qubit gates with sub-nanosecond gate times ($\tau_g \approx$ 1–10 ps) in GaAs and faster in silicon due to stronger confinement [7].

The next requirement for quantum computation are feasible read-out and initialization schemes. In the case that the qubit states (see equations (39)–(40)) are the ground states, the initialization is trivial and just a matter of thermalization [7]; this, however, can be slow. In the general case initialization techniques may be adapted from the EO qubit or the ST qubit; a singlet state is initialized in an isolated QD and in a second step the adiabatic opening of the tunnel barriers allows for the tunneling of a third electron. For read-out, a destructive measurement is suggested that detects if a fourth electron is resonantly tunneling in the QD or not, following the same protocol as used for a single-spin qubit [7, 135]. Since the qubit states are not degenerate, read-out techniques using cavity quantum electrodynamics (cQED) should be adaptable [112, 114, 217, 218].

2.5. Hybrid qubit

The holy grail for quantum computation is claimed by the qubit implementation which allows most high-fidelity operations during its coherence time. There are basically two ways of winning the race, either the coherence time is increased or the gate time is decreased, i.e. making the qubit operations faster. While the exchange-only qubit and its derivations try to increase the coherence time the hybrid qubit (HQ) is a representative of the latter approach, which in short, combines the longevity of spin qubits and the fast qubit operations of a charge qubit [8]. Note, that this section is far from complete and only covers the core concepts and recent advances providing a first insight of the hybrid qubit and that the hybrid qubit deserves a review article on its own.

The HQ qubit is implemented in a double quantum dot (DQD) analogously to the ST-qubit, however, filled with three electrons. The qubit states are

$$|0\rangle \equiv |s\rangle_R|\downarrow\rangle_L, \quad (42)$$

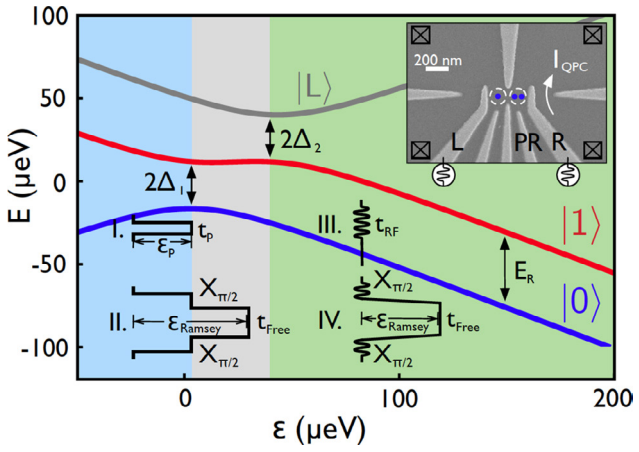

Figure 7. Main panel: Energy levels of the qubit states, $|0\rangle$ and $|1\rangle$, and the virtually occupied state $|L\rangle$ as a function of the detuning ε, the energy difference between QD potentials. Two tunneling parameters $\Delta_{1,(2)}$ (between ground (excited) state of the right QD and the ground state of the left QD) cause avoided crossings and couplings between the states. The green (blue) region is called the spin-region (charge-region), since there the qubit states differ by their spin (charge). The four pulse sequences show the experiments performed in [11]. Inset: SEM image of a hybrid qubit from the Eriksson group. Reprinted with permission from [11] Copyright 2016 by the American Physical Society.

$$|1\rangle \equiv -\sqrt{\frac{2}{3}}\,|t_-\rangle_R|\uparrow\rangle_L + \frac{1}{\sqrt{3}}|t_0\rangle_R|\downarrow\rangle_L, \tag{43}$$

where the right QD is doubly occupied while the left QD only singly occupied (see SEM image in figure 7 inset) which corresponds to the $S = 1/2$ and $S_z = -1/2$ subspace (see section 2.2) and the (1,2,0) or (0,1,2) charge configuration regime of a TQD discussed above. While the lowest orbital allows the singlet state $|s\rangle_R$, the triplet states $|t_-\rangle_R$ and $|t_0\rangle_R$ are forbidden in the lowest orbital due to the Pauli exclusion principle, hence, occupy the first excited orbital [8]. Assuming that the described singlet and triplet states are lowest in energy [219, 220], higher excited singlets and triplets can be neglected due to fast spin conserving orbital relaxation processes [221] which immediately relaxes the higher state into the ground state. The essential difference between the HQ and the EO qubit are the use of a DQD instead of a TQD and the double occupation of the right QD which includes occupation of higher orbital states (only in the right QD). A second singlet state, $|L\rangle = |\downarrow\rangle_R|s\rangle_L$, becomes important which couples to the $|0\rangle$ via tunneling and gives rise to an additional exchange splitting between the qubit states $|0\rangle$ and $|1\rangle$ allowing for electrical control. In total there are three relevant states, the two qubit states, $|0\rangle$ and $|1\rangle$, and the virtually occupied state $|L\rangle$; all other states can be neglected in lowest order. Analogously to the EO qubit, the low-energy subspace Hamiltonian is approximated using a Schrieffer–Wolff transformation giving rise to a hybridization of the qubit states due to their coupling to the $|L\rangle$ state (the formal derivation and the explicit expressions can be found in the supplementary material of [8] and [222]). In contrast to the exchange-only qubit, one is unable to find a pure spin Hamiltonian for the effective Hamiltonian but needs the $t - J$-model to describe the low-energy subspace.

Arbitrary single qubit rotations require control of two independent axes; for the hybrid qubit, one axis of control is provided by the change of the energy splitting between the qubit states $\hbar\omega$ while the second axis is given by transitions between the qubit states. Projecting the low-energy Hamiltonian on the qubit space, one finds in particular

$$H_{\text{qubit}} = \frac{\hbar}{2}\omega\sigma_z + j\sigma_x. \tag{44}$$

The energy gap between the qubit states is dominated by the orbital singlet-triplet splitting E_{ST} in the doubly occupied QD, thus, $\hbar\omega = J + E_{\text{ST}} \approx E_{\text{ST}}$ since $|J| \ll |E_{\text{ST}}|$ (see main panel in figure 7). In particular one finds, $J \propto J_S + 3J_T$, where J_S is singlet exchange coupling due to the admixture of $|0\rangle$ with the virtual state $|L\rangle$ and J_T is the triplet exchange coupling from the admixture of $|1\rangle$ with $|L\rangle$. Control over the singlet-triplet E_{ST} splitting by changing the gate voltages in the QD [155, 223–225] gives rise to rotations around the z-axis, while rotations around the x-axis are given by transitions between the qubit states which are induced by the off-diagonal terms of the qubit Hamiltonian, $j \propto J_S + J_T$ with $J_{S,(T)} \propto t^2_{S,(T)}/\Delta E_{S,(T)}$. Here, $t_{S,(T)}$ is the tunnel amplitude and $\Delta E_{S,(T)}$ is the energy difference between the virtual state and the singlet (triplet) state. Therefore, either pulsing the tunnelings $t_{S,(T)}$ or the pulsing the energy differences $\Delta E_{S,(T)}$ give rise to adjustable transitions between the qubit states. Considering Si/SiGe as the QD host material, sub-nanosecond ($f = 10$ GHz) gate times have been predicted [8] and experimentally demonstrated [63]. Moreover, since both tunnel couplings t_S and t_T can be tuned independently (and also independently of E_{ST}), thus, also the ratio $r = t_S/t_T$, a larger set of elementary single qubit rotations becomes accessible. This provides a more 'fine-grained' control of the qubit which reduces the number of the pulses needed for two-qubit gates [8, 9]. Experiments demonstrate π-rotations around two orthogonal axes with rotation times $t_\pi \approx 100$ ps and 86% (transition between states) and 94% (control over qubit splitting) gate fidelity [63] which is further improved if resonantly modulated, yielding 93% and 96% gate fidelity in experiments [65]. In total, this allows for over 100 coherent exchange oscillations within the dephasing time $T_2^\star$ in Si/SiGe quantum dot devices [64]. Most recently, experiments resonantly modulating the energy gap of the hybrid qubit identical to the RX qubit (see section 2.3.4) achieve a gate fidelity of 98.4% [11]. This is performed by optimizing the point of operation, thus mitigating the effect of noise sources which is is identified as charge noise. At this point we postpone a comprehensive study of charge noise to section 4.2 and only mention that one has to decrease $\partial\omega/\partial\varepsilon$ which naively can be done by moving further into the spin-regime (green area in figure 7) of the hybrid qubit. This greatly increases the number of coherent oscillations (see figure 8) with the downside of increasing the gate time. Against theoretical predictions the best point of operation is not found by further increasing the detuning, but for certain values of ε that show a plateau for $\omega(\varepsilon)$, thus a small susceptibility ($\sim\partial\omega/\partial\varepsilon$) to charge noise. The highest fidelities were found at such a plateau [11]. Another recent demonstration of a modified version

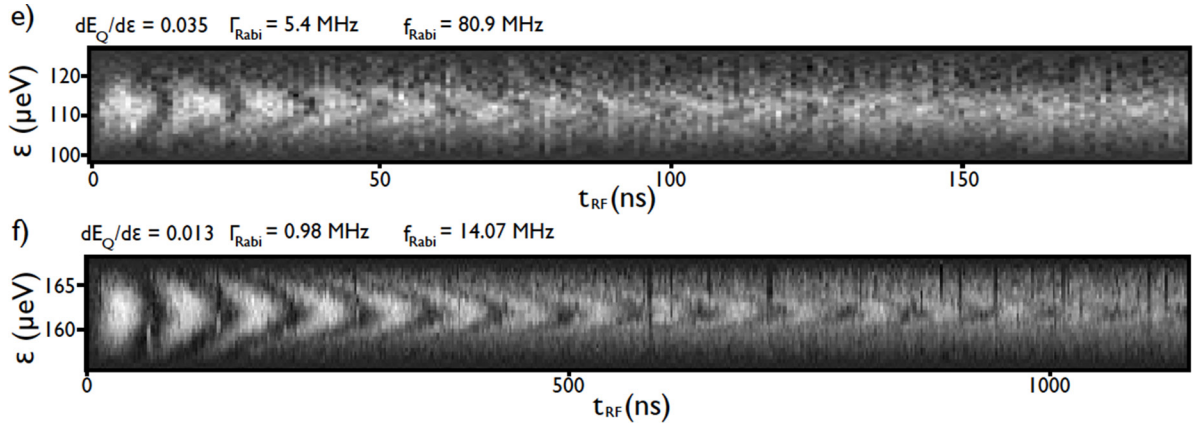

Figure 8. Rabi exchange oscillation of the probability to be in state $|1\rangle$ as a function of time r_{RF} for (e) a detuning $\varepsilon = 115$ μeV and (f) for a detuning $\varepsilon = 161$ μeV. The results show an increased number of oscillations for larger ε due to lesser susceptibility to charge noise. Figure taken from [11] with permission of the authors. Reprinted with permission from [11] Copyright 2016 by the American Physical Society.

of the hybrid qubit with 5 electrons in a GaAs double quantum which operates at the (2,3)–(1,4) charge transition yields over 10 coherent Rabi oscillations during the coherence time [10]. Note, that in GaAs dephasing is much faster than in silicon devices due to the presence of nuclear spins.

An initialization and read-out scheme requires the coupling of the doubly occupied QD to the lead with a significant difference in the tunneling rates between the qubit states. A large difference in the tunneling rates allows for a time-resolved measurement which yields information about the qubit state to be initialized or read-out. The crucial requirement, significantly different tunneling rates, are experimentally demonstrated in GaAs [226] and Si/SiGe [8, 227] devices. Numerical results predict further improvement of the coherence times measuring the current flow through a quantum point contact [228].

3. Two-qubit gates for three-spin qubits

3.1. Using short-ranged exchange

After the experimental demonstrations of arbitrary single qubit rotations [59, 69] the remaining challenge is the demonstration of universal two qubit operations in order to achieve universal quantum computation according to the DiVincenzo criteria [229]. Note that the bulk of two qubit gates are universal [230]. The set-up is the following; two three-spin qubits are coupled via the exchange interaction, i.e, spins in the set-up are coupled via a Heisenberg exchange term $H = \sum_{i,j} J_{ij} \boldsymbol{S}_i \cdot \boldsymbol{S}_j$ (see equation (2)). Thus, for the discussion it does not matter whether the electrons are physically separated, i.e. in different QDs, and/or energetically separated, i.e. in different orbitals, since this only changes the explicit expressions for the exchange couplings between the electron spins. If not otherwise mentioned a linear geometry is considered where only spins 3 and 4 are connected (shown schematically in figure 9(a)).

For two spin-$\frac{1}{2}$ qubits a simple sequence yields the two-qubit gate (see section 1.4), however, for the case of exchange coupled three-spin qubits the story is more complex. The main problem arises from the fact that the computational two-qubit space, $\mathcal{H}_{2\mathrm{qubit}} = \mathcal{H}_{+1/2} \oplus \mathcal{H}_{+1/2}$, represents only a subspace of the sector with spin quantum numbers $S = 1$ and $S_z = +1$ of the combined system. The inter-qubit exchange coupling leads to excursions outside the computational space during the pulse sequences, and thus, the possibility of leakage into the non-computational space. There are two distinct approaches to counteract the leakage which we discuss in detail; in the first approach, complex pulse sequences are applied in order to make sure that the mapping between the non-computational space and the qubit subspace at the end of the sequence vanishes [2]. In the second approach a (large) energy difference between the computational space and the non-computational space in combination with fast gates (approximately) prevents leakage into the non-computational subspace [15].

3.1.1. Exact gate sequences. There are many different pulse sequences for implementing an exact entangling gate between two three-spin qubits. In order to keep the expressions simple, we consider the time steps τ of the exchange interaction in units of a full swap gate, $\tau_{\mathrm{SWAP}} = 2\hbar/\pi J$, between connected spins in the remainder of this section. This justifies a consideration where all exchange couplings are identical, $J_{ij} = J$ since the resulting two-qubit gate $U_{ij}(\tau) = \exp[\mathrm{i} \int_0^\tau \mathrm{d}t' J_{ij}(t')\, \boldsymbol{\sigma_i} \cdot \boldsymbol{\sigma_j}/4\hbar]$ is independent of the pulse shape of $J_{ij}(\tau)$. In the original proposal, a minimal pulse sequence consisting of 19 exchange interactions between the spins was found numerically yielding a CNOT-gate up to local single qubit gates [2]. The sequence can be implemented in 13 time steps since some exchange interactions can be run in parallel. However, this sequence yields a leakage-free entangling gate only for the subspace qubit while there is still leakage in the case of the subsystem qubit. As a brief reminder, the subspace qubit is encoded in either of the two-level systems, $S = 1/2$ and $S_z = +1/2$ or $S = 1/2$ and $S_z = -1/2$, whereas the subsystem simultaneously uses both two-level systems $S = 1/2$ and $S_z = \pm 1/2$ for the encoding [2, 19]. An exact CNOT-gate sequence for the subsystem qubit consists of 22 pulses in 13 time steps [12] with all time steps being multiples of $\tau_{\mathrm{swap}}/4$, where the bare two-qubit pulse sequence consists of 18 pulses in 11 time

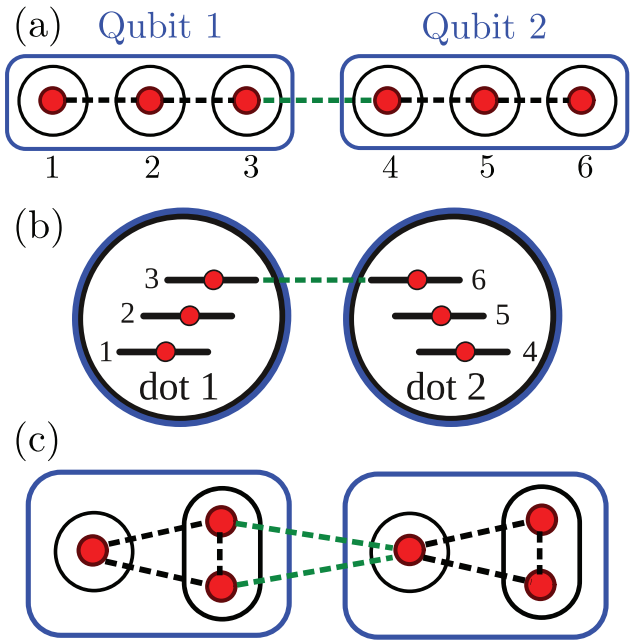

Figure 9. (a) Schematic illustration of the coupling of two three-spin qubits consisting of six spins (red dots) labelled numerically from left to right. The black circles represent the position (QD or orbital) of the spins in each qubit (blue box), the black dashed lines correspond to the intra-qubit exchange interactions, and the green dashed line to the inter-qubit exchange interaction (connecting spin 3 and spin 4). We refer to this geometry as the linear geometry. (b) Schematic illustration of the two-qubit coupling of two spin-charge qubits. The inter-dot exchange interaction (green) can be controlled by the tunnel barriers. The shortest full pulse sequence that implements CNOT excluding single qubit rotations consists of nine pulses. Figure inspired by [7]. (c) Schematic illustration of the two-qubit coupling of two hybrid qubits (qubit 1 and qubit 2). The black circles represent the quantum dots of each qubit (blue box) which each consists of three electrons (red dots), the black dashed lines correspond to the intra-qubit exchange interactions, and the green dashed lines to the inter-qubit exchange interaction. The shortest full universal pulse sequence consists of 14 exchange pulses. Figure inspired by [8].

steps [13]. Allowing for simultaneously applied exchange pulses one can find a two-qubit gate sequence in 8 time steps. However, this requires precise control of all couplings individually. It should be noted that all sequences were discovered using a numerical minimization algorithm due to the very large Hilbert space of six spins-$\frac{1}{2}$ (dimension $2^6 = 64$). A full understanding and analytical derivation of the path through the Hilbert space associated with the exact CNOT gate has subsequently been found [14, 231].

Taking into consideration other geometries which have more connections (exchange couplings) between the two three-spin qubits, shorter and faster pulse sequences are possible. The shortest sequence consisting of 12 pulses in 9 time steps was found for the unrealistic case of a fully connected geometry, while one needs at least 14 pulses with the butterfly geometry where the center spins of each three-spin qubit are connected (connection between spin 2 and spin 5 in figure 9(a)).

Nevertheless, the mutual feature that all sequences require more than ten pulses makes the exact two-qubit gate somewhat vulnerable to a noisy exchange interaction, i.e. charge noise in the tunnel parameters and detuning parameters or hyperfine interaction due to nuclear spin. Treating the effects of nuclear noise requires a noise-correction scheme consisting of permutations which decouple the static effects of the noise [12, 13]. In simple words, a single pulse is divided into several pulses such that each electron 'feels' the same nuclear fields at each given time step, thus, unavoidably increases the pulse sequences [12, 13]. The procedure is comparable to a spin echo where the effect of dephasing is reversed by a spin flip and can also be adapted for (quasi) static charge noise. However, due to the nature of charge noise which also consists of high frequency components the correction scheme is better suited for counteracting the effects of nuclear noise due to its slow dynamics. For charge noise, other techniques are usually considered, i.e. operating on a charge noise sweet spot. At this point we postpone a detailed discussion regarding the exchange interaction under the influence of charge noise to section 4.2.

Distinctions for spin-charge and hybrid qubit. Since the description of two-qubit gates has been general up to now, we want to inform the reader in this paragraph about some special distinctions regarding the SC qubit and the hybrid qubit.

The SC qubit was introduced in section 2.4 and is implemented in a single QD using several orbitals (1,2,3). In a naive understanding, one would assume that, if two such qubits are placed next to each other, all orbitals would be coupled via an external exchange interaction with a similar strength. However, in a minimal coupling approach only the highest orbitals of two neighboring spin-charge qubits are typically coupled via the next neighbor exchange interaction (shown schematic illustration in figure 9(b)) [7]. Since the occupation probability at the edge of the quantum dot increases with increasing orbital quantum number [232], electrons in two quantum dot couple first via the highest orbitals if one brings them together [7]. Careful adjustment of the gate potentials and the use of the non-linear dependence of the exchange coupling with respect to the inter-dot distance [120], can lead to a selective coupling of only the uppermost orbitals with each other. Note that the resulting two-qubit coupling is identical to that of the EO qubit (see figure 9(b)) except for the always-on intra-dot exchange interaction, thus, similar but not identical pulse sequences can be used. The shortest pulse sequence that implements CNOT excluding single qubit rotations consists of a minimum of nine pulses [7].

For the hybrid qubit one can use the same argumentation as for the SC qubit. However, since the hybrid qubit has additional single-qubit control (schematically illustrated in figure 9(b)) shorter pulse sequences are feasible consisting of only 14 exchange pulses [8, 13, 233] summing up to an overall gate time on the order of nanoseconds. One possible issue for the implementation of exchange-based two-qubit gates for the hybrid qubit is leakage to the non-computational space which is larger than for the other implementations as the spin-charge and exchange-only qubit. While the occupation of these states, i.e. clones of the qubit state $|0\rangle = |s\rangle_R|\downarrow\rangle_L$ where $|s\rangle$ is not the ground state, is suppressed for single-qubit rotations [8], this is not the case for inter-qubit exchange (two-qubit gate), thus giving rise to increased leakage.

3.1.2. Approximated gate sequences. Instead of maneuvering on complex paths through the Hilbert space in order to minimize leakage into the non-computational space, one can use short cuts, gate sequences consisting of a single exchange pulse [15, 16, 234]. However, these short cuts are only feasible if there exists a favorably large energy gap between the computational and non-computational subspaces. This energy gap is crucial since it reduces the amount of leakage during the operation depending on the size of the energy gap. It should also be noted that the amount of leakage can never reach exactly zero for a finite energy gap. Practically speaking, this energy gap is increased by a larger energy splitting between the qubit states while it is reduced by the inter-qubit exchange interaction [15], thus, making the RX qubit an ideal candidate for its two-qubit scheme due to the large and always turned-on exchange interaction. Another good candidate is the AEON qubit where the exchange interaction is always turned on or off. However, the AEON qubit naturally has a smaller qubit splitting than the RX qubit. We want to discuss two concrete methods for implementing two-qubit gates, the first consisting of a DC pulse, while in the second the exchange interaction is modulated by an RF signal. Both methods provide fast two-qubit gates with suppressed (but still finite) leakage.

Considering a Heisenberg type Hamiltonian for the interaction between the electrons in the singly occupied QDs the system is described by $H = H_A + H_B + H_{int}$ where $H_{A,B}$ are the uncoupled single qubit Hamiltonians introduced in equation (34). Focusing on the relevant subspace $S_z = 1$ which has dimension $n = 15$, there are 11 leakage states [15], however, six states with a total spin $S = 2,3$ cannot be accessed by the exchange interaction alone since it conserves the total spin [2]. However, gradients in the magnetic field and spin–orbit interaction can cause transitions into these additional leakage states. In table 1 the corresponding eigenenergies of the 11 states are displayed. In lowest order in perturbation theory, i.e. $J_c/J \ll 1$ with the inter-qubit coupling J_c and the intra-qubit coupling J, the interaction between qubit A and qubit B for a general geometry can be expressed as [15]

$$H_{int} = \delta J_0 + \delta J_z(\sigma_{z,A} + \sigma_{z,B})/2 + J_{zz}\sigma_{z,A}\sigma_{z,B} + J_\perp(\sigma_{x,A}\sigma_{x,B} + \sigma_{y,A}\sigma_{yB}), \quad (45)$$

where $\sigma_{i,Q}$ is the $i = x,y,z$ Pauli matrix acting on qubit $Q = A,B$. Each of the coefficients J_0, δJ_z, J_{zz}, and $J_\perp$ is proportional to the inter-qubit exchange interaction J_c. The parameters strongly depend on the chosen geometry, e.g. for a linear geometry (inter-qubit coupling between QD 3 of the first qubit and QD 1 of the second qubit) the parameters can be chosen as follows, $\delta J_z/J_c = 1/36$, $J_{zz}/J_c = 1/36$, and $J_\perp/J_c = -1/24$. It is very useful for the implementation of a CPHASE gate between the qubits that for large inequality between the qubit splittings $|J_{z,A} - J_{z,B}| \gg J_c$ the degeneracy between the $|01\rangle$ and $|10\rangle$ two-qubit states is lifted, thus, one finds $J_\perp = 0$ [15]. A CPHASE-gate can now be implemented in a single pulse for $\int_0^\tau dt' J_{zz}(t') = \pi/4$. For $J_\perp \neq 0$ single qubit operations are additionally needed to 'echo out' the effects of the perpendicular interaction term [15] which is always possible [235]. Realistic values for the exchange interactions using the RX qubit encoding predict gate times $\tau_{gate} = 21$ ns ($\tau_{gate} = 63$ ns) with a leakage error $L < 1\%$ ($L < 0.1\%$) [15]. Using realistic parameter setting for the AEON qubit the gates times are longer ($\tau_{gate} > 100$ ns) [16] due to the weaker exchange splitting. An improvement can be achieved by using different coupling geometries, especially the butterfly geometry (center QD of both qubits are connected) which provides the best gate times [15, 16]. Further improvement is obtained using different pulse shapes for the exchange pulse with the best having a sinusoidal shape, $J_c = J_{c,0}[1 - \cos(2\pi\tau/\tau_{gate})]$ allowing for single-pulse fidelities exceeding 0.9999 for physically reasonable parameter settings [234]. Leakage is increased by considering a realistic environment consisting of charge noise and Overhauser noise due to nuclear spins. Recent studies show that low-frequency charge noise has the strongest impact on the gate fidelity [234].

Table 1. All 15 states in the $S_z = 1$ subspace of two three-spin qubits with their respective eigenenergies, where $J_{z,A\,(B)}$ is the exchange splitting between the qubit states $|0\rangle$ and $|1\rangle$ in qubit A (qubit B). For the notation we use $|A,B\rangle = |A\rangle|B\rangle$, where the leakage states are defined as follows; $|Q_{3/2}\rangle = |S = \frac{3}{2}, S_z = +\frac{3}{2}\rangle = |\uparrow,\uparrow,\uparrow\rangle$, $|Q\rangle = |\frac{3}{2}, S_z = +\frac{1}{2}\rangle = (|\uparrow,\uparrow,\downarrow\rangle + |\uparrow,\downarrow,\uparrow\rangle + |\downarrow,\uparrow,\uparrow\rangle)/\sqrt{3}$, and $|0_-\rangle$ and $|1_-\rangle$ being the qubit states for $S_z = -1/2$ (see equation (29)). Note that all qubit states differ in energy from the leakage states. This table was adapted from [15].

Two qubit state	Energy + E_{Zeeman}
$\|Q,Q\rangle, \|Q_{3/2},Q_-\rangle, \|Q_-,Q_{3/2}\rangle$	0
$\|0,Q\rangle, \|0_-,Q_{3/2}\rangle$	$-J_{z,A}/2$
$\|Q,0\rangle, \|Q_{3/2},0_-\rangle$	$-J_{z,B}/2$
$\|0,0\rangle$	$-(J_{z,A} + J_{z,B})/2$
$\|1,Q\rangle, \|1_-,Q_{3/2}\rangle$	$-3J_{z,A}/2$
$\|Q,1\rangle, \|Q_{3/2},1_-\rangle$	$-3J_{z,B}/2$
$\|1,0\rangle$	$-(3J_{z,A} + J_{z,B})/2$
$\|0,1\rangle$	$-(J_{z,A} + 3J_{z,B})/2$
$\|1,1\rangle$	$-3(J_{z,A} + J_{z,B})/2$

The second approach uses a RF modulation of the exchange coupling $J_c(\tau) = J_{c,0}(\tau) + J_{c,\Delta}(\tau)\cos[(J_{z,A} - J_{z,B})\tau]$ between the qubits. For example, in experiments using a linear geometry this would correspond to the modulation of the energy barrier between the two qubits. Under a rotating wave approximation ($J_{c,0}, J_{c,\Delta} \ll (J_{z,A} - J_{z,B})$) the two-qubit interaction is given by [15]

$$H_{int} = \frac{J_{c,0}}{6}\sigma_{z,A}\sigma_{z,B} + \frac{J_{c,\Delta}}{24}(\sigma_{x,A}\sigma_{x,B} + \sigma_{y,A}\sigma_{yB}), \quad (46)$$

where we used the same expressions as in the paragraph above. The advantage of this approach is that both control parameters $J_{c,0}$ and $J_{c,\Delta}$ can be set individually allowing for more flexibility of controlling the two-qubit gate. The only required condition is $|J_{c,\Delta}| < J_{c,0}$ due to the positive sign for the exchange interaction [15].

3.2. Long-ranged two-qubit gates

At the time of writing of this review the best available option for error correction techniques appears to be the surface codes which require a two-dimensional geometry of qubits [236,

237]. In realistic devices, this is a challenge since each qubit must be accessed by multiple (gate) electrodes limiting the possibility to connect one qubit with more than two other qubits through exchange. This makes it more realistic to use a linear geometry. Since the exchange interaction is limited to adjacent QDs, other, long-range interactions have to be considered to overcome this technical difficulty allowing for a two-dimensional array of qubits which are spatially separated [238]. There are several proposals for the achievement of such an interaction, e.g. tunneling mediated by a superconductor [239, 240], coupling though surface acoustic waves [241–246], ferromagnets [247], superexchange mediated by an additional QD [163, 248–250], spatial adiabatic passage [233, 251, 252], photon assisted tunneling [253–255], and quantum Hall edge states [245, 256]. The most practical ideas (up to date) seem to be Coulomb-based dipole-dipole coupling [6, 9, 257–260] and cQED mediated coupling [17, 18, 114, 173, 218, 261–263] which both use the electric dipole moment of the qubit, whereas in the second approach the interaction range is elongated by the use of a cavity as a mediator [3, 17, 18, 167, 168]. For the capacitative coupling the relevant interaction is the direct dipole-dipole coupling of the three-spin qubits originating from the charge difference of the qubit states proposing a fast and feasible two-qubit pulsed gate [6, 9, 259, 260] while a more realistic analysis hints possible problems due to charge noise [259]. Three-spin qubits have (in certain parameter regimes) large electric dipole moments [6, 8] which, combined with recent advances in superconducting microwave cavities, boost the vacuum coupling strength [172], making the three-spin qubits a good candidate for the implementation of cQED. There are multiple ways to implement such two-qubit gates which we try to discuss in the following.

Qubit-cavity interaction. Originally proposed for superconducting qubits [264] due to their strong dipole coupling strength on the order of $g \approx 200$ MHz [265, 266], cQED can also be used for semiconductor spin qubits despite having a coupling strength at least one order of magnitude smaller [167, 168], i.e. $g \approx 0.1$–10 MHz [3, 6, 17, 18] for three-spin qubits, due to advances in the coherence times [79] and cavity design [115, 172]. It is crucial to achieve a coherent coupling between the qubit and the cavity, therefore, a coupling which needs to be stronger than the relaxation and dephasing mechanism in each, the cavity and the qubit, which recently was achieved for single electron charge in a semiconductor double quantum dot [113, 115, 173, 263].

For the purpose of its theoretical investigation, the cavity can be described as a resonator (see figure 10(a)) with only a single mode with frequency ω_{ph} that lies nearby the resonant frequency of the qubit splitting ω. Thus, the cavity is described without loss or decoherence effects by a quantum harmonic oscillator with this frequency $H_{\mathrm{cav}} = \hbar\omega_{\mathrm{ph}}(a^\dagger a + \frac{1}{2})$ [267], where $a^\dagger$ (a) creates (annihilates) a photon inside the cavity with the very same frequency. The corresponding energy of the cavity is $E_{\mathrm{cav}} = \hbar\omega_{\mathrm{ph}}(n_{\mathrm{ph}} + \frac{1}{2})$ which depends on the average number of photons $n_{\mathrm{ph}} = \langle a^\dagger a\rangle$. Many protocols for

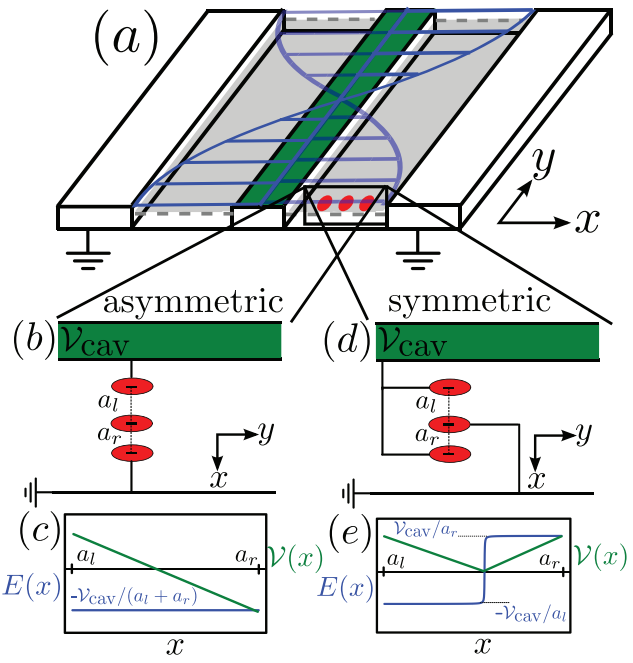

Figure 10. (a) Schematic illustration of a qubit implemented in a triple quantum dot coupled to the cavity and the architecture for a (b) asymmetric and (d) symmetric qubit-cavity coupling. The center conductor of the superconducting transmission line resonator is on the potential $\mathcal{V}_{\mathrm{cav}}$ while the outer conductors are connected to the ground to screen off surrounding fields. The corresponding potential (green) and electric field (blue) is shown for the asymmetric (c) and symmetric (e) arrangement as a function of the position x. Figure taken from [3] with permission of the authors. Reprinted with permission from [3] Copyright 2016 by the American Physical Society.

two-qubit gates [167, 168, 264] require the cavity to be in the ground state, therefore, depending on the resonance frequency to be cooled to very low temperatures, e.g. $T \ll 50$ μeV for a 10 GHz cavity, while a few protocols also work with thermally populated cavities [262, 268].

In the approach of cQED the qubit-cavity interaction is described by the minimal coupling approach which replaces the momentum with the generalized momentum $\boldsymbol{p} \to \boldsymbol{p} - e\boldsymbol{A}$ that includes the electromagnetic vector potential $\boldsymbol{A}$ and the elementary charge e [267]. In the dipole approximation near the resonance the coupling is

$$H_{\mathrm{dip}} = -e\boldsymbol{E}\cdot\boldsymbol{d} \tag{47}$$

where $\boldsymbol{E} = \boldsymbol{\mathcal{E}}(a + a^\dagger)$ denotes the electric field inside the cavity and $\boldsymbol{d}$ is the dipole operator of the qubit. Defining the qubit-cavity coupling strength as the transition amplitude between the qubit states $g \equiv -e\langle 0|\boldsymbol{\mathcal{E}}\cdot\boldsymbol{d}|1\rangle$ allows for a quantitative comparison [168]. In order to find the dipole operator $\boldsymbol{d}$ the microscopic wave functions of the three-spin qubit states are necessary which are in general rather difficult to obtain [192]. Fortunately, there are a few approximations that help to overcome this difficulty.

In a simplified picture, where the spatial extension of the QD is much smaller than the wavelength of the resonator mode, the qubit-cavity interaction is derived from the oscillation of the electrostatic gate potentials [167]. Depending on which gate electrode is connected to the cavity, thus, the

architecture of the qubit-cavity system (see figures 10(b) and (d)), ε, ε_M or both provide the coupling [17]. The corresponding dipole operator is $\boldsymbol{d} = d_x \boldsymbol{e}_x$ with $\boldsymbol{e}_x$ being the unit vector in x-direction and $d_x = \partial H(q)\nu/\partial q$, where the qubit Hamiltonian H depends on the detuning $q = \alpha\varepsilon + \beta\varepsilon_M$ with $\alpha, \beta \in \mathbb{R}$ and $\alpha^2 + \beta^2 = 1$. The phenomenological parameter ν describes the overall interaction strength and can be derived from the capacitances in the hybrid (qubit and cavity) system [167]. For $\beta = 0$ only ε is relevant (corresponds to figure 10(b)) which leads to $d_x = \hbar g \sigma_x$ with the coupling strength [18]

$$\frac{g}{g_0} = \frac{1}{2}\sqrt{\left(\frac{\partial J}{\partial \varepsilon}\right)^2 + 3\left(\frac{\partial j}{\partial \varepsilon}\right)^2} \tag{48}$$

with the exchange coupling $J = (J_l + J_r)/2$ and $j = (J_l - J_r)/2$ from equations (31) and (32) and, the vacuum coupling strength g_0 [18].

In a more realistic picture, the microscopic three-electron real-space wavefunctions of the states $|0\rangle, |1\rangle, |2\rangle, |3\rangle, |4\rangle$, and $|5\rangle$ from equations (11)–(18) are constructed from the single-electron real-space wavefunctions [120] $|\psi_i\rangle$ with $i = 1$, 2, 3 needed for the dipole matrix elements [17, 168]. Since these single-electron real-space wavefunctions depend on the experimental setup, thus the number of QDs, we show in this paragraph only the results for the exchange-only qubit implemented in a TQD. Using the formalism of orthonormalized Wannier orbitals [3, 17], the overlapping wavefunctions $|\psi_i\rangle$ are transformed into a basis of orthonormalized maximally localized [269] wavefunctions $|\phi_j\rangle$. Requirements for this transformation are a small overlap between the single-electron wavefunctions, $|\langle\psi_i|\psi_j\rangle| = |S_{ij}| \ll 1$ with $i, j = 1$, 2, 3 [17, 120, 168]. The full expression of the dipole operator in the basis $\{|0\rangle, |1\rangle, |2\rangle, |3\rangle, |4\rangle, |5\rangle\}$ can be found in [3] and depends solely on the transition dipole matrix elements $\boldsymbol{x}_{ij} = \langle\phi_i|\boldsymbol{d}|\phi_j\rangle$ of the single-electron Wannier orbitals. In the next step the geometry of the qubit-cavity device is needed, since it enters the expression through the dependence of the electric field $\boldsymbol{E}$ from the position (see figures 10(c) and (e)). An analytical expression for the asymmetric case $\boldsymbol{E} = E(a^\dagger + a)\boldsymbol{e}_x$ with $\boldsymbol{e}_x$ being the unit vector in x-direction (see figure 10(c)) inside the (1, 1, 1) charge configuration regime is [3]

$$\frac{g_A}{g_0} = -\sqrt{\frac{3}{2}}\left[\frac{J_l}{t_l}\frac{\mathrm{Re}(x_{12})}{2(a_l + a_r)} - \frac{J_r}{t_r}\frac{\mathrm{Re}(x_{23})}{2(a_l + a_r)}\right] - \frac{\sqrt{3}}{4}\left[\frac{(\varepsilon - \varepsilon_M)}{U}\frac{J_l^2}{t_l^2}\frac{x_{11}}{a_l + a_r} + \frac{(\varepsilon + \varepsilon_M)}{U}\frac{J_r^2}{t_r^2}\frac{x_{33}}{a_l + a_r}\right]. \tag{49}$$

Here, g_0 is again the vacuum coupling of the cavity, a_l (a_r) is the inter-dot distance between QD 1 and QD 2 (QD 2 and QD 3) while $\mathrm{Re}(\xi)$ denotes the real part of ξ. This result is consistent with the results in the simplified picture (see equation (48)) under the assumptions $\mathrm{Re}(x_{ij}) = 0$ for $i \neq j$, $x_{11} = -a_l$ and $x_{33} = a_r$ which corresponds to a vanishing overlap between the single-electron wavefunctions. Obviously, this expression consists of two parts where each corresponds to the qubit-cavity coupling of a DQD [168], thus, the combined effect of the coupling of two DQDs. For a symmetric architecture where the cavity is connected to the gate electrode of QD 2 (see figure 10(d)) the electric field is position dependent (see figure 10(e)), $\boldsymbol{E} = \frac{1}{\pi}\left\{\tan^{-1}\left[\frac{\boldsymbol{d}\cdot\boldsymbol{e}_x}{T(a_l + a_r)}\right] + \frac{\pi(a_l - a_r)}{2(a_l + a_r)}\right\}(a^\dagger + a)\boldsymbol{e}_x$ where T is a dimensionless screening parameter. Practically, T describes sharpness of the bend in the electric potential (see figure 10) and needs either to be simulated or measured. Approximate analytic expressions exist for large screening $T \gg 1$

$$\frac{g_S}{g_0} = \frac{a_l - a_r}{2(a_l + a_r)^2}\langle g|(\boldsymbol{d}\cdot\boldsymbol{e}_x)|e\rangle + \frac{1}{\pi T(a_l + a_r)^2}\langle g|(\boldsymbol{d}\cdot\boldsymbol{e}_x)^2|e\rangle, \tag{50}$$

where the full expression of $\langle g|(\boldsymbol{d}\cdot\boldsymbol{e}_x)^2|e\rangle$ is found in [3]. A comparison of the asymmetric and the symmetric coupling strength is seen in the top row of figure 11 which shows the minimal vacuum coupling needed to reach strong coupling.

Instead of focusing solely on the transition dipole matrix elements typically used for (transversal) two-qubit entanglement protocols [167, 168] one can also calculate the longitudinal [109, 111] dipole matrix element $g_l = (\langle 0|\boldsymbol{\mathcal{E}}\cdot\boldsymbol{d}|0\rangle - \langle 1|\boldsymbol{\mathcal{E}}\cdot\boldsymbol{d}|1\rangle)/2$ used for longitudinal entanglement protocols [116, 217, 270, 271]. The crucial difference is that the first induces a transition between the qubit states $|0\rangle \leftrightarrow |1\rangle$ through the absorption/emission of a cavity photon, while the longitudinal dipole matrix element only changes the phase of the qubit state assisted by the cavity photon. Its strength can be estimated by the same procedure as for the transverse coupling.

Under realistic settings, both couplings, the transversal and the longitudinal, are permanently present. However, depending on the exact position in the $(\varepsilon, \varepsilon_M)$-space, their strength changes significantly, therefore, effectively turning off one kind of coupling [116, 218]. This resembles a sweet spot (where first order effects vanish) for this type of coupling (see section 4.2). Combining all the above elements, the qubit-cavity Hamiltonian in its eigenbasis, up to a constant shift in energy, is

$$H = \frac{\hbar}{2}\omega\sigma_z + \hbar\omega_{\mathrm{ph}}a^\dagger a + g_l(a^\dagger + a)\sigma_z + g(a^\dagger\sigma_- + a\sigma_+) \tag{51}$$

with the ladder operators $\sigma_\pm = (\sigma_x \pm \mathrm{i}\sigma_y)/2$. This expression corresponds to the extended Jaynes–Cummings Hamiltonian [272–274] and is derived using a rotating wave approximation, $g \ll \omega_{\mathrm{ph}}$, whereby the counter-rotating terms $a^\dagger\sigma_+$ and $a\sigma_-$ are excluded since they oscillate with twice the cavity frequency and therefore average out [275].

Concepts for two-qubit gates. In the conventional scheme for a long distant coupling the qubits are entangled using the photons as a carrier of information [166]. This concept is generally applicable for all two-level systems and only needs a sufficiently strong qubit-cavity coupling outmatching the loss and dephasing effects [168, 264, 276]. The starting situation is as follows; two three-spin qubits in the same

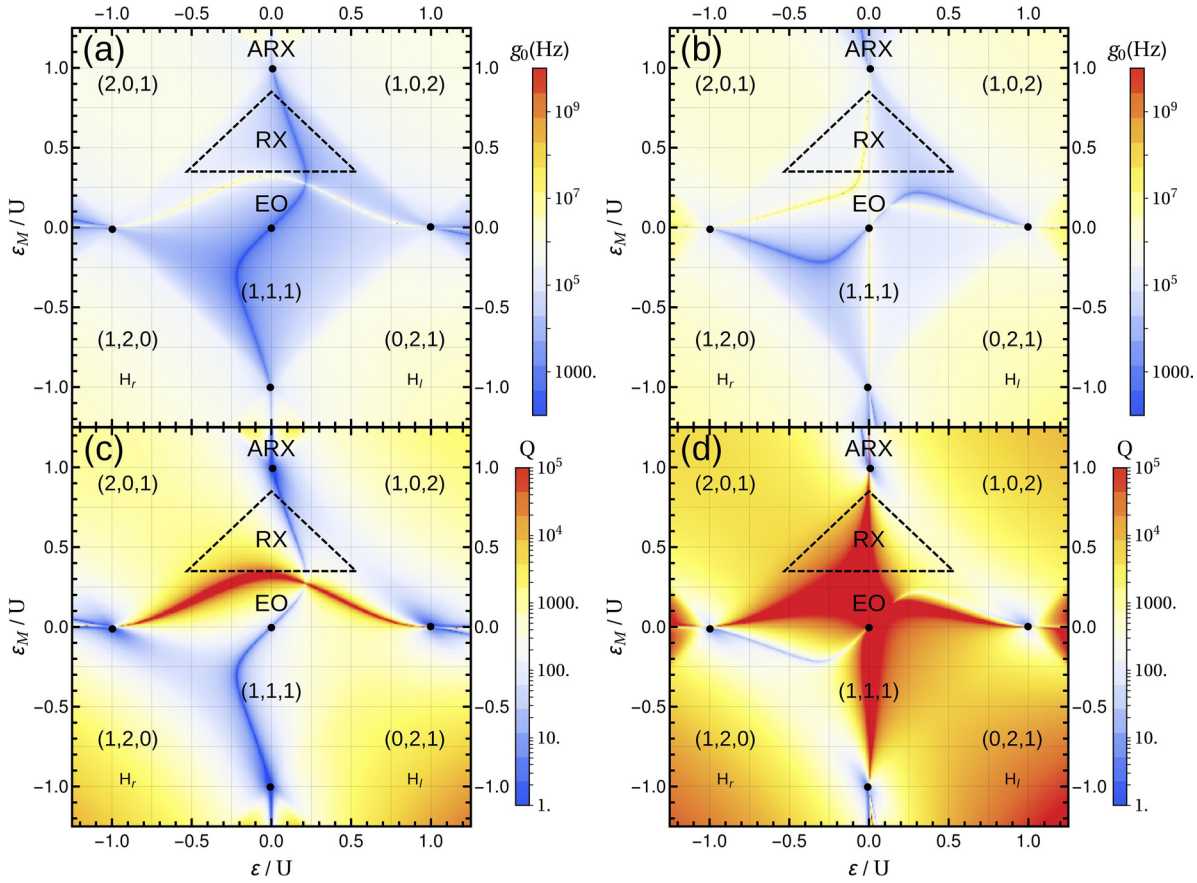

Figure 11. (Top row) The minimal vacuum coupling g_0 needed to reach strong coupling between the qubit and the cavity under the assumption that qubit dephasing is the dominant loss mechanism. (Bottom row) Minimal Q-factor of the cavity needed for successful entanglement between two qubits in the same cavity using dispersive transversal coupling. Panels (a) and (c) show the results for the asymmetric architecture and with noise only in the asymmetric detuning parameter ε, while (b) and (d) show the results for the symmetric architecture and noise only in the symmetric detuning parameter ε_M. The parameters are chosen as follows; $\omega_{\rm ph} = 4.7$ GHz, $g_0 = 2\pi \times 10$ MHz, $t_l = 0.022\,U$, $t_r = 0.015\,U$, and the noise strength $A_q = (10^{-3}\,U)^2$ where $q = \varepsilon$ in (a) and $q = \varepsilon_M$ in (b). The datasets for T_φ are obtained from [3]. For the scale of T_φ and g an explicit value of $U = 1$ meV is used. Reprinted with permission from [3] Copyright 2016 by the American Physical Society.

cavity that both are transversally coupled to the same cavity. Operating in the dispersive regime $g \ll |\Omega_i| \equiv |\omega_{\rm ph} - \omega_{1,2}|$, where $\hbar\omega_i$ is the qubit energy splitting of qubit $i = 1,2$, the cavity mode can be eliminated by a Schrieffer–Wolff transformation [168, 264, 276] yielding the effective Hamiltonian [17, 18]

$$H = \sum_{i=1,2} \frac{1}{2}(\hbar\omega_i + \epsilon_i)\sigma_{z,i} + g_{\rm eff}(\tau)(\sigma_{+,1}\sigma_{-,2} + \sigma_{-,1}\sigma_{+,2}). \quad (52)$$

Here, the ladder operators $\sigma_{\pm,i}$ act on qubit i, the coupling strength is given by $g_{\rm eff} = g_1 g_2(\Omega_1 + \Omega_2)/\Omega_1\,\Omega_2$ with the detuning Ω_i of qubit i, and ϵ_i denotes the Stark shift of qubit i. After the time $\tau_g = \hbar\pi/2g_{\rm eff}$ the two-qubit interaction yields the universal iSWAP-gate [17, 168, 277]. A sequence of two iSWAP-gates and two single-qubit rotations form a CNOT-gate [278]. In an earlier approach, a CNOT-gate gate is generated by the same Hamiltonian by using the two-qubit $\pi/4$-gate instead [166]. Figures 11(c) and (d) show qualitatively the required quality factor $\omega_{\rm ph}/\Omega_{1,2}$ for a successful entanglement considering dephasing due to charge noise through the respective detuning parameter, i.e. ε for an asymmetric architecture and ε_M for the symmetric architecture. Using realistic parameter settings, the iSWAP-gate can be performed in $\tau_g = 540$ ns with a fidelity of 99% while for faster gates the fidelity decreases [18].

Instead of operating in the dispersive regime, a faster alternative scheme uses resonant driving [18]. This scheme, based on the Cirac–Zoller gate for trapped ions [40, 279], uses sideband transitions [276, 280, 281] that are generated when an external driving field ν is included in the qubit-cavity system. For resonant driving between the driving field and the qubit transition, $\nu = \omega$, the interaction Hamiltonian in a rotating frame is [18]

$$H = \Delta_0 a^\dagger a + g(e^{i\phi} a\sigma_+ + e^{-i\phi} a^\dagger \sigma_-) + \Omega\,\sigma_y, \quad (53)$$

where ϕ is the phase and ϵ the amplitude of the driving field, Δ_0 is the detuning between the driving field and the cavity, and $\Omega = g\epsilon/\Delta_0$ is the Rabi frequency of the qubit. Switching into a second rotating frame of the Rabi frequency and carefully adjusting the detuning $\Delta_0 = \pm 2\,\Omega$ yields 'red' and 'blue' sideband transition Hamiltonians [18]

$$H_\pm = \frac{g}{2}(e^{\mp i\phi} a^\dagger \sigma_\mp + e^{\pm i\phi} a\sigma_\pm). \quad (54)$$

An entangling controlled-Z gate is constructed using pulses of 'red' and 'blue' sideband transition gates $S_{\pm}(\phi,\tau) \equiv \exp(-\mathrm{i}H_{\pm}(g,\phi)\tau/\hbar)$ combined with single-qubit rotations. One of such a pulse sequence consists of seven pulses providing a controlled-Z gate time $\tau_g = 270$ ns with a fidelity of 99.6% for realistic parameter settings [18].

The concept of cQED with longitudinal coupling was originally developed to read out the qubit states via a microwave cavity [109, 111, 114], however, can also be used to entangle multiple distant qubits [114, 116, 217, 270, 271]. This concept is generally applicable for two-level systems, does not rely on perturbative arguments, and solely bases on the parametric modulation of the longitudinal qubit-cavity coupling, therefore, does not produce any residual terms in the Hamiltonian [217]. The starting situation is as follows; two three-spin qubits (two-level systems) are both longitudinally coupled to the same cavity (see equation (51)) while the transversal coupling $g = 0$. The longitudinal coupling leads to a small displacement of the oscillator field which can be significantly increased by resonant driving at the cavity frequency. Since the resonant driving leads also to a rapid dephasing, the modulation drive ω_m is to be chosen off-resonant that finally gives in the polaron frame rise to [217]

$$H = \sum_{i=1,2} \frac{\hbar}{2}\omega_i \sigma_{z,i} + \omega_{\mathrm{ph}} a^{\dagger}a + g_{\mathrm{eff}}(\tau)\sigma_{z,1}\sigma_{z,2}, \qquad (55)$$

where $\sigma_{z,i}$ acts on qubit i whose states are split by $\hbar\omega_i$. The two-qubit interaction $\sigma_{z,1}\sigma_{z,2}$ yields, after time $\tau_g = \theta/4|g_{\mathrm{eff}}|$, the entangling controlled-phase gate $U = \mathrm{diag}\,[1, 1, 1, \mathrm{e}^{\mathrm{i}\theta}]$ sufficient for universal quantum computing [217]. An approximate expression for the coupling strength [217] is $g_{\mathrm{eff}} = -g_{l,1}g_{l,2}\omega_{\mathrm{ph}}/[(\omega_{\mathrm{ph}} - \omega_m)(\omega_{\mathrm{ph}} + \omega_m)]$. While resembling the transversal coupling [276], the key difference is that for longitudinal coupling the results are exact and not only valid in a limited regime. Furthermore, under certain parameter settings, the gate starts and ends in the vacuum state of the cavity, therefore, the gate can be performed non-adiabatically which yields, with realistic but optimistic parameter settings, $\tau_g = 37$ ns with a fidelity of 99.99%. Note, that there is no trade-off between gate time and fidelity for this scheme, thus, allowing for fast gates with arbitrarily small errors [217]. Increased fidelity is achieved if squeezed photon states instead of coherent states are used [217]. More specific investigations regarding three-spin qubits allow the operation of such a gate on such time-scales while operated on a charge noise sweet spot [116]. However, all of the above requires a pure longitudinal coupling with no residual transversal coupling.

4. Decoherence effects in three-spin qubits

The main sources of decoherence in three-spin qubits are magnetic noise due to nuclear spins, charge noise originating from random fluctuations in the host material or transmitted via the electric gates [5] and spin–orbit interaction. Spin–orbit interactions play a less important role in this review due to the choice of host material, typically GaAs and silicon, and design of the device, i.e. lateral quantum dots in a 2DEG [78, 79] versus QDs in wires or nanotubes which usually have stronger spin–orbit interaction [86, 129, 282].

4.1. Magnetic noise

Since both qubit states of the three-spin qubits have identical spin quantum numbers S and S_z such three-spin qubits possess a natural protection against global magnetic fields [237]. Depending on the qubit implementation this degree of protection against global magnetic field fluctuations varies. The DFS qubit is completely immune against general collective noise which includes all noise that couples identically to each spin in the system [1, 2, 19, 237, 283–285]. The DFS Hamiltonian of a system coupled to a noise bath can then be expressed as $H = H_{\mathrm{system}} + H_{\mathrm{bath}} + H_{\mathrm{int}}$ and the interaction is $H_{\mathrm{int}} = \sum_{\alpha} S_{\alpha} \otimes B_{\alpha}$ where S solely acts on the system and B solely acts on the bath. The DFS qubit states both lie in the same subspace of such a S_{α}, thus, both affected identically by the noise [237]. However, only global Overhauser (effective nuclear) fields [145, 286–288], which would require a perfect polarization of the nuclear spins, are considered by general collective noise while static and fluctuating magnetic field gradients between the QDs are not considered, therefore, still inducing leakage [23, 70] and dephasing [5, 21]. The general theory of DFS is already covered in a related review [237] and we focus in this review on the effects due to Overhauser field gradients.

4.1.1. Decoherence due to magnetic noise. The main component of magnetic noise is induced by nuclear spins surrounding the nanostructures and coupling to the trapped electron spins in the QDs. These nuclear spins are present in almost all host materials with only a few having a nuclear spin free isotope, i.e. carbon (≈99%), silicon (≈95%), and germanium (≈91%), and unless one uses one of these materials, the nuclear spins interact with the trapped electrons through the hyperfine interaction [287, 288]. Due to their (almost) omnipresent nature the nuclear spins themselves and their effects on QDs are studied and reviewed very carefully in literature, e.g. by Coish and Baugh (see [145]), thus, we dispense with a repetition of the basics and focus on their effect on three-spin qubits.

Considering only the contact hyperfine interaction of the ground-state orbital of the QD, which requires low temperature and large orbital level spacing [145, 289], the interaction between the three-spin qubit and a bath of nuclear spins is effectively described by [23] $H_{\mathrm{HI}} = \sum_{i=1}^{3} \boldsymbol{S}_i \cdot \boldsymbol{B}_i$ with $\boldsymbol{B}_i = \sum_{k\in i} A_{k,i}\boldsymbol{I}_k$. Here, $A_{k,i}$ is the hyperfine interaction constant of a nucleus with spin $\boldsymbol{I}_k$ interacting with the electron spin in QD i. In typical experiments the nuclear spins are randomly oriented $\langle \boldsymbol{B}_i \rangle = 0$ with a finite standard deviation $\sqrt{\langle \boldsymbol{B}_i^2 \rangle} \approx \mathcal{A}_i$ where $\mathcal{A}_i$ is the average hyperfine energy [23] coupled to electron spin i. These Overhauser fields $\boldsymbol{B}_i$ can be correlated due to a finite overlap between the spin wavefunctions of the electron i since a nucleus in an overlapping region affects both electron spin. In realizations using TQD devices these correlations can be small due to their small overlap. Depending on

the material these coupling constants $\mathcal{A}_i$ can be rather strong, e.g. $\mathcal{A}_i \approx 85\ \mu$eV (for a full list see [145]) for GaAs giving rise to effective Overhauser fields $|\boldsymbol{B}_j| \approx 5$ T for the unrealistic case of fully polarized nuclear spins. For unpolarized nuclear spins, however, the Overhauser fields scale with $\propto 1/\sqrt{N}$ leading to typical values $|\boldsymbol{B}_j| \approx 5$ mT for $N = 10^6$ nuclear spins [145]. These Overhauser fields have two main effects on the three-spin qubit.

Differences in the Overhauser fields cause leakage into the non-computational space due to the spin non-preserving nature of H_{HI}. Therefore, without an external magnetic field the Overhauser fields couple almost all spin states giving rise to leakage into nearly every state. Reverting the leakage requires complicated sequences of pulsed magnetic fields, thus, losing the benefit of the three-spin encoding [23]. However, subject to a large magnetic field, the EO subspace qubit, $S = 1/2$ and $S_z = +1/2$ leaks only into a single state, the $S = 3/2$ and $S_z = 1/2$ state

$$|L\rangle = \frac{1}{\sqrt{3}}(|\uparrow\uparrow\downarrow\rangle + |\uparrow\downarrow\uparrow\rangle + |\downarrow\uparrow\uparrow\rangle), \tag{56}$$

giving rise to an effective three-level system. It is preferable to work in a regime where both Zeeman energy E_z and exchange splitting J is significantly larger than the Overhauser fields, $J, E_z \gg \mathcal{A}_i$, since their leakage is suppressed $\propto \mathcal{A}_i/J$. Outside this regime, the leakage dynamics occurs in timescales of nanoseconds [23].

Nuclear field gradients between the QDs make the qubit vulnerable to inhomogeneous broadening which cause dephasing of the qubit states due to the acquisition of random local phases. Setting up a Ramsey free induction type measurement consisting of two $\pi/2$-pulses separated by the time τ can quantify dephasing. Considering Gaussian distributed Overhauser fields which is valid under typical experimental conditions [78, 145] the resulting inhomogeneous broadening dephasing time is given by [23, 145]

$$T_2^\star \propto \left(\sum_{i=1}^{3} \nu_i^2 \mathcal{A}_i^2\right)^{-1/2}. \tag{57}$$

Here, $\mathcal{A}_i$ are the standard deviations of the Overhauser fields in QD j while their impact is given by the weighing factors $\nu_1 = \nu_3 = 1$ and $\nu_2 = 2$. Therefore, the dephasing times of three-spin qubits are roughly on the same timescales as for spin-$\frac{1}{2}$ qubits ($T_2^\star \approx 10$ ns) assuming uncorrelated Overhauser fields in each dot [23].

4.1.2. Suppressing magnetic noise. Since nuclear noise has typically a very slow dynamics [290] dynamical decoupling (DD) [145, 205, 291–295] offers an efficient way to counteract the effects of noise. In simple words, DD decouples the noise from the system, e.g. through gate sequences which swap the electrons in such a way that each electron is exposed to the same noise, thus, 'globalizing' the random phase. Under the assumption of static noise, a simple example is the permutation sequence which cyclicly swaps the electrons after each time interval τ. In this review, we focus on recent advances in DD which only use the exchange interaction for the decoupling sequence in agreement with the concept of the EO qubit; for the general case we refer to [237].

The starting situation is the following; a single three-spin qubit implemented in a linear TQD where the electron in each QD is coupled to a large number of nuclear spins. The three-spin qubit system in the (1, 1, 1) charge configuration is described by the Heisenberg exchange Hamiltonian plus a Zeeman term including the fluctuating Overhauser fields [26]

$$H = \frac{J_{12}}{4}\boldsymbol{\sigma_1}\cdot\boldsymbol{\sigma_2} + \frac{J_{23}}{4}\boldsymbol{\sigma_2}\cdot\boldsymbol{\sigma_3} + \sum_{n=1,2,3}\boldsymbol{B}_n\cdot\boldsymbol{\sigma}_n. \tag{58}$$

Assuming a strong Zeeman splitting the dynamics of the qubit is described by the qubit states and single relevant leakage state $|L\rangle$ (see equation (56)).

Introduced by West and Fong [25], the DD sequence consists only of operations SWAP_{ij} that interchange the spin of QD i and QD j and which are realized by the exchange interaction [123]. During the SWAP operation leakage is suppressed by exchange [23], thus, dephasing is only possible in the remaining QD during the short time of an operation since exchange is completely turned on in-between the pulses [25]. Only sequences are considered which consists of the permutation $P = \mathrm{SWAP}_{23}\mathrm{SWAP}_{12}$ and its inverse $P^{-1} = \mathrm{SWAP}_{12}\mathrm{SWAP}_{23}$. Under the assumption of Gaussian distributed noise the variance of the gathered phase differences, which cause the dephasing, can be expressed in terms of switching functions $f_j(\tau)$ with $j = 1, 2, 3$ which are defined according to the position of the spin states regarding their initial position and their rescaled Fourier transforms $\gamma_j \equiv \frac{\omega}{i}\int_0^T \mathrm{d}t\mathrm{e}^{\mathrm{i}\omega t} f_j(\tau)$ [25, 26]. The resulting expression for the variance of the phase differences is

$$\langle\Delta\Phi(T)^2\rangle = \frac{1}{\pi}\int_0^\infty \mathrm{d}\omega \sum_{j=1}^{3}|\gamma_j(\omega T)|^2\frac{S(\omega)}{\omega^2}, \tag{59}$$

where $S(\omega)$ is the power density noise spectrum of the noise which for simplicity is assumed to be identical in each QD whereas the noise in each dot is uncorrelated. The cross-correlation of the noise depends on the system and can be measured, e.g. using spatial separated QDs [296]. For a simple permutation sequence and the West and Fong sequence of length n the switching functions take the values $f_i = -1, 0, 1$ (for the exact definitions see [25, 26]) at the times $T\ \delta_j$ where δ_j with $j = 1, ..., n$ are the waiting times.

There are many concepts for optimizing the waiting times δ_j the most popular being the CPMG sequence [297, 298] which uses equidistant time intervals $\Delta\delta_j = 1/n$. However, CPMG is not optimized for the three-spin case, thus, does not lead to $\gamma_i = 0$ in lowest order. Until now the best concepts are Uhrig dynamical decoupling (UDD) [299–301] and optimized noise filtration dynamical decoupling (OFDD) [302] depending on the given noise. UDD requires that the Fourier transforms vanish up to an order m, thus, $\frac{\partial^k\gamma_i(q)}{\partial q^k}|_{q=0} = 0$ for $k = 0, ..., m$ and $i = 1, 2, 3$. In the single spin case $n = m$ pulses are required [299] with the analytical expressions for the waiting times $\delta_j = [1 - \cos(\pi j/(n+1))]/2$. For the three-spin case

$n = 2m$ pulses are required [25] while the expression for the waiting times are obtained from the solution of the $2m$ polynomial functions up to order m. OFDD directly minimizes the integral $\int_0^1 \mathrm{d}\omega \sum_{j=1}^{3} |\gamma_j(\omega T)|^2$ finding a suitable set for the waiting times δ_j. The integrals can be treated analytically, however, the values have to be determined using numerical optimization, e.g. one can use the values for CPMG and UDD as starting values. A comparison of both strategies is displayed in figure 12 which shows the better results of OFDD for both considered types of noise.

4.2. Charge noise

Charge noise or electrical noise, produced by fluctuations of charges or electric fields, is an omnipresent phenomenon if any form of electric control is used in experimental setups, directly, e.g. electric potentials to attract/deplete electrons or indirectly, e.g. background charge fluctuations. Thus, this also includes each device based on semiconductors or metals since electrons, the carriers of the charge, move around freely which unavoidably results in fluctuations due to the discreteness of the electric charge. These charge fluctuations can be correlated in time or space depending on the source of the noise. In semiconductors, the background noise is typically dominated by low-frequency noise or colored noise which has a spectral density $S(\omega) = A\omega^{-\gamma}$, where γ is the noise exponent [177, 178]. Noise which is induced into the qubit system through the gate electrodes necessary for confining and controlling the electrons is typically Nyquist–Johnson noise [303–306] due to the finite temperature and shot-noise [307] due to quantization (graininess) of electric charge. Like magnetic noise, charge noise also depends on the system [179, 296, 308], however, to a smaller degree than for magnetic noise from nuclear spins, e.g. charge noise can be enhanced in the presence of piezoelectric phonons and their coupling strength. Therefore, charge noise cannot be changed significantly if the host material is replaced, since freely-moving electrons exist in every semiconductor and every device is connected to wires.

In this section, we investigate the effect of charge noise on three-spin qubits and look for approaches to avoid noise in the first order and consecutively, if this is not possible, to avoid the effects of such noise. The first approach is usually treated by working on 'sweet spots', points in parameter space which are least susceptible to noise, while the latter is usually taken by using dynamical decoupling techniques [295, 308, 309]. Since dynamical decoupling of charge noise is already presented in the previous section and in a related review [184], we mainly study the techniques for avoiding the noise in this review.

4.2.1. Decoherence due to charge noise. Electric noise affects the charge degrees of freedom in a quantum system, thus, allows for coupling through every electrically controlled parameter in the system. The dominant links which couple the charge noise to the TQD qubit are the detuning parameters, ε (detuning between outer QDs) and ε_M (detuning between center QD and mean of outer QDs) from equation (25), linked to the gate voltages

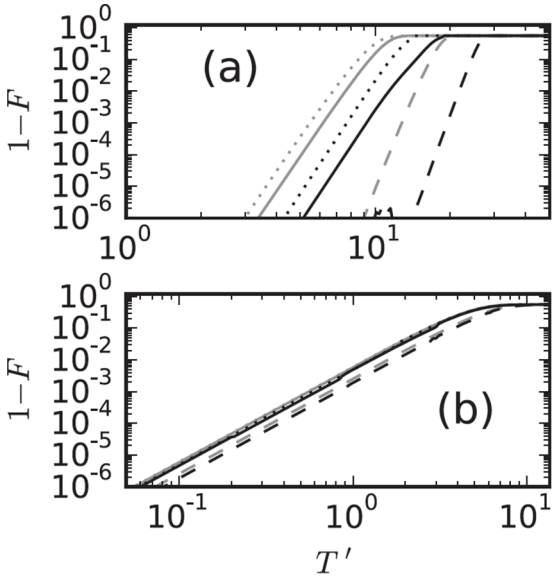

Figure 12. Comparison of the infidelity $1 - F$ as a function of the dimensionless storage time $T' = T\omega_1$ for both noise decoupling strategies, Uhrig dynamical decoupling (gray) and optimized noise filtration dynamical decoupling (black), (a) assuming ohmic noise with $S(\omega) = \omega\theta(\omega - \omega_1)/\omega_1$ and (b) Lorentzian noise $S(\omega) = 1/(1 + (\omega/\omega_1)^2)$ noise. Here, ω_1 is a sharp cut-off frequency for ohmic noise while ω_1 is the line-width for the Lorentzian noise. The dashed lines correspond to the single spin case, the solid lines correspond to the simple permutation cycle, and the dotted lines correspond to the West and Fong sequence. Reprinted with permission from [26] Copyright 2016 by the American Physical Society.

underneath each QD [3, 6, 16, 20, 24, 310] (see figure 13). This is because these control parameters typically induce the qubit gates, thus, they have to be addressed fast and precisely over a large range which limits the amount of noise filtering [59, 67, 69]. Furthermore, the tunneling parameters, t_l and t_r, also provide a significant noise contribution if the qubit is operated symmetrically by controlling the tunnel barriers between the qubits [96, 183] (see figure 13). Additional parameters worth being considered are the charging and confinement energies [200] but these play a less important role since they are static, allowing for low-pass filtering. Formally, the noisy control parameters are described by considering noisy parameters $q(\delta q) = f(\delta q)$, where f is some function which describes how the noisy parameter q is affected by the corresponding fluctuations δq. Typically, one assumes that the strength of charge noise is unaffected by the strength of the noisy parameter, thus, $q(\delta q) = q + \delta q$ [3, 6, 16, 20, 24, 310]. While by definition the average of these fluctuations vanishes, $\langle \delta q \rangle = 0$, under realistic conditions there are no measurements yet in TQD devices of the standard deviations and higher cumulants. For the detuning parameters, ε and ε_M, measurements in single QDs and DQDs indicate values of $\sqrt{S(\omega)}\big|_{\omega=1\,\mathrm{Hz}} \simeq 5\ \mu\mathrm{eV}\ \sqrt{\mathrm{Hz}}^{-1}$ in a GaAs device [175, 311–317] and $\sqrt{S(\omega)}\big|_{\omega=1\,\mathrm{Hz}} \simeq 1\ \mu\mathrm{eV}\ \sqrt{\mathrm{Hz}}^{-1}$ in SiO and Si/SiGe devices [318, 319]. An effective measurement of detuning charge noise in an isotopically purified Si/SiGe TQD indicates a higher value, $\sqrt{S(\omega)_\varepsilon}\big|_{\omega=1\,\mathrm{Hz}} \simeq 15\ \mu\mathrm{eV}/\sqrt{\mathrm{Hz}}^{-1}$ for $1/f$-noise

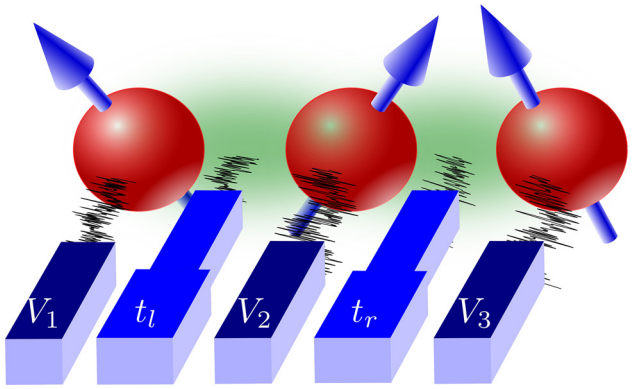

Figure 13. Schematic illustration of a three-spin qubit coupled to charge noise. The environment mainly affects the electron spins directly through the gate voltages V_i with $i \in \{1, 2, 3\}$ of each quantum dot (QD) or the exchange coupling (green cloud) between the electron spins through the gate-controlled tunnel hopping (t_l and t_r). Reprinted with permission from [3] Copyright 2016 by the American Physical Society.

[69]. While these values are likely to be accurate for ε, the noise coupling for the symmetric detuning ε_M are claimed to be ten times smaller [310]. The fluctuations of the remaining parameters such as the tunnel couplings is still unknown, but the tools to measure these are already present [296, 309, 320]. These charge fluctuations affect the qubit states but, unlike magnetic noise, do not cause any leakage out of the qubit space due to the spin conserving nature of charge noise. Leakage into other charge states with the same spin numbers such as (1,0,2) is still possible but ideally suppressed by detuning.

Since these longitudinal fluctuations are random the qubit states acquire local phases which are by definition unknown resulting in a dephasing of the qubit. A simple measurement to track these effects is provided by a Ramsey free decay sequence consisting of two $\pi/2$ pulses separated by the waiting time τ [321]. Starting in the state $|0\rangle$, the first $\pi/2$-pulse produces a superposition of the qubit states, $|+\rangle = (|0\rangle + |1\rangle)/\sqrt{2}$. After the second $\pi/2$-pulse the return probability into the $|0\rangle$ state is given by $P(\tau) = \frac{1}{2}(1 + \mathrm{Re}[f(\tau)])$ with

$$f(\tau) = \langle e^{i\phi(\tau)} \rangle = e^{-\langle \phi(\tau) \rangle_C^2/2} \tag{60}$$

where $\phi(\tau)$ is the average of the acquired phase difference between the qubit states and $\langle \phi(\tau) \rangle_C^2$ its second cumulant. For the second equality Gaussian distributed charge noise is assumed [3, 20]. The decay exponent itself strongly depends on the exact noise spectral density $S(\omega)$. Considering $1/f$-noise one finds $\langle \phi(\tau) \rangle_C^2 = \tau^2/T_\varphi^2$ with the pure dephasing time T_φ.

The transversal effect of charge noise causes random transitions between the qubit states. However, since the time-scales of the transitions are rather long (milliseconds) the qubit-flip errors can often be neglected.

4.2.2. Sweet spots and optimal working points. The starting situation is: a single three-spin qubit implemented in a linear TQD affected by charge noise through various noisy parameters q. In general, the noisy Hamiltonian is $H = H_0 + H_{\mathrm{noise}}$ where $H_0 = \hbar\omega_z/2$ is the unperturbed qubit Hamiltonian in its eigenbasis and

$$H_{\mathrm{noise}} = \hbar\,[\delta\omega_z\sigma_z + \delta\omega_x\sigma_x + \delta\omega_y\sigma_y] \tag{61}$$

is in the same basis and directly follows from perturbation theory with the single requirement that the fluctuations are small compared to the energy gap. The perturbation terms, one longitudinal and two transversal, are given by

$$\begin{aligned}\delta\omega_z &= \frac{1}{2}(\langle g|H_{1,q}|g\rangle - \langle e|H_{1,q}|e\rangle),\\ &\approx \sum_q \left(\omega_q \delta q + \frac{\omega_{q,q}}{2}\delta q^2\right) + \frac{1}{2}\sum_{p\neq q}\omega_{p,q}\delta p\delta q,\end{aligned} \tag{62}$$

$$\delta\omega_x = \frac{1}{2}(\langle g|H_{1,q}|e\rangle + \langle e|H_{1,q}|g\rangle), \tag{63}$$

$$\delta\omega_y = \frac{1}{2\mathrm{i}}(\langle g|H_{1,q}|e\rangle - \langle e|H_{1,q}|g\rangle), \tag{64}$$

where $H_{1,q} = \frac{\partial}{\partial q}H\,\delta q$, $\omega_q \equiv \frac{\partial\omega}{\partial q}$, and $\omega_{p,q} \equiv \frac{\partial^2\omega}{\partial p\partial q}$. For the approximation in the second term the perturbation is expanded up to second order in the fluctuations δq. Therefore, the most devastating effect is contributed by the longitudinal charge noise $\delta\omega_z$ which becomes clear when expanding the eigenenergy gap

$$\begin{aligned}\omega &= \sqrt{(\omega_0 + \delta\omega_z)^2 + \delta\omega_x^2 + \delta\omega_y^2}\\ &\simeq \omega_0 + \delta\omega_z + \frac{\delta\omega_x^2}{2\omega_0} + \frac{\delta\omega_y^2}{2\omega_0} + O(\delta\omega^3),\end{aligned} \tag{65}$$

while the transversal charge noise, $\delta\omega_x$ and $\delta\omega_y$, contributes only second order and becomes smaller for large ω [3, 20]. Using equation (19) and low-frequency noise $S(\omega) = A_q/\omega$, where $A_q = \sigma_q^2$ is the squared standard deviation of the noise, the Ramsey free decay pure dephasing time is [3]

$$\begin{aligned}T_\varphi = \hbar\Bigg[&\sum_q \frac{\omega_q^2}{2}A_p \log r + \frac{\omega_{q,q}^2}{4}A_q^2 \log^2 r\\ &+\frac{1}{2}\sum_{p\neq q}\frac{\omega_{p,q}^2}{2}A_pA_q \log^2 r + \frac{1}{8}\omega_{p,p}\omega_{q,q}A_p\,A_q\Bigg]^{-\frac{1}{2}}\end{aligned} \tag{66}$$

with the ratio $r = \omega_U/\omega_L$ of the upper cut-off frequency ω_U and the lower cut-off frequency ω_L.

With this in mind, a formal definition for 'sweet spots' [3, 5, 6, 16, 20, 24, 234, 310] of order $n = 1, 2, 3, \ldots$ is

$$\sum_q \omega_q \delta q = 0, \tag{67}$$

with the sum running over n terms since then the dominating terms in the expressions above vanish (see equations (62) and (66)) [3]. A full sweet spot is only possible if each term in the sum vanishes simultaneously and a sweet spot of order n requires that n terms are zero. This condition corresponds to an extremum of the qubit energy gap with respect to the noisy parameter q. In the following we denote sweet spots of the order $n = 1$ and $n = 2$ as single sweet spots (SSSs) and double sweet spots (DSSs).

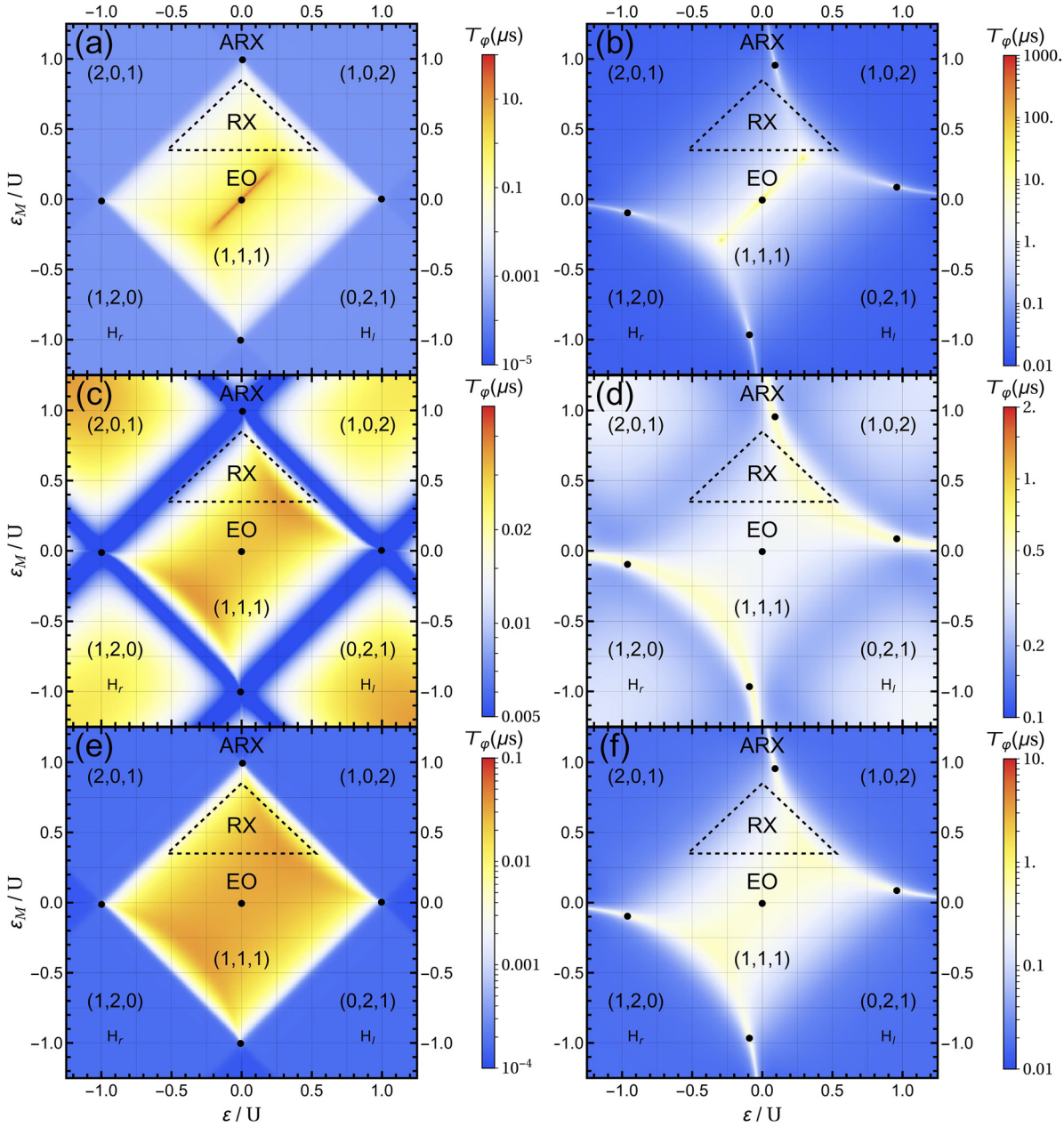

Figure 14. Dephasing time T_φ given by equation (66) due to longitudinal noise as a function of the detuning parameters ε and ε_M. In the top row ((a) and (b)) we plot T_φ resulting from charge noise in the two detuning parameters ε and ε_M, in the center row ((c) and (d)) we plot T_φ resulting from charge noise in the two tunneling parameter t_l and t_r, and in the bottom row ((e) and (f)) we plot T_φ resulting from charge noise from all four parameters combined, where we choose the parameter settings identical in each column. The left column shows results for weak tunneling and strong noise while in the right column, results for strong tunneling and weak noise are plotted. Parameters are set as follows; $t_l = 0.022\,U$, $t_r = 0.015\,U$, $A_q = (10^{-3}\,U)^2$ where $q = \varepsilon, \varepsilon_M$ in (a) and (e), and $A_q = (10^{-4}\,U)^2$, where $q = t_l, t_r$ in (c) and (e), for the left column and $t_l = 0.22\,U$, $t_r = 0.15\,U$, $A_q = (10^{-5}\,U)^2$ where $q = \varepsilon, \varepsilon_M$ in (b) and (f), and $A_{t_l} = A_{t_r} = (10^{-6}\,U)^2$, where $q = t_l, t_r$ in (d) and (f), for the right column. To include a large frequency bandwidth, we globally set the ratio of the lower and higher frequency cut-off $r = 5 \times 10^6$. For the scale of T_φ we used an explicit value of $U = 1$ meV; note that T_φ scales inversely proportional with U. The black dots indicate the DSS. Reprinted with permission from [3] Copyright 2016 by the American Physical Society.

For the detuning parameters, ε and ε_M, there are five known DSSs [3]. One is located in the center of the (1,1,1) charge configuration regime [16, 24] (see figure 14(a)), $\varepsilon = \varepsilon_M = 0$ (for symmetric charging energies), and the motivation behind the AEON qubit (see section 2.3.3). The reason for this is the high degree of symmetry this point possesses, being aligned symmetrically to the four charge configurations (1, 0, 2), (2, 0, 1), (1, 2, 0), and (0, 2, 1) and in the center of the (1, 1, 1) charge configuration regime yielding a real minimum of the energy gap. The other four DSS are located each at the charge transitions between two neighboring asymmetric ((1, 0, 2), (2, 0, 1), (1, 2, 0), or (0, 2, 1)) and the (1, 1, 1) charge configuration [3, 20]. They are approximately located at $(\varepsilon, \varepsilon_M) = (0, U), (0, -U), (-U, 0), (U, 0)$ (see figure 14(a))

whereby the real positions are slightly shifted due to the influence of the other charge configurations. Since these four DSSs possess less symmetry these positions are not minima of ω but correspond to saddle points [3]. Taking into account also the second order effects, the center DSS is clearly favorable compared to the remaining four DSS (see figure 14(a)). The explanation of such case, e.g. for the top DSS that corresponds to the $(2,0,1) \leftrightarrow (1,0,2)$ charge transition, would be the large electric dipole moment between the (2, 0, 1) and (1, 0, 2) states providing a channel through which charge noise couples to the qubit. On the other hand, the center DSS possesses only a vanishing electric dipole moment providing a better protection [3, 16]. Increasing the strength of the tunnel couplings, experimentally achieved by lowering of the tunnel barriers, smoothens out the curvature, giving rise to longer dephasing times and decreasing difference between the DSSs (see figure 14(b)). The drawback of the center DSS is that its energy gap is minimal, making the gate operations slower. Since charge noise through ε_M is claimed to be ten times smaller [310] it can be sufficient to work on a SSS with respect to only ε noise combined with a strong exchange splitting (RX regime) [5, 6]. As experimentally demonstrated, when working at a SSS, the dephasing time is increased significantly, reaching $T_2 = 19\ \mu$s while measuring a larger spectral density exponent. This indicates that higher order effects play the dominating role, thus, a telltale sign of a sweet spot. However, this measurement includes also nuclear noise, making it difficult to differentiate between these two [5].

For noisy tunneling parameters, t_l and t_r, there exist no such DSSs where the impacts of both tunneling parameters are minimized simultaneously [3] (see figures 14(c) and (d)). Therefore, only single SSSs exist which are located at the charge transitions associated with the tunneling parameter, e.g. t_l is minimized nearby the $(2,0,1) \leftrightarrow (1,1,1)$ charge configuration [3]. With their strong impact, fluctuations in the tunnel couplings altogether limit the dephasing times significantly and even more strongly than detuning noise if both fluctuations are comparable in strength. Since the effect of fluctuating tunnel barriers on the tunnel couplings is still under investigation, only qualitative conclusions are possible at this stage [3]. Such a qualitative comparison is shown in figures 14(e) and (f).

4.2.3. Spin-phonon relaxation. Additionally to dephasing, charge noise can also induce relaxation of the qubits via the electron–phonon interaction [22, 78, 322–324] through the dipole moment of the qubit [6, 18]. The phonons in the host material create an electrical field, e.g. polar or piezo-electric phonons, which couples via the electric dipole moment to the qubit inducing relaxation. Direct spin-flips are forbidden due to the dipole transition rules, however, can be mediated by mechanism such as spin–orbit interaction. This interaction depends on the lattice symmetry of the host material and is described for the most common materials (GaAs and silicon with strain in [0 0 1] ($\hat{z}'$) direction) by [6, 18]

$$H_{\mathrm{ep}}^{\mathrm{Ga}} = \sum_{\mu,\boldsymbol{k}} M_k \sqrt{\frac{\hbar}{2\rho_0 V_0 c_\mu k}}\,(\boldsymbol{k}\cdot\hat{\boldsymbol{\epsilon}}_{\mu,\boldsymbol{k}}\Xi_l - \mathrm{i}\Xi)(a_{\mu,\boldsymbol{k}} + a^\dagger_{\mu,-\boldsymbol{k}}), \tag{68}$$

$$H_{\mathrm{ep}}^{\mathrm{Si}} = \sum_{\mu,\boldsymbol{k}} M_k \sqrt{\frac{\hbar}{2\rho_0 V_0 c_\mu k}}\,(\boldsymbol{k}\cdot\hat{\boldsymbol{\epsilon}}_{\mu,\boldsymbol{k}}\Xi_d + k_{z'}\hat{z}'\cdot\hat{\boldsymbol{\epsilon}}_{\mu,\boldsymbol{k}}\Xi_u)(a_{\mu,\boldsymbol{k}} + a^\dagger_{\mu,-\boldsymbol{k}}) \tag{69}$$

$$M_k = \sum_{i,j=1}^{3}\sum_{\sigma}\langle i|\mathrm{e}^{\mathrm{i}\boldsymbol{k}\cdot\boldsymbol{r}}|j\rangle c^\dagger_{i,\sigma}c_{j,\sigma}.$$

Here, $a^\dagger_{\mu,-\boldsymbol{k}}$ ($a_{\mu,-\boldsymbol{k}}$) creates (annihilates) a phonon with wave vector $\boldsymbol{k}$, polarization μ, sound speed c_μ, and unit polarization vector $\hat{\boldsymbol{\epsilon}}_{\mu,\boldsymbol{k}}$. System material dependent parameters are the Volume V_0 and the density of mass ρ_0, while the host material dependent parameters are the longitudinal deformation potential Ξ_l and the piezoelectric constant Ξ for GaAs, and the dilation and the uniaxial deformation potential (Ξ_d and Ξ_u) for silicon [325]. Note, the expressions for the two materials only differ by a single term, as there is no strain in GaAs and no piezoelectric phonons present in silicon.

The relaxation rates can now be calculated via Fermi's golden rule [6, 18] $1/T^1 = \Gamma \sim |\langle g|H_{\mathrm{ep}}|e\rangle|^2\,\rho(\omega)$ where $\rho(\omega)$ is the phonon density evaluated at the qubit energy gap $\hbar\omega$. Within a simple model one finds for GaAs [6], $\Gamma \sim (\omega^3/\nu^2_{\mathrm{GaAs}})\xi^4$, and silicon, $\Gamma \sim (\omega^5/\nu^2_{\mathrm{Si}})\xi^4$, with the fitting parameters $\nu_{\mathrm{GaAs,Si}}$ and the ratio between tunneling and the quadrupolar detuning $\xi = t/(\varepsilon_M - U)$. These results agree well with experimental and theoretical investigations [22, 155, 326] of single and double quantum dots showing the dominance of piezoelectric phonons ($\sim\omega^3$) for GaAs and their absence in silicon ($\sim\omega^5$). Using realistic parameter settings it is estimated that these relaxation rates are small in GaAs [6], $\Gamma \sim$ 1–100 kHz and even smaller in Si [18], $\Gamma =$ 1–100 Hz. Therefore, Si is better protected due to the absence of piezo-electric phonons. It should, however, be noted that studies which include valley physics (see next paragraph) and their effect on the relaxation rates is still an open problem.

4.2.4. Nuclear spin free materials and valley degree of freedom. Despite the better performance of silicon an important factor is the six-fold (valley) degeneracy of the ground-state in bulk silicon. Applying strain raises four of the six valleys in energy such that there exists in silicon QDs an additional two-fold valley degeneracy which has the properties of a pseudo-spin [79]. This two-fold valley degeneracy can be lifted by interfaces in the 2DEG, however, the exact orientation and splitting of the valley depends on atomistic steps of the interface [327–335]. Additional imperfections in the cut-angle lead to a valley-orbit mixing [327, 328], thus, the valley degree of freedom is not a good quantum number anymore. This all together makes the valley splitting very unpredictable and difficult to deal with, since it opens several additional leakage channels due to the increased number of total states (with equivalent spin numbers). Further research is required to fully understand and control the valley splitting before it can be used constructively.

In SiMOS devices the valley splitting is controllable to some degree by an electric field perpendicular to the interface [63, 90, 334–340] which pushes the electrons into the overlap changing

the overlap of the electron wavefunctions with the interface steps. There are theoretical concepts of utilizing the valley as an additional qubit [329, 330], however, due to the unpredictable nature a large valley splitting is typically preferred in experiments involving silicon as the host material.

5. Perspectives

This review describes the recent experimental and theoretical progress and achievements in three-spin qubits that were initially proposed over a decade ago. Several realizations of the three-spin qubits have been discussed, such as the exchange-only qubit, the spin-charge qubit, the hybrid qubit, the resonant exchange qubit, and the always-on exchange only qubit, with special attention to their potential to fulfill the DiVincenzo criteria [36]. We organize our summary according to these five criteria.

(i) Having a scalable system with well-defined qubits. Electron spins fulfill definitely the requirement of well-defined qubits; thus, three-spin qubits inherit this property if encoded in a proper subspace which is the case. The requirement, however, can be violated by leakage since the three-spin qubit is encoded only in a subspace of the full three-spin space. But external global magnetic fields and the exchange interaction can be used to energetically separate the qubit space from the non-computational space, thus, reducing the leakage to a manageable quantity. Scalability follows from the geometry of the quantum dots and the gate electrodes.

(ii) Being able to initialize a proper state such as $|00000\cdots\rangle$. Spin-to-charge conversion allows to initialize a state with a probability close to 1. Two electrons filled in a single dot nearly always relax into a singlet ground-state after a sufficiently long time depending on the experimental setup which afterwards can be adiabatically transformed into a $|0\rangle$ state.

(iii) Having a long decoherence time, or more precisely a sufficient number of gate operations while the qubit is coherent. Three-spin qubits possess a natural robustness against some noise since they are encoded in a decoherence free subspace. Using isotopically purified host materials and operating on a charge noise sweet spot one can mitigate the two main sources of decoherence, allowing for large coherence times. The other possibility is to speed up the gate operations which is realized by utilizing the fast exchange interaction based operations.

(iv) Having a universal set of quantum gates. Three-spin qubits allow for a very fast and highly precise way for operating single-qubit gates. Utilizing the exchange interaction leads to gates in sub-nanosecond time scales $\tau_g \approx 200$ ps, and fidelity exceeding 99% or using resonant driving allows for gate times on the order of nanoseconds, $\tau_g \approx 2.5$ ns. Both of these are significantly faster than qubit implementations using a single electron spin. However, fast exchange-based two-qubit gates either consist of complex sequences with more than 10 pulses or can leak into the non-computational space. Nonetheless, the large dipole moment of three-spin qubits makes up for this since it allows for fast long-ranged two-qubit interactions utilizing a cavity as a mediator.

(v) Having high fidelity and qubit-specific measurements. Spin-to-charge conversion combined with charge-sensitive detectors such as quantum point contacts or single electron transistors allow for precise and fast read-out schemes. Concepts using cavity quantum electrodynamics also allow for fast read-out.

In summary, three-spin qubits provide a realistic path forward to solid-state quantum information processing. Further research will be required to explore this path and address the challenges outlined in this review.

Acknowledgments

We acknowledge funding from ARO through Grant No. W911NF-15-1-0149 and the DFG through SFB 767. We also thank M Brooks, C Peterfalvi, and M Rancic for discussions contributing to this review. Special thanks also go to M Brooks for proof reading the manuscript.

References

[1] Bacon D, Kempe J, Lidar D A and Whaley K B 2000 Universal fault-tolerant quantum computation on decoherence-free subspaces *Phys. Rev. Lett.* **85** 1758–61
[2] DiVincenzo D P, Bacon D, Kempe J, Burkard G and Whaley K B 2000 Universal quantum computation with the exchange interaction *Nature* **408** 339
[3] Russ M, Ginzel F and Burkard G 2016 Coupling of three-spin qubits to their electric environment *Phys. Rev.* B **94** 165411
[4] Laird E A, Taylor J M, DiVincenzo D P, Marcus C M, Hanson M P and Gossard A C 2010 Coherent spin manipulation in an exchange-only qubit *Phys. Rev.* B **82** 075403
[5] Medford J, Beil J, Taylor J M, Rashba E I, Lu H, Gossard A C and Marcus C M 2013 Quantum-dot-based resonant exchange qubit *Phys. Rev. Lett.* **111** 050501
[6] Taylor J M, Srinivasa V and Medford J 2013 Electrically protected resonant exchange qubits in triple quantum dots *Phys. Rev. Lett.* **111** 050502
[7] Kyriakidis J and Burkard G 2007 Universal quantum computing with correlated spin-charge states *Phys. Rev.* B **75** 115324
[8] Shi Z *et al* 2012 Fast hybrid silicon double-quantum-dot qubit *Phys. Rev. Lett.* **108** 140503
[9] Koh T S, Gamble J K, Friesen M, Eriksson M A and Coppersmith S N 2012 Pulse-gated quantum-dot hybrid qubit *Phys. Rev. Lett.* **109** 250503
[10] Cao G *et al* 2016 Tunable hybrid qubit in a GaAs double quantum dot *Phys. Rev. Lett.* **116** 086801
[11] Thorgrimsson B *et al* 2016 Mitigating the effects of charge noise and improving the coherence of a quantum dot hybrid qubit (arXiv:1611.04945)
[12] Fong B H and Wandzura S M 2011 Universal quantum computation and leakage reduction in the 3-qubit decoherence free subsystem *Quantum Inf. Comput.* **11** 1003–18
[13] Setiawan F, Hui H-Y, Kestner J P, Wang X and Sarma S D 2014 Robust two-qubit gates for exchange-coupled qubits *Phys. Rev.* B **89** 085314

[14] Zeuch D, Cipri R and Bonesteel N E 2014 Analytic pulse-sequence construction for exchange-only quantum computation *Phys. Rev.* B **90** 045306

[15] Doherty A C and Wardrop M P 2013 Two-qubit gates for resonant exchange qubits *Phys. Rev. Lett.* **111** 050503

[16] Shim Y-P and Tahan C 2016 Charge-noise-insensitive gate operations for always-on, exchange-only qubits *Phys. Rev.* B **93** 121410

[17] Russ M and Burkard G 2015 Long distance coupling of resonant exchange qubits *Phys. Rev.* B **92** 205412

[18] Srinivasa V, Taylor J M and Tahan C 2016 Entangling distant resonant exchange qubits via circuit quantum electrodynamics *Phys. Rev.* B **94** 205421

[19] Kempe J, Bacon D, Lidar D A and Whaley K B 2001 Theory of decoherence-free fault-tolerant universal quantum computation *Phys. Rev.* A **63** 042307

[20] Russ M and Burkard G 2015 Asymmetric resonant exchange qubit under the influence of electrical noise *Phys. Rev.* B **91** 235411

[21] Ladd T D 2012 Hyperfine-induced decay in triple quantum dots *Phys. Rev.* B **86** 125408

[22] Mehl S and DiVincenzo D P 2013 Noise analysis of qubits implemented in triple quantum dot systems in a Davies master equation approach *Phys. Rev.* B **87** 195309

[23] Hung J-T, Fei J, Friesen M and Hu X 2014 Decoherence of an exchange qubit by hyperfine interaction *Phys. Rev.* B **90** 045308

[24] Fei J, Hung J-T, Koh T S, Shim Y-P, Coppersmith S N, Hu X and Friesen M 2015 Characterizing gate operations near the sweet spot of an exchange-only qubit *Phys. Rev.* B **91** 205434

[25] West J R and Fong B H 2012 Exchange-only dynamical decoupling in the three-qubit decoherence free subsystem *New J. Phys.* **14** 083002

[26] Rohling N and Burkard G 2016 Optimizing electrically controlled echo sequences for the exchange-only qubit *Phys. Rev.* B **93** 205434

[27] Malinowski F K, Martins F, Nissen P D, Fallahi S, Gardner G C, Manfra M J, Marcus C M and Kuemmeth F 2017 Symmetric operation of the resonant exchange qubit (arXiv:1704.01298)

[28] Nielsen M and Chuang I 2000 *Quantum Computation and Quantum Information* (*Cambridge Series on Information and the Natural Sciences*) (Cambridge: Cambridge University Press) (https://doi.org/10.1017/CBO9780511976667)

[29] Feynman R P 1982 Simulating physics with computers *Int. J. Theor. Phys.* **21** 467–88

[30] Lloyd S 1996 Universal quantum simulators *Science* **273** 1073–8

[31] Shor P W 1997 Polynomial-time algorithms for prime factorization and discrete logarithms on a quantum computer *SIAM J. Comput.* **26** 1484

[32] Rivest R L, Shamir A and Adleman L 1978 A method for obtaining digital signatures and public-key cryptosystems *Commun. ACM* **21** 120

[33] Grover L K 1996 A fast quantum mechanical algorithm for database search *Proc. 28th Annual ACM Symp. on Theory of Computing (ACM, New York, NY, USA)* p 212

[34] Grover L K 1998 Quantum computers can search rapidly by using almost any transformation *Phys. Rev. Lett.* **80** 4329–32

[35] Lloyd S 1993 A potentially realizable quantum computer *Science* **261** 1569–71

[36] DiVincenzo D P 2000 The physical implementation of quantum computation *Fortsch. Phys.* **48** 771–83

[37] Kloeffel C and Loss D 2013 Prospects for spin-based quantum computing in quantum dots *Ann. Rev. Condens. Matter Phys.* **4** 51–81

[38] Vandersypen L M K and Chuang I L 2005 Nmr techniques for quantum control and computation *Rev. Mod. Phys.* **76** 1037–69

[39] Miller R, Northup T E, Birnbaum K M, Boca A, Boozer A D and Kimble H J 2005 Trapped atoms in cavity QED: coupling quantized light and matter *J. Phys. B: At. Mol. Opt. Phys.* **38** S551

[40] Cirac J I and Zoller P 1995 Quantum computations with cold trapped ions *Phys. Rev. Lett.* **74** 4091–4

[41] Nakamura Y, Pashkin Y A and Tsai J S 1999 Coherent control of macroscopic quantum states in a single-cooper-pair box *Nature* **398** 786–8

[42] Makhlin Y, Schön G and Shnirman A 2001 Quantum-state engineering with Josephson-junction devices *Rev. Mod. Phys.* **73** 357–400

[43] Kane B E 1998 A silicon-based nuclear spin quantum computer *Nature* **393** 133

[44] Doherty M W, Manson N B, Delaney P, Jelezko F, Wrachtrup J and Hollenberg L C L 2013 The nitrogen-vacancy colour centre in diamond *Phys. Rep.* **528** 1–45

[45] Dobrovitski V V, Fuchs G D, Falk A L, Santori C and Awschalom D D 2013 Quantum control over single spins in diamond *Ann. Rev. Condens. Matter Phys.* **4** 23–50

[46] Weber J R, Koehl W F, Varley J B, Janotti A, Buckley B B, de Walle C G V and Awschalom D D 2011 Defects in sic for quantum computing *J. Appl. Phys.* **109** 102417

[47] Kok P, Munro W J, Nemoto K, Ralph T C, Dowling J P and Milburn G J 2007 Linear optical quantum computing with photonic qubits *Rev. Mod. Phys.* **79** 135–74

[48] Pérez-Delgado C A and Kok P 2011 Quantum computers: definition and implementations *Phys. Rev.* A **83** 012303

[49] Martinis J M 2015 Qubit metrology for building a fault-tolerant quantum computer *npj Quantum Inf.* **1** 15005

[50] Gaudreau L, Studenikin S A, Sachrajda A S, Zawadzki P, Kam A, Lapointe J, Korkusinski M and Hawrylak P 2006 Stability diagram of a few-electron triple dot *Phys. Rev. Lett.* **97** 036807

[51] Schröer D, Greentree A D, Gaudreau L, Eberl K, Hollenberg L C L, Kotthaus J P and Ludwig S 2007 Electrostatically defined serial triple quantum dot charged with few electrons *Phys. Rev.* B **76** 075306

[52] Ihn T, Sigrist M, Ensslin K, Wegscheider W and Reinwald M 2007 Interference in a quantum dot molecule embedded in a ring interferometer *New J. Phys.* **9** 111

[53] Rogge M C and Haug R J 2008 Noninvasive detection of molecular bonds in quantum dots *Phys. Rev.* B **78** 153310

[54] Gaudreau L, Kam A, Granger G, Studenikin S A, Zawadzki P and Sachrajda A S 2009 A tunable few electron triple quantum dot *Appl. Phys. Lett.* **95** 193101

[55] Yamahata G, Tsuchiya Y, Mizuta H, Uchida K and Oda S 2009 Electron transport through silicon serial triple quantum dots *Solid-State Electron.* **53** 779–85 (papers Selected from the *38th European Solid-State Device Research Conf.*)

[56] Pierre M, Wacquez R, Roche B, Jehl X, Sanquer M, Vinet M, Prati E, Belli M and Fanciulli M 2009 Compact silicon double and triple dots realized with only two gates *Appl. Phys. Lett.* **95** 242107

[57] Takakura T, Pioro-Ladrière M, Obata T, Shin Y-S, Brunner R, Yoshida K, Taniyama T and Tarucha S 2010 Triple quantum dot device designed for three spin qubits *Appl. Phys. Lett.* **97** 212104

[58] Granger G, Gaudreau L, Kam A, Pioro-Ladrière M, Studenikin S A, Wasilewski Z R, Zawadzki P and Sachrajda A S 2010 Three-dimensional transport diagram of a triple quantum dot *Phys. Rev.* B **82** 075304

[59] Gaudreau L, Granger G, Kam A, Aers G C, Studenikin S A, Zawadzki P, Pioro-Ladriere M, Wasilewski Z R and Sachrajda A S 2012 Coherent control of three-spin states in a triple quantum dot *Nat. Phys.* **8** 54

[60] Amaha S, Hatano T, Tamura H, Teraoka S, Kubo T, Tokura Y, Austing D G and Tarucha S 2012 Resonance-hybrid states in a triple quantum dot *Phys. Rev.* B **85** 081301

[61] Pan H, House M G, Hao X and Jiang H W 2012 Fabrication and characterization of a silicon metal-oxide-semiconductor based triple quantum dot *Appl. Phys. Lett.* **100** 263109

[62] Busl M *et al* 2013 Bipolar spin blockade and coherent state superpositions in a triple quantum dot *Nat. Nanotechnol.* **8** 261–5

[63] Kim D *et al* 2014 Quantum control and process tomography of a semiconductor quantum dot hybrid qubit *Nature* **511** 70–4

[64] Shi Z *et al* 2014 Fast coherent manipulation of three-electron states in a double quantum dot *Nat. Commun.* **5** e1500214

[65] Kim D, Ward D R, Simmons C B, Savage D E, Lagally M G, Friesen M, Coppersmith S N and Eriksson M A 2015 High-fidelity resonant gating of a silicon-based quantum dot hybrid qubit *Npj Quantum Inf.* **1** 15004

[66] Aers G C, Studenikin S A, Granger G, Kam A, Zawadzki P, Wasilewski Z R and Sachrajda A S 2012 Coherent exchange and double beam splitter oscillations in a triple quantum dot *Phys. Rev.* B **86** 045316

[67] Medford J, Beil J, Taylor J M, Bartlett S D, Doherty A C, Rashba E I, DiVincenzo D P, Lu H, Gossard A C and Marcus C M 2013 Self-consistent measurement and state tomography of an exchange-only spin qubit *Nat. Nanotechnol.* **8** 654

[68] Sanchez R, Granger G, Gaudreau L, Kam A, Pioro-Ladriere M, Studenikin S A, Zawadzki P, Sachrajda A S and Platero G 2014 Long-range spin transfer in triple quantum dots *Phys. Rev. Lett.* **112** 176803

[69] Eng K *et al* 2015 Isotopically enhanced triple-quantum-dot qubit *Sci. Adv.* **1** e1500214

[70] Poulin-Lamarre G, Thorgrimson J, Studenikin S A, Aers G C, Kam A, Zawadzki P, Wasilewski Z R and Sachrajda A S 2015 Three-spin coherent oscillations and interference *Phys. Rev.* B **91** 125417

[71] Scarola V W, Park K and Sarma S D 2004 Chirality in quantum computation with spin cluster qubits *Phys. Rev. Lett.* **93** 120503

[72] Scarola V W and Sarma S D 2005 Exchange gate in solid-state spin-quantum computation: the applicability of the Heisenberg model *Phys. Rev.* A **71** 032340

[73] Hsieh C-Y, Rene A and Hawrylak P 2012 Herzberg circuit and berry's phase in chirality-based coded qubit in a triangular triple quantum dot *Phys. Rev.* B **86** 115312

[74] Łuczak J and Bułka B R 2012 Entanglement in a three spin system controlled by electric and magnetic fields *J. Phys.: Condens. Matter* **24** 375303

[75] Urbaniak M, Tooski S B, Ramšak A and Bułka B R 2014 Thermal entanglement in a triple quantum dot system *Eur. Phys. J.* B **86** 505

[76] Tooski S B, Bułka B R, Žitko R and Ramšak A 2014 Entanglement switching via the kondo effect in triple quantum dots *Eur. Phys. J.* B **87** 145

[77] Łuczak J and Bułka B R 2014 Readout and dynamics of a qubit built on three quantum dots *Phys. Rev.* B **90** 165427

[78] Hanson R, Kouwenhoven L P, Petta J R, Tarucha S and Vandersypen L M K 2007 Spins in few-electron quantum dots *Rev. Mod. Phys.* **79** 1217

[79] Zwanenburg F A, Dzurak A S, Morello A, Simmons M Y, Hollenberg L C L, Klimeck G, Rogge S, Coppersmith S N and Eriksson M A 2013 Silicon quantum electronics *Rev. Mod. Phys.* **85** 961

[80] Recher P, Nilsson J, Burkard G and Trauzettel B 2009 Bound states and magnetic field induced valley splitting in gate-tunable graphene quantum dots *Phys. Rev.* B **79** 085407

[81] Churchill H O H, Kuemmeth F, Harlow J W, Bestwick A J, Rashba E I, Flensberg K, Stwertka C H, Taychatanapat T, Watson S K and Marcus C M 2009 Relaxation and dephasing in a two-electron 13c nanotube double quantum dot *Phys. Rev. Lett.* **102** 166802

[82] Reynoso A A and Flensberg K 2011 Dephasing and hyperfine interaction in carbon nanotube double quantum dots: the clean limit *Phys. Rev.* B **84** 205449

[83] Reynoso A A and Flensberg K 2012 Dephasing and hyperfine interaction in carbon nanotubes double quantum dots: disordered case *Phys. Rev.* B **85** 195441

[84] Song X-X *et al* 2015 A gate defined quantum dot on the two-dimensional transition metal dichalcogenide semiconductor WSe2 *Nanoscale* **7** 16867–73

[85] Song X-X, Zhang Z-Z, You J, Liu D, Li H-O, Cao G, Xiao M and Guo G-P 2015 Temperature dependence of coulomb oscillations in a few-layer two-dimensional WS2 quantum dot *Sci. Rep.* **5** 16113

[86] Laird E A, Kuemmeth F, Steele G A, Grove-Rasmussen K, Nygård J, Flensberg K and Kouwenhoven L P 2015 Quantum transport in carbon nanotubes *Rev. Mod. Phys.* **87** 703–64

[87] Wang K, Taniguchi T, Watanabe K and Kim P 2016 Engineering quantum confinement in semiconducting van der Waals heterostructure (arXiv:1610.02929)

[88] Angus S J, Ferguson A J, Dzurak A S and Clark R G 2007 Gate-defined quantum dots in intrinsic silicon *Nano Lett.* **7** 2051–5

[89] Jones C, Gyure M F, Ladd T D, Fogarty M A, Morello A and Dzurak A S 2016 A logical qubit in a linear array of semiconductor quantum dots (arXiv:1608.06335)

[90] Yang C H, Rossi A, Ruskov R, Lai N S, Mohiyaddin F A, Lee S, Tahan C, Klimeck G, Morello A and Dzurak A S 2013 Spin-valley lifetimes in a silicon quantum dot with tunable valley splitting *Nat. Commun.* **4** 2069

[91] Veldhorst M *et al* 2014 An addressable quantum dot qubit with fault-tolerant control-fidelity *Nat. Nanotechnol.* **9** 981–5

[92] Muhonen J T *et al* 2014 Storing quantum information for 30 seconds in a nanoelectronic device *Nat. Nanotechnol.* **9** 986–91

[93] Morello A 2015 Silicon quantum dots: fine-tuning to maturity *Nanotechnology* **26** 502501

[94] Borselli M G *et al* 2015 Undoped accumulation-mode Si/SiGe quantum dots *Nanotechnology* **26** 375202

[95] Zajac D M, Hazard T M, Mi X, Wang K and Petta J R 2015 A reconfigurable gate architecture for Si/SiGe quantum dots *Appl. Phys. Lett.* **106** 223507

[96] Reed M D *et al* 2016 Reduced sensitivity to charge noise in semiconductor spin qubits via symmetric operation *Phys. Rev. Lett.* **116** 110402

[97] Ward D R, Kim D, Savage D E, Lagally M G, Foote R H, Friesen M, Coppersmith S N and Eriksson M A 2016 State-conditional coherent charge qubit oscillations in a Si/SiGe quadruple quantum dot *npj Quantum Inf.* **2** 16032

[98] Knapp T J *et al* 2016 Characterization of a gate-defined double quantum dot in a Si/SiGe nanomembrane *Nanotechnology* **27** 154002

[99] Zajac D M, Hazard T M, Mi X, Nielsen E and Petta J R 2016 Scalable gate architecture for densely packed semiconductor spin qubits *Phys. Rev. Applied* **6** 054013

[100] Itoh K M and Watanabe H 2014 Isotope engineering of silicon and diamond for quantum computing and sensing applications *MRS Commun.* **4** 143–57

[101] Kawakami E, Scarlino P, Ward D R, Braakman F R, Savage D E, Lagally M G, Friesen M, Coppersmith S N, Eriksson M A and Vandersypen L M K 2014 Electrical control of a long-lived spin qubit in a Si/SiGe quantum dot *Nat. Nanotechnol.* **9** 666–70

[102] Field M, Smith C G, Pepper M, Ritchie D A, Frost J E F, Jones G A C and Hasko D G 1993 Measurements of coulomb blockade with a noninvasive voltage probe *Phys. Rev. Lett.* **70** 1311–4

[103] Barthel C, Reilly D J, Marcus C M, Hanson M P and Gossard A C 2009 Rapid single-shot measurement of a singlet-triplet qubit *Phys. Rev. Lett.* **103** 160503

[104] Devoret M H and Schoelkopf R J 2000 Amplifying quantum signals with the single-electron transistor *Nature* **406** 1039–46

[105] Barthel C, Kjærgaard M, Medford J, Stopa M, Marcus C M, Hanson M P and Gossard A C 2010 Fast sensing of double-dot charge arrangement and spin state with a radio-frequency sensor quantum dot *Phys. Rev.* B **81** 161308

[106] House M G, Bartlett I, Pakkiam P, Koch M, Peretz E, van der Heijden J, Kobayashi T, Rogge S and Simmons M Y 2016 High-sensitivity charge detection with a single-lead quantum dot for scalable quantum computation *Phys. Rev. Appl.* **6** 044016

[107] House M G, Peretz E, Keizer J G, Hile S J and Simmons M Y 2014 Single-charge detection by an atomic precision tunnel junction *Appl. Phys. Lett.* **104** 113111

[108] Delbecq M R, Schmitt V, Parmentier F D, Roch N, Viennot J J, Fève G, Huard B, Mora C, Cottet A and Kontos T 2011 Coupling a quantum dot, fermionic leads and a microwave cavity on a chip *Phys. Rev. Lett.* **107** 256804

[109] Kerman A J 2013 Quantum information processing using quasiclassical electromagnetic interactions between qubits and electrical resonators *New J. Phys.* **15** 123011

[110] Gonzalez-Zalba M F, Barraud S, Ferguson A J and Betz A C 2015 Probing the limits of gate-based charge sensing *Nat. Commun.* **6** 6084

[111] Didier N, Bourassa J and Blais A 2015 Fast quantum nondemolition readout by parametric modulation of longitudinal qubit-oscillator interaction *Phys. Rev. Lett.* **115** 203601

[112] Burkard G and Petta J R 2016 Dispersive readout of valley splittings in cavity-coupled silicon quantum dots *Phys. Rev.* B **94** 195305

[113] Mi X, Cady J V, Zajac D M, Stehlik J, Edge L F and Petta J R 2017 Circuit quantum electrodynamics architecture for gate-defined quantum dots in silicon *Appl. Phys. Lett.* **4** 043502

[114] Beaudoin F, Blais A and Coish W A 2017 Hamiltonian engineering for robust quantum state transfer and qubit readout in cavity QED *New J. Phys.* **19** 023041

[115] Stockklauser A *et al* 2017 Strong coupling cavity QED with gate-defined double quantum dots enabled by a high impedance resonator *Phys. Rev.* X **7** 011030

[116] Ruskov R and Tahan C 2017 Quantum-limited measurement of spin qubits via curvature coupling to a cavity (arXiv:1704.05876)

[117] Mi X, Peterfalvi C G, Burkard G and Petta J R 2017 High resolution valley spectroscopy of Si quantum dots (arXiv:1704.06312)

[118] Petta J R, Johnson A C, Taylor J M, Laird E A, Yacoby A, Lukin M D, Marcus C M, Hanson M P and Gossard A C 2005 Coherent manipulation of coupled electron spins in semiconductor quantum dots *Science* **309** 2180

[119] Hubbard J 1963 Electron correlations in narrow energy bands *Proc. R. Soc. Lond.* A **276** 238

[120] Burkard G, Loss D and DiVincenzo D P 1999 Coupled quantum dots as quantum gates *Phys. Rev.* B **59** 2070

[121] Schrieffer J R and Wolff P A 1966 Relation between the Anderson and Kondo Hamiltonians *Phys. Rev.* **149** 491–2

[122] Bravyi S, Divincenzo D P and Loss D 2011 Schrieffer–Wolff transformation for quantum many-body systems *Ann. Phys.* **326** 2793

[123] Loss D and DiVincenzo D P 1998 Quantum computation with quantum dots *Phys. Rev.* A **57** 120

[124] Koppens F H L, Buizert C, Tielrooij K J, Vink I T, Nowack K C, Meunier T, Kouwenhoven L P and Vandersypen L M K 2006 Driven coherent oscillations of a single electron spin in a quantum dot *Nature* **442** 766

[125] Golovach V N, Borhani M and Loss D 2006 Electric-dipole-induced spin resonance in quantum dots *Phys. Rev.* B **74** 165319

[126] Nowack K C, Koppens F H L, Nazarov Y V and Vandersypen L M K 2007 Coherent control of a single electron spin with electric fields *Science* **318** 1430

[127] Khomitsky D V, Gulyaev L V and Sherman E Y 2012 Spin dynamics in a strongly driven system: very slow rabi oscillations *Phys. Rev.* B **85** 125312

[128] Li R, You J Q, Sun C P and Nori F 2013 Controlling a nanowire spin–orbit qubit via electric-dipole spin resonance *Phys. Rev. Lett.* **111** 086805

[129] Nadj-Perge S, Frolov S M, Bakkers E P A M and Kouwenhoven L P 2010 Spin–orbit qubit in a semiconductor nanowire *Nature* **468** 1084–7

[130] Tokura Y, van der Wiel W G, Obata T and Tarucha S 2006 Coherent single electron spin control in a slanting zeeman field *Phys. Rev. Lett.* **96** 047202

[131] Obata T, Pioro-Ladrière M, Tokura Y, Shin Y-S, Kubo T, Yoshida K, Taniyama T and Tarucha S 2010 Coherent manipulation of individual electron spin in a double quantum dot integrated with a micromagnet *Phys. Rev.* B **81** 085317

[132] Laird E A, Barthel C, Rashba E I, Marcus C M, Hanson M P and Gossard A C 2007 Hyperfine-mediated gate-driven electron spin resonance *Phys. Rev. Lett.* **99** 246601

[133] Pioro-Ladriere M, Obata T, Tokura Y, Shin Y S, Kubo T, Yoshida K, Taniyama T and Tarucha S 2008 Electrically driven single-electron spin resonance in a slanting zeeman field *Nat. Phys.* **4** 776–9

[134] Brunner R, Shin Y-S, Obata T, Pioro-Ladrière M, Kubo T, Yoshida K, Taniyama T, Tokura Y and Tarucha S 2011 Two-qubit gate of combined single-spin rotation and interdot spin exchange in a double quantum dot *Phys. Rev. Lett.* **107** 146801

[135] Elzerman J M, Hanson R, Willems van Beveren L H, Witkamp B, Vandersypen L M K and Kouwenhoven L P 2004 Single-shot read-out of an individual electron spin in a quantum dot *Nature* **430** 431

[136] Foletti S, Bluhm H, Mahalu D, Umansky V and Yacoby A 2009 Universal quantum control of two-electron spin quantum bits using dynamic nuclear polarization *Nat. Phys.* **5** 903

[137] Culcer D, Hu X and Das Sarma S 2009 Dephasing of Si spin qubits due to charge noise *Appl. Phys. Lett.* **95** 073102

[138] Vion D, Aassime A, Cottet A, Joyez P, Pothier H, Urbina C, Esteve D and Devoret M H 2002 Manipulating the quantum state of an electrical circuit *Science* **296** 886

[139] Paladino E, Galperin Y M, Falci G and Altshuler B L 2014 1/*f* noise: implications for solid-state quantum information *Rev. Mod. Phys.* **86** 361–418

[140] Gong B, Wang L, Tu T, Li C-F and Guo G-C 2016 Robust universal gates for quantum-dot spin qubits using tunable adiabatic passages *Phys. Rev.* A **94** 032311

[141] Chirolli L and Burkard G 2008 Decoherence in solid-state qubits *Adv. Phys.* **57** 225–85

[142] Merkulov I A, Efros A L and Rosen M 2002 Electron spin relaxation by nuclei in semiconductor quantum dots *Phys. Rev.* B **65** 205309

[143] Coish W A and Loss D 2004 Hyperfine interaction in a quantum dot: non-markovian electron spin dynamics *Phys. Rev.* B **70** 195340

[144] Fischer J, Trif M, Coish W and Loss D 2009 Spin interactions, relaxation and decoherence in quantum dots *Solid State Commun.* **149** 1443–50

[145] Coish W A and Baugh J 2009 Nuclear spins in nanostructures *Phys. Status Solidi* b **246** 2203–15

[146] Khaetskii A V and Nazarov Y V 2001 Spin-flip transitions between zeeman sublevels in semiconductor quantum dots *Phys. Rev.* B **64** 125316

[147] Golovach V N, Khaetskii A and Loss D 2004 Phonon-induced decay of the electron spin in quantum dots *Phys. Rev. Lett.* **93** 016601

[148] Sherman E Y and Lockwood D J 2005 Spin relaxation in quantum dots with random spin–orbit coupling *Phys. Rev.* B **72** 125340

[149] Bulaev D V and Loss D 2005 Spin relaxation and anticrossing in quantum dots: Rashba versus Dresselhaus spin–orbit coupling *Phys. Rev.* B **71** 205324

[150] Fal'ko V I, Altshuler B L and Tsyplyatyev O 2005 Anisotropy of spin splitting and spin relaxation in lateral quantum dots *Phys. Rev. Lett.* **95** 076603

[151] Prada M and Pfannkuche D 2017 Anisotropy of spin coherence in high mobility quantum wells with arbitrary magnetic fields *Phys. Rev.* B **95** 045421

[152] Koppens F H L, Nowack K C and Vandersypen L M K 2008 Spin echo of a single electron spin in a quantum dot *Phys. Rev. Lett.* **100** 236802

[153] Bluhm H, Foletti S, Neder I, Rudner M, Mahalu D, Umansky V and Yacoby A 2011 Dephasing time of GaAs electron-spin qubits coupled to a nuclear bath exceeding 200 μs *Nat. Phys.* **7** 109

[154] Malinowski F K *et al* 2017 Notch filtering the nuclear environment of a spin qubit *Nat. Nanotechnol.* **12** 16–20

[155] Amasha S, MacLean K, Radu I P, Zumbühl D M, Kastner M A, Hanson M P and Gossard A C 2008 Electrical control of spin relaxation in a quantum dot *Phys. Rev. Lett.* **100** 046803

[156] Levy J 2002 Universal quantum computation with spin-1/2 pairs and Heisenberg exchange *Phys. Rev. Lett.* **89** 147902

[157] Klinovaja J, Stepanenko D, Halperin B I and Loss D 2012 Exchange-based CNOT gates for singlet-triplet qubits with spin–orbit interaction *Phys. Rev.* B **86** 085423

[158] Wardrop M P and Doherty A C 2014 Exchange-based two-qubit gate for singlet-triplet qubits *Phys. Rev.* B **90** 045418

[159] Taylor J M, Engel H-A, Dur W, Yacoby A, Marcus C M, Zoller P and Lukin M D 2005 Fault-tolerant architecture for quantum computation using electrically controlled semiconductor spins *Nat. Phys.* **1** 177

[160] Coish W A and Loss D 2005 Singlet-triplet decoherence due to nuclear spins in a double quantum dot *Phys. Rev.* B **72** 125337

[161] Stepanenko D and Burkard G 2007 Quantum gates between capacitively coupled double quantum dot two-spin qubits *Phys. Rev.* B **75** 085324

[162] Calderon-Vargas F A and Kestner J P 2015 Directly accessible entangling gates for capacitively coupled singlet-triplet qubits *Phys. Rev.* B **91** 035301

[163] Mehl S, Bluhm H and DiVincenzo D P 2014 Two-qubit couplings of singlet-triplet qubits mediated by one quantum state *Phys. Rev.* B **90** 045404

[164] Shulman M D, Dial O E, Harvey S P, Bluhm H, Umansky V and Yacoby A 2012 Demonstration of entanglement of electrostatically coupled singlet-triplet qubits *Science* **336** 202

[165] Srinivasa V and Taylor J M 2015 Capacitively coupled singlet-triplet qubits in the double charge resonant regime *Phys. Rev.* B **92** 235301

[166] Imamoglu A, Awschalom D D, Burkard G, DiVincenzo D P, Loss D, Sherwin M and Small A 1999 Quantum information processing using quantum dot spins and cavity qed *Phys. Rev. Lett.* **83** 4204

[167] Childress L, Sørensen A S and Lukin M D 2004 Mesoscopic cavity quantum electrodynamics with quantum dots *Phys. Rev.* A **69** 042302

[168] Burkard G and Imamoglu A 2006 Ultra-long-distance interaction between spin qubits *Phys. Rev.* B **74** 041307

[169] Hu X, Liu Y-X and Nori F 2012 Strong coupling of a spin qubit to a superconducting stripline cavity *Phys. Rev.* B **86** 035314

[170] Petersson K D, McFaul L W, Schroer M D, Jung M, Taylor J M, Houck A A and Petta J R 2012 Circuit quantum electrodynamics with a spin qubit *Nature* **490** 380

[171] Viennot J J, Dartiailh M C, Cottet A and Kontos T 2015 Coherent coupling of a single spin to microwave cavity photons *Science* **349** 408–11

[172] Samkharadze N, Bruno A, Scarlino P, Zheng G, DiVincenzo D P, DiCarlo L and Vandersypen L M K 2016 High-kinetic-inductance superconducting nanowire resonators for circuit QED in a magnetic field *Phys. Rev. Appl.* **5** 044004

[173] Bruhat L E, Cubaynes T, Viennot J J, Dartiailh M C, Desjardins M M, Cottet A and Kontos T 2016 Strong coupling between an electron in a quantum dot circuit and a photon in a cavity (arXiv:1612.05214)

[174] Kogan S 1996 *Electronic Noise and Fluctuations in Solids* (Cambridge: Cambridge University Press)

[175] Jung S W, Fujisawa T, Hirayama Y and Jeong Y H 2004 Background charge fluctuation in a GaAs quantum dot device *Appl. Phys. Lett.* **85** 768

[176] Müller J, von Molnár S, Ohno Y and Ohno H 2006 Decomposition of $1/f$ noise in $al_xga_{1-x}As$/GaAs Hall devices *Phys. Rev. Lett.* **96** 186601

[177] Dutta P and Horn P M 1981 Low-frequency fluctuations in solids: $\frac{1}{f}$ noise *Rev. Mod. Phys.* **53** 497–516

[178] Weissman M B 1988 $\frac{1}{f}$ noise and other slow, nonexponential kinetics in condensed matter *Rev. Mod. Phys.* **60** 537–71

[179] Beaudoin F and Coish W A 2015 Microscopic models for charge-noise-induced dephasing of solid-state qubits *Phys. Rev.* B **91** 165432

[180] Ramon G and Hu X 2010 Decoherence of spin qubits due to a nearby charge fluctuator in gate-defined double dots *Phys. Rev.* B **81** 045304

[181] Ramon G 2011 Electrically controlled quantum gates for two-spin qubits in two double quantum dots *Phys. Rev.* B **84** 155329

[182] Hiltunen T, Bluhm H, Mehl S and Harju A 2015 Charge-noise tolerant exchange gates of singlet-triplet qubits in asymmetric double quantum dots *Phys. Rev.* B **91** 075301

[183] Martins F, Malinowski F K, Nissen P D, Barnes E, Fallahi S, Gardner G C, Manfra M J, Marcus C M and Kuemmeth F 2016 Noise suppression using symmetric exchange gates in spin qubits *Phys. Rev. Lett.* **116** 116801

[184] Lidar D A 2014 *Review of Decoherence-Free Subspaces, Noiseless Subsystems and Dynamical Decoupling* (New York: Wiley) pp 295–354

[185] Buchachenko A L and Berdinsky V L 2002 Electron spin catalysis *Chem. Rev.* **102** 603

[186] Waugh F R, Berry M J, Mar D J, Westervelt R M, Campman K L and Gossard A C 1995 Single-electron charging in double and triple quantum dots with tunable coupling *Phys. Rev. Lett.* **75** 705–8

[187] Usukura J, Saiga Y and Hirashima D S 2005 Three-electron systems in quantum nanostructures: ground state transition from a spin-doublet state to a spin-quartet state *J. Phys. Soc. Japan* **74** 1231–9

[188] Korkusinski M, Gimenez I P, Hawrylak P, Gaudreau L, Studenikin S A and Sachrajda A S 2007 Topological hunds rules and the electronic properties of a triple lateral quantum dot molecule *Phys. Rev.* B **75** 115301

[189] Delgado F, Shim Y-P, Korkusinski M and Hawrylak P 2007 Theory of spin, electronic and transport properties of the lateral triple quantum dot molecule in a magnetic field *Phys. Rev.* B **76** 115332

[190] Li Y, Yannouleas C and Landman U 2007 Three-electron anisotropic quantum dots in variable magnetic fields: exact results for excitation spectra, spin structures and entanglement *Phys. Rev.* B **76** 245310

[191] Hsieh C-Y and Hawrylak P 2010 Quantum circuits based on coded qubits encoded in chirality of electron spin complexes in triple quantum dots *Phys. Rev.* B **82** 205311

[192] Hsieh C-Y, Shim Y-P, Korkusinski M and Hawrylak P 2012 Physics of lateral triple quantum-dot molecules with controlled electron numbers *Rep. Prog. Phys.* **75** 114501

[193] van der Wiel W G, De Franceschi S, Elzerman J M, Fujisawa T, Tarucha S and Kouwenhoven L P 2002 Electron transport through double quantum dots *Rev. Mod. Phys.* **75** 1–22

[194] Vidan A, Westervelt R M, Stopa M, Hanson M and Gossard A C 2005 Charging and spin effects in triple dot artificial molecules *J. Supercond.* **18** 223–7

[195] Rogge M C and Haug R J 2009 The three dimensionality of triple quantum dot stability diagrams *New J. Phys.* **11** 113037

[196] Seo M, Choi H K, Lee S-Y, Kim N, Chung Y, Sim H-S, Umansky V and Mahalu D 2013 Charge frustration in a triangular triple quantum dot *Phys. Rev. Lett.* **110** 046803

[197] Broome M A, Gorman S K, Keizer J G, Watson T F, Hile S J, Baker W J and Simmons M Y 2016 Mapping the chemical potential landscape of a triple quantum dot *Phys. Rev.* B **94** 054314

[198] Nguyen K T *et al* 2013 Charge sensed Pauli blockade in a metal-oxide-semiconductor lateral double quantum dot *Nano Lett.* **13** 5785–90

[199] Powell I E 2014 Simulating charge stability diagrams for double and triple quantum dot systems (private communication) www.pa.ucla.edu/sites/default/files/files/REU/Papers%202014/powell.pdf

[200] Russ M and Burkard G Fluctuating charging energies in three-spin qubits unpublished

[201] Mizel A and Lidar D A 2004 Three- and four-body interactions in spin-based quantum computers *Phys. Rev. Lett.* **92** 077903

[202] Hawrylak P and Korkusinski M 2005 Voltage-controlled coded qubit based on electron spin *Solid State Commun.* **136** 508–12

[203] Ren Y, Wang L, Liu Z and Wu M 2014 Energy spectra of three electrons in SiGe/Si/SiGe laterally coupled triple quantum dots *Physica E: Low-Dimens. Syst. Nanostruct.* **63** 329–36

[204] Kawano Y and Ozawa M 2006 Quantum gates generated by rotationally invariant operators in a decoherence-free subsystem *Phys. Rev.* A **73** 012339

[205] Lee B, Witzel W M and Das Sarma S 2008 Universal pulse sequence to minimize spin dephasing in the central spin decoherence problem *Phys. Rev. Lett.* **100** 160505

[206] Hickman G T, Wang X, Kestner J P and Das Sarma S 2013 Dynamically corrected gates for an exchange-only qubit *Phys. Rev.* B **88** 161303

[207] Takakura T, Noiri A, Obata T, Otsuka T, Yoneda J, Yoshida K and Tarucha S 2014 Single to quadruple quantum dots with tunable tunnel couplings *Appl. Phys. Lett.* **104** 113109

[208] Rashba E I 2008 Theory of electric dipole spin resonance in quantum dots: mean field theory with gaussian fluctuations and beyond *Phys. Rev.* B **78** 195302

[209] Gordon J P and Bowers K D 1958 Microwave spin echoes from donor electrons in silicon *Phys. Rev. Lett.* **1** 368–70

[210] Chiba M and Hirai A 1972 Electron spin echo decay behaviours of phosphorus doped silicon *J. Phys. Soc. Japan* **33** 730–8

[211] Tezuka H, Stegner A R, Tyryshkin A M, Shankar S, Thewalt M L W, Lyon S A, Itoh K M and Brandt M S 2010 Electron paramagnetic resonance of boron acceptors in isotopically purified silicon *Phys. Rev.* B **81** 161203

[212] Alexander S and Anderson P W 1964 Interaction between localized states in metals *Phys. Rev.* **133** A1594–603

[213] Stöhr J and Siegmann H C 2006 From fundamentals to nanoscale dynamics *Magnetism* (Springer Series in Solid-State Sciences) (Berlin: Springer) (https://doi.org/10.1007/978-3-540-30283-4)

[214] Kostyrko T and Bułka B R 2011 Canonical perturbation theory for inhomogeneous systems of interacting fermions *Phys. Rev.* B **84** 035123

[215] Trif M, Troiani F, Stepanenko D and Loss D 2008 Spin-electric coupling in molecular magnets *Phys. Rev. Lett.* **101** 217201

[216] Kyriakidis J and Penney S J 2005 Coherent rotations of a single spin-based qubit in a single quantum dot at fixed zeeman energy *Phys. Rev.* B **71** 125332

[217] Royer B, Grimsmo A L, Didier N and Blais A 2016 Fast and high-fidelity entangling gate through parametrically modulated longitudinal coupling **1** 11

[218] Beaudoin F, Lachance-Quirion D, Coish W A and Pioro-Ladrière M 2016 Coupling a single electron spin to a microwave resonator: controlling transverse and longitudinal couplings *Nanotechnology* **27** 464003

[219] Borselli M G *et al* 2011 Measurement of valley splitting in high-symmetry Si/SiGe quantum dots *Appl. Phys. Lett.* **98** 123118

[220] Liu Z, Wang L and Shen K 2012 Energy spectra of three electrons in Si/SiGe single and vertically coupled double quantum dots *Phys. Rev.* B **85** 045311

[221] Tahan C and Joynt R 2014 Relaxation of excited spin, orbital and valley qubit states in ideal silicon quantum dots *Phys. Rev.* B **89** 075302

[222] Ferraro E, De Michielis M, Mazzeo G, Fanciulli M and Prati E 2014 Effective Hamiltonian for the hybrid double quantum dot qubit *Quantum Inf. Process.* **13** 1155–73

[223] Shi Z, Simmons C B, Prance J R, King Gamble J, Friesen M, Savage D E, Lagally M G, Coppersmith S N and Eriksson M A 2011 Tunable singlet-triplet splitting in a few-electron Si/SiGe quantum dot *Appl. Phys. Lett.* **99** 233108

[224] Boykin T B, Klimeck G, Friesen M, Coppersmith S N, von Allmen P, Oyafuso F and Lee S 2004 Valley splitting in low-density quantum-confined heterostructures studied using tight-binding models *Phys. Rev.* B **70** 165325

[225] Saraiva A L, Calderón M J, Hu X, Das Sarma S and Koiller B 2009 Physical mechanisms of interface-mediated intervalley coupling in Si *Phys. Rev.* B **80** 081305

[226] Hanson R, van Beveren L H W, Vink I T, Elzerman J M, Naber W J M, Koppens F H L, Kouwenhoven L P and Vandersypen L M K 2005 Single-shot readout of electron spin states in a quantum dot using spin-dependent tunnel rates *Phys. Rev. Lett.* **94** 196802

[227] Simmons C B *et al* 2011 Tunable spin loading and T_1 of a silicon spin qubit measured by single-shot readout *Phys. Rev. Lett.* **106** 156804

[228] Lei Y, Wen Y and Fang-Wei W 2014 Hybrid double-dot qubit measurement with a quantum point contact *Chin. Phys.* B **23** 100303

[229] DiVincenzo D P 1995 Two-bit gates are universal for quantum computation *Phys. Rev.* A **51** 1015

[230] Lloyd S 1995 Almost any quantum logic gate is universal *Phys. Rev. Lett.* **75** 346–9

[231] Zeuch D and Bonesteel N E 2016 Simple derivation of the fong-wandzura pulse sequence *Phys. Rev.* A **93** 010303

[232] Kouwenhoven L, Austing D G and Tarucha S 2001 Few-electron quantum dots *Rep. Prog. Phys.* **64** 701

[233] Ferraro E, De Michielis M, Fanciulli M and Prati E 2015 Coherent tunneling by adiabatic passage of an exchange-only spin qubit in a double quantum dot chain *Phys. Rev.* B **91** 075435

[234] Wardrop M P and Doherty A C 2016 Characterization of an exchange-based two-qubit gate for resonant exchange qubits *Phys. Rev.* B **93** 075436

[235] Zhang J, Vala J, Sastry S and Whaley K B 2003 Geometric theory of nonlocal two-qubit operations *Phys. Rev.* A **67** 042313

[236] Fowler A G, Mariantoni M, Martinis J M and Cleland A N 2012 Surface codes: towards practical large-scale quantum computation *Phys. Rev.* A **86** 032324

[237] Lidar D and Brun T 2013 *Quantum Error Correction* (Cambridge: Cambridge University Press) (https:doi.org/10.1017/CBO9781139034807)

[238] Brecht T, Pfaff W, Wang C, Chu Y, Frunzio L, Devoret M H and Schoelkopf R J 2016 Multilayer microwave integrated quantum circuits for scalable quantum computing *npj Quantum Inf.* **2** 16002

[239] Leijnse M and Flensberg K 2013 Coupling spin qubits via superconductors *Phys. Rev. Lett.* **111** 060501

[240] Hassler F, Catelani G and Bluhm H 2015 Exchange interaction of two spin qubits mediated by a superconductor *Phys. Rev.* B **92** 235401

[241] Stotz J A H, Hey R, Santos P V and Ploog K H 2005 Coherent spin transport through dynamic quantum dots *Nat. Mater.* **4** 585–8

[242] Hermelin S, Takada S, Yamamoto M, Tarucha S, Wieck A D, Saminadayar L, Bauerle C and Meunier T 2011 Electrons surfing on a sound wave as a platform for quantum optics with flying electrons *Nature* **477** 435–8

[243] McNeil R P G, Kataoka M, Ford C J B, Barnes C H W, Anderson D, Jones G A C, Farrer I and Ritchie D A 2011 On-demand single-electron transfer between distant quantum dots *Nature* **477** 439–42

[244] Schuetz M J A, Kessler E M, Giedke G, Vandersypen L M K, Lukin M D and Cirac J I 2015 Universal quantum transducers based on surface acoustic waves *Phys. Rev.* X **5** 031031

[245] Benito M, Schuetz M J A, Cirac J I, Platero G and Giedke G 2016 Dissipative long-range entanglement generation between electronic spins *Phys. Rev.* B **94** 115404

[246] Bertrand B, Hermelin S, Takada S, Yamamoto M, Tarucha S, Ludwig A, Wieck A D, Bäuerle C and Meunier T 2016 Fast spin information transfer between distant quantum dots using individual electrons *Nat. Nanotechnol.* **11** 672–6

[247] Trifunovic L, Pedrocchi F L and Loss D 2013 Long-distance entanglement of spin qubits via ferromagnet *Phys. Rev.* X **3** 041023

[248] Braakman F R, Barthelemy P, Reichl C, Wegscheider W and Vandersypen L M K 2013 Long-distance coherent coupling in a quantum dot array *Nat. Nanotechnol.* **8** 432–7

[249] Sánchez R, Gallego-Marcos F and Platero G 2014 Superexchange blockade in triple quantum dots *Phys. Rev.* B **89** 161402

[250] Srinivasa V, Xu H and Taylor J M 2015 Tunable spin-qubit coupling mediated by a multielectron quantum dot *Phys. Rev. Lett.* **114** 226803

[251] Kuo D M T and Chang Y-C 2014 Long-distance coherent tunneling effect on the charge and heat currents in serially coupled triple quantum dots *Phys. Rev.* B **89** 115416

[252] Menchon-Enrich R, Benseny A, Ahufinger V, Greentree A D, Busch T and Mompart J 2016 Spatial adiabatic passage: a review of recent progress *Rep. Prog. Phys.* **79** 074401

[253] Braakman F R, Danon J, Schreiber L R, Wegscheider W and Vandersypen L M K 2014 Dynamics of spin-flip photon-assisted tunneling *Phys. Rev.* B **89** 075417

[254] Gallego-Marcos F, Snchez R and Platero G 2015 Photon assisted long-range tunneling *J. Appl. Phys.* **117** 112808

[255] Stano P, Klinovaja J, Braakman F R, Vandersypen L M K and Loss D 2015 Fast long-distance control of spin qubits by photon-assisted cotunneling *Phys. Rev.* B **92** 075302

[256] Yang G, Hsu C-H, Stano P, Klinovaja J and Loss D 2016 Long-distance entanglement of spin qubits via quantum hall edge states *Phys. Rev.* B **93** 075301

[257] Pal A, Rashba E I and Halperin B I 2014 Driven nonlinear dynamics of two coupled exchange-only qubits *Phys. Rev.* X **4** 011012

[258] Pal A, Rashba E I and Halperin B I 2015 Exact CNOT gates with a single nonlocal rotation for quantum-dot qubits *Phys. Rev.* B **92** 125409

[259] Mehl S 2015 Two-qubit pulse gate for the three-electron double quantum dot qubit *Phys. Rev.* B **91** 035430

[260] Serina M, Trifunovic L, Kloeffel C and Loss D 2016 Long-range interaction between charge and spin qubits in quantum dots (arXiv:1601.03564)

[261] Puri S and Blais A 2016 High-fidelity resonator-induced phase gate with single-mode squeezing *Phys. Rev. Lett.* **116** 180501

[262] Schuetz M J A, Giedke G, Vandersypen L M K and Cirac J I 2017 High-fidelity hot gates for generic spin-resonator systems *Phys. Rev.* A **95** 052335

[263] Viennot J J, Delbecq M R, Bruhat L E, Dartiailh M C, Desjardins M M, Baillergeau M, Cottet A and Kontos T 2016 Towards hybrid circuit quantum electrodynamics with quantum dots *C. R. Phys.* **17** 705–17 (quantum microwaves / Micro-ondes quantiques)

[264] Blais A, Huang R-S, Wallraff A, Girvin S M and Schoelkopf R J 2004 Cavity quantum electrodynamics for superconducting electrical circuits: an architecture for quantum computation *Phys. Rev.* A **69** 062320

[265] Schoelkopf R J and Girvin S M 2008 Wiring up quantum systems *Nature* **451** 664–9

[266] Houck A A, Tureci H E and Koch J 2012 On-chip quantum simulation with superconducting circuits *Nat. Phys.* **8** 292–9

[267] Cohen-Tannoudji C, Dupont-Roc J and Grynberg G 2007 *Photons and Atoms: Introduction to Quantum Electrodynamics* (New York: Wiley) (https:doi.org/10.1002/9783527618422.ch)

[268] Sørensen A and Mølmer K 2000 Entanglement and quantum computation with ions in thermal motion *Phys. Rev.* A **62** 022311

[269] Marzari N, Mostofi A A, Yates J R, Souza I and Vanderbilt D 2012 Maximally localized Wannier functions: theory and applications *Rev. Mod. Phys.* **84** 1419

[270] Billangeon P-M, Tsai J S and Nakamura Y 2015 Circuit-QED-based scalable architectures for quantum information processing with superconducting qubits *Phys. Rev.* B **91** 094517

[271] Richer S and DiVincenzo D 2016 Circuit design implementing longitudinal coupling: a scalable scheme for superconducting qubits *Phys. Rev.* B **93** 134501

[272] Jaynes E and Cummings F 1963 Comparison of quantum and semiclassical radiation theories with application to the beam maser *Proc. IEEE* **51** 89

[273] Cummings F W 1965 Stimulated emission of radiation in a single mode *Phys. Rev.* **140** A1051–6

[274] Shore B W and Knight P L 1993 The Jaynes–Cummings model *J. Mod. Opt.* **40** 1195–238

[275] Wu Y and Yang X 2007 Strong-coupling theory of periodically driven two-level systems *Phys. Rev. Lett.* **98** 013601

[276] Blais A, Gambetta J, Wallraff A, Schuster D I, Girvin S M, Devoret M H and Schoelkopf R J 2007 Quantum-information processing with circuit quantum electrodynamics *Phys. Rev.* A **75** 032329

[277] Schuch N and Siewert J 2003 Natural two-qubit gate for quantum computation using the XY interaction *Phys. Rev.* A **67** 032301

[278] Tanamoto T, Maruyama K, Liu Y-X, Hu X and Nori F 2008 Efficient purification protocols using iSWAP gates in solid-state qubits *Phys. Rev.* A **78** 062313

[279] Childs A M and Chuang I L 2000 Universal quantum computation with two-level trapped ions *Phys. Rev.* A **63** 012306

[280] Wallraff A, Schuster D I, Blais A, Gambetta J M, Schreier J, Frunzio L, Devoret M H, Girvin S M and Schoelkopf R J 2007 Sideband transitions and two-tone spectroscopy of a superconducting qubit strongly coupled to an on-chip cavity *Phys. Rev. Lett.* **99** 050501

[281] Leek P J, Filipp S, Maurer P, Baur M, Bianchetti R, Fink J M, Göppl M, Steffen L and Wallraff A 2009 Using sideband transitions for two-qubit operations in superconducting circuits *Phys. Rev.* B **79** 180511

[282] Sapmaz S, Jarillo-Herrero P, Kouwenhoven L P and van der Zant H S J 2006 Quantum dots in carbon nanotubes *Semicond. Sci. Technol.* **21** S52

[283] Zanardi P and Rasetti M 1997 Error avoiding quantum codes *Mod. Phys. Lett.* B **11** 1085–93

[284] Lidar D A, Chuang I L and Whaley K B 1998 Decoherence-free subspaces for quantum computation *Phys. Rev. Lett.* **81** 2594–7

[285] Viola L, Knill E and Lloyd S 2000 Dynamical generation of noiseless quantum subsystems *Phys. Rev. Lett.* **85** 3520–3

[286] Overhauser A W 1953 Polarization of nuclei in metals *Phys. Rev.* **92** 411–5

[287] Abragam A 1961 *The Principles of Nuclear Magnetism* (*Int. Series of Monographs on Physics*) (Oxford: Clarendon)

[288] Slichter C P 1990 *Principles of Magnetic Resonance* (*Springer Series in Solid-State Sciences*) (Berlin: Springer) (https://doi.org/10.1007/978-3-662-09441-9)

[289] Hung J-T, Cywiński L, Hu X and Das Sarma S 2013 Hyperfine interaction induced dephasing of coupled spin qubits in semiconductor double quantum dots *Phys. Rev.* B **88** 085314

[290] Delbecq M R *et al* 2016 Quantum dephasing in a gated GaAs triple quantum dot due to nonergodic noise *Phys. Rev. Lett.* **116** 046802

[291] Falci G, D'Arrigo A, Mastellone A and Paladino E 2004 Dynamical suppression of telegraph and 1/*f* noise due to quantum bistable fluctuators *Phys. Rev.* A **70** 040101

[292] Faoro L and Viola L 2004 Dynamical suppression of 1/*f* noise processes in qubit systems *Phys. Rev. Lett.* **92** 117905

[293] Rebentrost P, Serban I, Schulte-Herbrüggen T and Wilhelm F K 2009 Optimal control of a qubit coupled to a non-Markovian environment *Phys. Rev. Lett.* **102** 090401

[294] Du J, Rong X, Zhao N, Wang Y, Yang J and Liu R B 2009 Preserving electron spin coherence in solids by optimal dynamical decoupling *Nature* **461** 1265–8

[295] Green T J, Sastrawan J, Uys H and Biercuk M J 2013 Arbitrary quantum control of qubits in the presence of universal noise *New J. Phys.* **15** 095004

[296] Szańkowski P, Trippenbach M and Cywiński L 2016 Spectroscopy of cross correlations of environmental noises with two qubits *Phys. Rev.* A **94** 012109

[297] Carr H Y and Purcell E M 1954 Effects of diffusion on free precession in nuclear magnetic resonance experiments *Phys. Rev.* **94** 630–8

[298] Meiboom S and Gill D 1958 Modified spin echo method for measuring nuclear relaxation times *Rev. Sci. Instrum.* **29** 688–91

[299] Uhrig G S 2007 Keeping a quantum bit alive by optimized π-pulse sequences *Phys. Rev. Lett.* **98** 100504

[300] Uhrig G S 2008 Exact results on dynamical decoupling by pulses in quantum information processes *New J. Phys.* **10** 083024

[301] Uhrig G S 2009 Concatenated control sequences based on optimized dynamic decoupling *Phys. Rev. Lett.* **102** 120502

[302] Uys H, Biercuk M J and Bollinger J J 2009 Optimized noise filtration through dynamical decoupling *Phys. Rev. Lett.* **103** 040501

[303] Johnson J B 1928 Thermal agitation of electricity in conductors *Phys. Rev.* **32** 97

[304] Nyquist H 1928 Thermal agitation of electric charge in conductors *Phys. Rev.* **32** 110

[305] Langsjoen L S, Poudel A, Vavilov M G and Joynt R 2012 Qubit relaxation from evanescent-wave Johnson noise *Phys. Rev.* A **86** 010301

[306] Poudel A, Langsjoen L S, Vavilov M G and Joynt R 2013 Relaxation in quantum dots due to evanescent-wave Johnson noise *Phys. Rev.* B **87** 045301

[307] Schottky W 1918 Über spontane stromschwankungen in verschiedenen elektrizitätsleitern *Ann. Phys.* **362** 541–67

[308] Ramon G 2015 Non-gaussian signatures and collective effects in charge noise affecting a dynamically decoupled qubit *Phys. Rev.* B **92** 155422

[309] Cywiński L 2014 Dynamical-decoupling noise spectroscopy at an optimal working point of a qubit *Phys. Rev.* A **90** 042307

[310] Friesen M, Eriksson M A and Coppersmith S N 2016 A decoherence-free subspace for charge: the quadrupole qubit (arXiv:1605.01797)

[311] Li Y P, Tsui D C, Heremans J J, Simmons J A and Weimann G W 1990 Low frequency noise in transport through quantum point contacts *Appl. Phys. Lett.* **57** 774–6

[312] Dekker C, Scholten A J, Liefrink F, Eppenga R, van Houten H and Foxon C T 1991 Spontaneous resistance switching and low-frequency noise in quantum point contacts *Phys. Rev. Lett.* **66** 2148–51

[313] Sakamoto T, Nakamura Y and Nakamura K 1995 Distributions of single carrier traps in GaAs/Al_xGa_{1-x}As heterostructures *Appl. Phys. Lett.* **67** 2220–2

[314] Kurdak C, Chen C-J, Tsui D C, Parihar S, Lyon S and Weimann G W 1997 Resistance fluctuations in GaAs/Al_xGa_{1-x}As quantum point contact and hall bar structures *Phys. Rev.* B **56** 9813–8

[315] Hayashi T, Fujisawa T, Cheong H D, Jeong Y H and Hirayama Y 2003 Coherent manipulation of electronic states in a double quantum dot *Phys. Rev. Lett.* **91** 226804

[316] Buizert C, Koppens F H L, Pioro-Ladrière M, Tranitz H-P, Vink I T, Tarucha S, Wegscheider W and Vandersypen L M K 2008 *In situ* reduction of charge noise in GaAs/Al_xGa_{1-x}As Schottky-gated devices *Phys. Rev. Lett.* **101** 226603

[317] Petersson K, Petta J, Lu H and Gossard A 2010 Quantum coherence in a one-electron semiconductor charge qubit *Phys. Rev. Lett.* **105** 246804

[318] Takeda K, Obata T, Fukuoka Y, Akhtar W M, Kamioka J, Kodera T, Oda S and Tarucha S 2013 Characterization and suppression of low-frequency noise in Si/SiGe quantum point contacts and quantum dots *Appl. Phys. Lett.* **102** 123113

[319] Freeman B M, Schoenfield J S and Jiang H 2013 Comparison of low frequency charge noise in identically patterned Si/SiO2 and Si/SiGe quantum dots *Appl. Phys. Lett.* **108** 253108

[320] Dial O E, Shulman M D, Harvey S P, Bluhm H, Umansky V and Yacoby A 2013 Charge noise spectroscopy using coherent exchange oscillations in a singlet-triplet qubit *Phys. Rev. Lett.* **110** 146804

[321] Taylor J and Lukin M 2006 Dephasing of quantum bits by a quasi-static mesoscopic environment *Quantum Inf. Process.* **5** 503

[322] Hu X 2011 Two-spin dephasing by electron-phonon interaction in semiconductor double quantum dots *Phys. Rev.* B **83** 165322
[323] Gamble J K, Friesen M, Coppersmith S N and Hu X 2012 Two-electron dephasing in single Si and GaAs quantum dots *Phys. Rev.* B **86** 035302
[324] Huang P and Hu X 2014 Electron spin relaxation due to charge noise *Phys. Rev.* B **89** 195302
[325] Yu P 2010 *Fundamentals of Semiconductors: Physics and Materials Properties* (Berlin: Springer)
[326] Maune B M *et al* 2012 Coherent singlet-triplet oscillations in a silicon-based double quantum dot *Nature* **481** 344
[327] Culcer D, Cywiński L, Li Q, Hu X and Das Sarma S 2009 Realizing singlet-triplet qubits in multivalley Si quantum dots *Phys. Rev.* B **80** 205302
[328] Culcer D, Cywiński L, Li Q, Hu X and Das Sarma S 2010 Quantum dot spin qubits in silicon: multivalley physics *Phys. Rev.* B **82** 155312
[329] Rohling N and Burkard G 2012 Universal quantum computing with spin and valley states *New J. Phys.* **14** 083008
[330] Rohling N, Russ M and Burkard G 2014 Hybrid spin and valley quantum computing with singlet-triplet qubits *Phys. Rev. Lett.* **113** 176801
[331] Veldhorst M, Ruskov R, Yang C H, Hwang J C C, Hudson F E, Flatté M E, Tahan C, Itoh K M, Morello A and Dzurak A S 2015 Spin–orbit coupling and operation of multivalley spin qubits *Phys. Rev.* B **92** 201401
[332] Rančić M J and Burkard G 2016 Electric dipole spin resonance in systems with a valley-dependent *g* factor *Phys. Rev.* B **93** 205433
[333] Boross P, Széchenyi G, Culcer D and Pályi A 2016 Control of valley dynamics in silicon quantum dots in the presence of an interface step *Phys. Rev.* B **94** 035438
[334] Zimmerman N, Huang P and Culcer D 2016 Valley phase, interface roughness and voltage control and coherent manipulation in Si quantum dots (arXiv:1608.06881)
[335] King Gamble J *et al* 2016 Valley splitting of single-electron Si MOs quantum dots *Appl. Phys. Lett.* **109** 253101
[336] Saraiva A L, Calder M J, Capaz R B, Hu X, Das Sarma S and Koiller B 2011 Intervalley coupling for interface-bound electrons in silicon: an effective mass study *Phys. Rev.* B **84** 155320
[337] Lim W H, Yang C H, Zwanenburg F A and Dzurak A S 2011 Spin filling of valley–orbit states in a silicon quantum dot *Nanotechnology* **22** 335704
[338] Wu Y and Culcer D 2012 Coherent electrical rotations of valley states in Si quantum dots using the phase of the valley-orbit coupling *Phys. Rev.* B **86** 035321
[339] Culcer D, Saraiva A L, Koiller B, Hu X and Das Sarma S 2012 Valley-based noise-resistant quantum computation using Si quantum dots *Phys. Rev. Lett.* **108** 126804
[340] Hao X, Ruskov R, Xiao M, Tahan C and Jiang H 2014 Electron spin resonance and spin–valley physics in a silicon double quantum dot *Nat. Commun.* **5** 3860